WILEY    *Journal of*
METAMORPHIC GEOLOGY

ORIGINAL ARTICLE

# Subduction metamorphism of serpentinite-hosted carbonates beyond antigorite-serpentinite dehydration (Nevado-Filábride Complex, Spain)

Manuel D. Menzel[1] (ID) | Carlos J. Garrido[1] | Vicente López Sánchez-Vizcaíno[2] | Károly Hidas[1,3] | Claudio Marchesi[1,4]

[1]Instituto Andaluz de Ciencias de la Tierra (IACT), CSIC – Universidad de Granada, Armilla, Spain

[2]Dpto. de Geología (Unidad Asociada al IACT-CSIC), Universidad de Jaén, Escuela Politécnica Superior, Linares, Spain

[3]Dpto. de Geodinámica, Facultad de Ciencias, Universidad de Granada, Granada, Spain

[4]Dpto. de Mineralogía y Petrología, Facultad de Ciencias, Universidad de Granada, Granada, Spain

**Correspondence**
Manuel D. Menzel, Instituto Andaluz de Ciencias de la Tierra (IACT), CSIC – Universidad de Granada, Armilla, Spain.
Email: manuel.menzel@csic.es; manuelmenzel@gmail.com

## Abstract

At sub-arc depths, the release of carbon from subducting slab lithologies is mostly controlled by fluid released by devolatilization reactions such as dehydration of antigorite (Atg-) serpentinite to prograde peridotite. Here we investigate carbonate–silicate rocks hosted in Atg-serpentinite and prograde chlorite (Chl-) harzburgite in the Milagrosa and Almirez ultramafic massifs of the palaeo-subducted Nevado-Filábride Complex (NFC, Betic Cordillera, S. Spain). These massifs provide a unique opportunity to study the stability of carbonate during subduction metamorphism at $P–T$ conditions before and after the dehydration of Atg-serpentinite in a warm subduction setting. In the Milagrosa massif, carbonate–silicate rocks occur as lenses of Ti-clino-humite–diopside–calcite marbles, diopside–dolomite marbles and antigorite–diopside–dolomite rocks hosted in clinopyroxene-bearing Atg-serpentinite. In Almirez, carbonate–silicate rocks are hosted in Chl-harzburgite and show a high-grade assemblage composed of olivine, Ti-clinohumite, diopside, chlorite, dolomite, calcite, Cr-bearing magnetite, pentlandite and rare aragonite inclusions. These NFC carbonate–silicate rocks have variable CaO and $CO_2$ contents at nearly constant Mg/Si ratio and high Ni and Cr contents, indicating that their protoliths were variable mixtures of serpentine and Ca-carbonate (i.e., ophicarbonates). Thermodynamic modelling shows that the carbonate–silicate rocks attained peak metamorphic conditions similar to those of their host serpentinite (Milagrosa massif; 550–600°C and 1.0–1.4 GPa) and Chl-harzburgite (Almirez massif; 1.7–1.9 GPa and 680°C). Microstructures, mineral chemistry and phase relations indicate that the hybrid carbonate–silicate bulk rock compositions formed before prograde metamorphism, likely during seawater hydrothermal alteration, and subsequently underwent subduction metamorphism. In the CaO–MgO–$SiO_2$ ternary, these processes resulted in a compositional variability of NFC serpentinite-hosted carbonate–silicate rocks along the serpentine-calcite mixing trend, similar to that observed in serpentinite-hosted carbonate-rocks in other palaeo-subducted metamorphic terranes. Thermodynamic

modelling using classical models of binary $H_2O$–$CO_2$ fluids shows that the compositional variability along this binary determines the temperature of the main devolatilization reactions, the fluid composition and the mineral assemblages of reaction products during prograde subduction metamorphism. Thermodynamic modelling considering electrolytic fluids reveals that $H_2O$ and molecular $CO_2$ are the main fluid species and charged carbon-bearing species occur only in minor amounts in equilibrium with carbonate–silicate rocks in warm subduction settings. Consequently, accounting for electrolytic fluids at these conditions slightly increases the solubility of carbon in the fluids compared with predictions by classical binary $H_2O$–$CO_2$ fluids, but does not affect the topology of phase relations in serpentinite-hosted carbonate-rocks. Phase relations, mineral composition and assemblages of Milagrosa and Almirez (meta)-serpentinite-hosted carbonate–silicate rocks are consistent with local equilibrium between an infiltrating fluid and the bulk rock composition and indicate a limited role of infiltration-driven decarbonation. Our study shows natural evidence for the preservation of carbonates in serpentinite-hosted carbonate–silicate rocks beyond the Atg-serpentinite breakdown at sub-arc depths, demonstrating that carbon can be recycled into the deep mantle.

## 1 | INTRODUCTION

Subduction zones transfer carbon from the Earth′s surface to its deep interior and control the long-term deep carbon cycle. Sediments, altered oceanic crust and the hydrated lithospheric mantle in the subducting slab contain carbon in the form of carbonate minerals and organic carbon. During subduction of the slab, metamorphic devolatilization reactions of hydrous minerals release fluids that enhance decarbonation reactions (Connolly, 2005; Gorman, Kerrick, & Connolly, 2006 ) and induce partial melting of the overlying mantle wedge (Dasgupta, Hirschmann, & Withers, 2004; Poli, 2015; Tumiati, Fumagalli, Tiraboschi, & Poli, 2013). Metamorphic devolatilization reactions thus play a vital role in the deep carbon cycle by ultimately modulating the amount of the subducted carbon returned to the Earth's surface via arc volcanism (Dasgupta, 2013 ; Kerrick & Connolly, 2001). Different estimates of the carbon fluxes at sub-arc depths mainly arise from uncertainties about the efficiency of rock-buffered devolatilization reactions, the role of congruent carbonate dissolution in fluid-dominated conditions and the pathways of fluids (Connolly & Galvez, 2018; Galvez, Connolly, & Manning, 2016; Kelemen & Manning, 2015).

Because it releases high amounts of $H_2O$-rich fluids—9 wt% $H_2O$ at ~660°C—dehydration of Atg-serpentinite is potentially the most relevant devolatilization reaction to mobilize carbon at sub-arc depths into fluids from slab and mantle wedge lithologies (Bromiley & Pawley, 2003; Padrón-Navarta,

Hermann, Garrido, López Sánchez-Vizcaíno, & Gómez-Pugnaire, 2010; Rüpke, Morgan, Hort, & Connolly, 2004; Ulmer & Trommsdorff, 1995). There is mounting evidence that fluids generated during high-pressure (HP) deserpentinization are oxidizing—close to the hematite-magnetite oxygen buffer—and are mildly alkaline (Alt et al., 2012; Debret et al., 2015; Debret & Sverjensky, 2017; Evans, Reddy, Tomkins, Crossley, & Frost, 2017; Galvez et al., 2016). If so, deserpentinization fluids could mobilize both reduced and inorganic carbon as $CO_{2(aq)}$ and $HCO_3^-$ (Facq, Daniel, Montagnac, Cardon, & Sverjensky, 2014). Antigorite dehydration fluids are rich in non-volatile components (Scambelluri, Müntener, Ottolini, Pettke, & Vannucci, 2004), which may form aqueous complexes such as $NaHCO_3$ and $CaHCO_3^+$ and increase carbon solubility (Facq, Daniel, Montagnac, Cardon, & Sverjensky, 2016; Galvez et al., 2016). Therefore, deserpentinization fluids might constitute very effective agents for the recycling of carbon back to arc volcanism in the subduction factory.

Exhumed metamorphic terranes provide essential insights into the mechanisms of deep carbon recycling and mobilization in subduction zones (Bebout & Penniston-Dorland, 2016; Ferrando, Groppo, Frezzotti, Castelli, & Proyer, 2017; Piccoli et al., 2016; Scambelluri et al., 2016). Thermodynamic calculations and studies of eclogite facies marbles and carbonated eclogites and serpentinites in palaeo-subducted metamorphic terranes show that carbonate minerals undergo variable extents of decarbonation and can be stable at high pressure (Collins et al., 2015; Connolly, 2005;

Cook-Kollars, Bebout, Collins, Angiboust, & Agard, 2014; Ferrando et al., 2017; Proyer, Mposkos, Baziotis, & Hoinkes, 2008). Studies of natural examples of HP metamorphism of carbonate-bearing rocks during Atg-serpentinite dehydration are scarce and limited to assess the mass-balance of carbon during dehydration (Alt et al., 2012). Most of the available estimates of carbon release in deserpentinization fluids heavily rely on numerical and thermodynamic modelling (Gorman et al.,2006 ; Kelemen & Manning, 2015). The study of serpentinite-hosted carbonates (e.g., ophicarbonates) can provide a direct record of the impact of antigorite dehydration fluids on carbon release mechanisms in subduction zones.

Exhumed palaeo-subducted metamorphic terranes offer a unique opportunity to investigate the metamorphism of



**FIGURE 1** Compilation of peak pressure–temperature (P–T) conditions of meta-ophicarbonates (white fields) superposed on the pseudosection of a Ca-bearing serpentinite from the Almirez massif. VM: Voltri massif (Scambelluri et al., 2016); ZS: Zermatt-Saas; B: Bracco Unit, Internal Ligurides; UV: Ubaye Valley, Western Alps (all from Collins et al., 2015). L, L*: Lanzo massif peak conditions and PT of graphite-formation in ophicarbonate, respectively (Vitale Brovarone et al., 2017); BA: contact-metamorphic ophicarbonates, Bergell aureole (Pozzorini & Früh-Green, 1996; Trommsdorff & Connolly, 1996); BD: Bellinzona-Dascio unit, Central Alps (Stucki, 2001). Dark grey field: maximum P–T conditions for hydrothermal ophicarbonate formation in seafloor serpentinites (Schwarzenbach et al., 2013). The P–T path of the Almirez massif (after Laborda-López et al., 2018) hosting meta-ophicarbonates beyond the antigorite stability (this study) is shown by the black dashed arrow. P–T paths at the Moho depth of the slab for hot, intermediate and cold subduction zones (HSZ, ISZ and CSZ, respectively) after van Keken, Hacker, Syracuse, and Abers (2011). Numbered fields: (1) Chl, Tlc, Tr, Ol, $H_2O$; (2) Chl, Ath, Tr, Ol, $H_2O$. P–T conditions of lizardite-antigorite transition after Evans (2004). PhA: phase A; see Table 1 for other abbreviations of mineral names.

serpentinite-hosted ophicarbonate. Examples of meta-ophicarbonate associated to prograde metamorphism of serpentinite are numerous in the geological record (Figure 1). Many examples are preserved in brucite- or olivine-bearing Atg-serpentinites that underwent metamorphism in intermediate to warm subduction settings (cf. orange and pink dotted paths in Figure 1; Collins et al., 2015; Scambelluri et al., 2016; Vitale Brovarone et al., 2017). Examples of serpentinite-hosted meta-ophicarbonate recording metamorphic grade approaching or exceeding the P–T conditions of antigorite breakdown are very rare (e.g. in the Bellinzona–Dascio unit and at the Bergell aureole, Central Alps; fields labelled BD and BA in Figure 1) and mostly associated to shallow contact metamorphism (Stucki, 2001; Trommsdorff & Connolly, 1996).

In this contribution, we present a petrological study of two occurrences of carbonate lenses hosted in HP Atg-serpentinite (Milagrosa ultramafic massif) and prograde Chl-harzburgite (Almirez ultramafic massif), recording respectively, subduction metamorphism prior to and after the conditions of antigorite breakdown in a hot subduction setting. In the Almirez massif, the dehydration reaction of serpentinite to Chl-harzburgite is preserved in the field, which makes it a unique case study to investigate the mobility of carbon during the breakdown of antigorite in subduction zones (Alt et al., 2012; Garrido et al., 2005 ; Padrón-Navarta, López Sánchez-Vizcaíno, Garrido, & Gomez-Pugnaire, 2011). Comparison of these two natural examples of prograde metamorphism of serpentinite-hosted ophicarbonate sheds new light on the processes that control carbon fluxes in subduction zones.
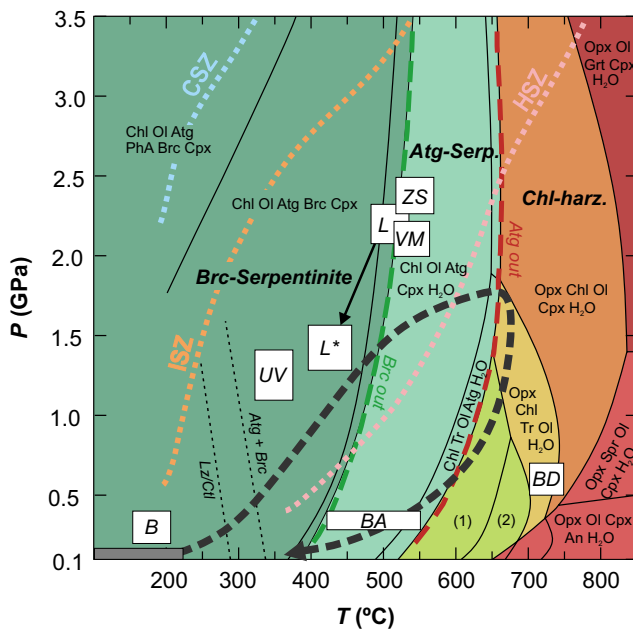
## 2 | THE NEVADO-FILÁBRIDE COMPLEX

The Nevado-Filábride Complex (NFC) is part of the internal zones of the Betic Cordilleras (S. Spain; Figure 2a,b) and records Alpine subduction-related HP metamorphism during early to middle Miocene (18–14 Ma; Gómez-Pugnaire et al., 2012; Kirchner, Behr, Loewy, & Stockli, 2016; López Sánchez-Vizcaíno, Rubatto, Gómez-Pugnaire, Trommsdorff, & Müntener, 2001; Platt, Anczkiewicz, Soto, Kelley, & Thirlwall, 2006). Estimates of the peak pressure–temperature (P–T) conditions for different units of this complex range from ~1.0 to 2.2 GPa and 550–700°C (Booth-Rea, Martínez-Martínez, & Giaconia, 2015; Gómez-Pugnaire, Franz, & López Sánchez-Vizcaíno, 1994; Jabaloy-Sánchez, Gómez-Pugnaire, Padrón-Navarta, López Sánchez-Vizcaíno, & Garrido, 2015; Li & Massonne, 2018; López Sánchez-Vizcaíno, Connolly, & Gomez-Pugnaire, 1997; Platt, Behr, Johanesen, & Williams, 2013). The NFC constituted a Jurassic extended continental margin (Gómez-Pugnaire et al., 2012) or narrow oceanic basin (Puga et al., 2011) that separated Iberia from the allochthonous Alborán domain units, which were part of the AlKaPeCa terranes in the central

**TABLE 1** Overview of the lithologies discussed in this study and their mineral assemblages

| Lithology | Mineral assemblage | Retrograde phases | Key features/trace phases |
|---|---|---|---|
| *Milagrosa* | | | |
| TiCl-Cal marble[a] | Cal+Chl+Di+TiCl+Dol±TiChn | ±Qtz | Carbonate dominated; banded /±Ap, Po, Py, Mag, Ilm, Prv |
| Di–Dol marble[a] | Dol+Di+Chl+Cal±Tr±TiCl±TiChn±Mag | Tr+Cal (?); Tlc, Qtz | Carbonate/silicate modal ratio 1:1; greenish in hand sample /±Atg, Ilm, Ap |
| Atg–Di–Dol rock[a] | Atg+Dol+Di+Chl±Cal±TiCl±Mag | ±Qtz, Cal-veins, Ni-sepiolite | Atg–Di–Dol-Chl in equilibrium in matrix, but also Atg/Chl pods and fragments occur |
| Cpx-serpent-inite[a] | Atg+Di+Mag±Chl±TiCl±Ol±Dol±Tr±Cal | ±Tlc, Cal-veins, Qtz | Anastomosing schistosity, high TiCl+Chl content when wrapping marble lenses. Dusty Di+Mag after Cpx /±Ilm, Pn |
| Atg-serpent-inite | Atg+Mag±TiCl±Cal | Cal | Massive with no visible schistosity; Atg shape-preferred orientation / ±Ilm, Pn |
| Dol-Atg-schist | Atg+Dol+Mag±Mgs | | Very schistose with stretched flat domains of Dol-Atg intergrowth; Dol has oscillatory zoning |
| Carbonate-Tr–Chl veins (zones rim to center) | (host): Atg+Cal-Dol-Mgs+Mag (I): Chl+Cal+Tlc+Atg+Dol+Mag±Hem ±Ilm±Mgs (II): Chl+Tlc+Dol±Tr±Mag±Hem (III): Tr+Chl+Dol±Cal±Hem | Fe-hydroxides | Calcite porphyroblasts in serpentinite close to veins contain Mgs-inclusions and Dol intergrowth; Grain sizes of Tr, Chl, Dol increase towards vein center |
| *Almirez* | | | |
| Meta-ophicar-bonate[b] (granofelsic) | Di+Dol+Cal+Ol+Chl+TiCl+Mag ±TiChn±Pn±Arg | Cal, Srp (Lz) | Granofelsic, with coarse Ol-porphyrob-lasts with Arg, Dol, Chl and Mag inclusions |
| Meta-ophicar-bonate[b] (gneissic) | Di+Dol+Chl+TiCl+Mag±TiChn | ±Srp, Tr, Qtz-Cal-veins | Gneissic banding, with coarse TiCl-por-phyroblasts /±Pn as inclusions in TiCl |
| Tr–Di–Dol rock[b] (SN-143) | Tr+Dol+Di+Chl±Mgs±Ilm/Chr | Cal; Tr–Dol (?) | Raft within carbonate breccia lens; Di as inclusions in Tr |
| Tlc-Mgs rock | Mgs+Tlc+Chl+Dol+Cal±Ilm | Cal; Tlc-Chl? | Penetrative foliation of Tlc-Chl aggregates parallel to gneissic meta-ophicarbonate; late replacement of Mgs by Cal. /±Rt, Ap |
| Mgs-Tr rocks/ veins | Mgs+Tr+Chl+Mag±TiCl±Dol, Cal | ±Cal | Very coarse-grained, euhedral Mgs and Tr |
| Dol-marble | Dol+Phl+Qtz±Cal±Phg±Tlc±Drv ±Plag±Tr±Zoi±Als | | Different Dol-marble assemblages constitute the majority of clasts in breccia /±Rt, Ttn, Ap |
| Carbonate breccia (matrix assemblage) | Cal+Tr+Dol+Chl+Chl+Phl±Tlc±Drv±Qtz | (?) | Mineral fragments in Cal-matrix |
| Carbonate breccia (rock fragments, clasts) | Dol-marble; Tr–Di–Dol rock; Chl–Tr-rock; chloritite; Tr–Ol–Atg–Chl rock; Chl-harz-burgite; coarse dolomite | | Angular to rounded, metre-sized rafts to millimetre-scale clasts; matrix-supported |

Minerals are listed in order of decreasing abundance. Mineral abbreviations throughout the paper are given following the recommendations by the IUGS Subcommission on the Systematics of Metamorphic Rocks (Siivola & Schmid, 2007), with the exception of titano-clinohumite (TiCl) and titano-chondrite (TiChn).

[a]Lithologies directly associated with marble lenses within serpentinite (Milagrosa). [b]Meta-ophicarbonate lenses (Almirez).
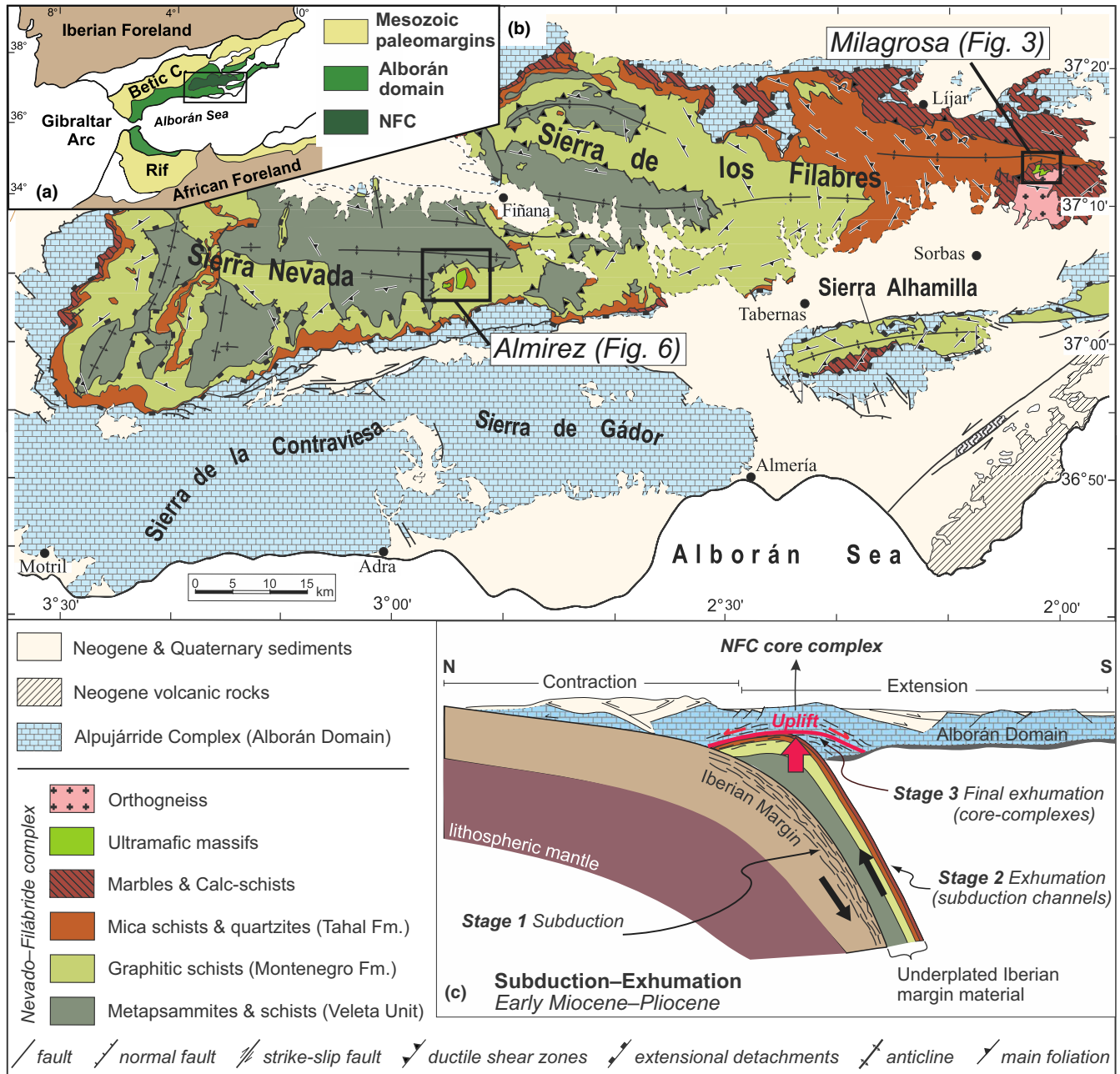
**FIGURE 2** (a) Location of the Nevado-Filábride Complex (NFC) in the Betic–Rif belt (modified from Jabaloy-Sánchez et al., 2015). (b) Geological map of the NFC in the central part of the Betic Cordillera (South Spain), with location of the two studied ultramafic massifs Almirez and Milagrosa; modified from Martínez-Martínez, Torres-Ruiz, Pesquera, and Gil-Crespo (2010). (c) Conceptual sketch of subduction and exhumation of the NFC (after Dilissen et al., 2018; modified from Behr & Platt, 2012)

Mediterranean (Hinsbergen, Vissers, & Spakman, 2014). In the middle Miocene, the margin was subducted below the Alborán domain and metamorphic rocks of the NFC rapidly exhumed in a two-stage process, first along the subduction interface and finally exhumed along E–W extensional domes now exposed in the Sierra Nevada, Sierra de los Filabres and Sierra Alhamilla ranges (Figure 2c) (Booth-Rea et al., 2015; Platt et al., 2013).

The NFC is subdivided into the lower Veleta unit, made up of graphite-bearing mica schists and metapsammites and the upper Mulhacén unit, composed of Paleozoic dark schists (Montenegro

formation), light schists (Tahal formation) and an upper heterogeneous sequence of alternating marbles, calc-schists, mica schists, and gneisses (Figure 2b; Gómez-Pugnaire et al., 2012). Intercalated in this sequence occur several ultramafic bodies of variable size (up to 2.3 km²), mainly composed of Atg-serpentinite and Chl-harzburgite (Gómez-Pugnaire et al., 2012; Jabaloy-Sánchez et al., 2015; Padrón-Navarta et al., 2011). The Milagrosa and Almirez ultramafic massifs crop out in the uppermost part of the NFC and are located in the eastern Sierra de los Filabres and eastern Sierra Nevada, respectively (Figure 2b).

# 3 | META-OPHICARBONATES IN THE NFC ULTRAMAFIC MASSIFS

## 3.1 | The Milagrosa ultramafic massif

### 3.1.1 | Field relations and sampling

The Milagrosa ultramafic massif consists of massive to schistose Atg-serpentinite, hosting variably sized marble lenses. The massif is tectonically bounded by metasediments (garnet–mica schists and phlogopite–quartz marbles) and metabasites (garnet-amphibolites with intercalations of garnet-bearing quartz-calcite schists) from the uppermost Mulhacén unit (Figure 3a). The internal structure of this massif is well exposed in the Milagrosa quarry (Figure 3b). In the NW of the quarry, the contact with garnet-mica schists and marbles is a fault composed of polymictic breccia grading into up to 10 m thick carbonated serpentinite breccia (Figure 3b). In the SE part of the quarry, a fine-grained brittle fault gauge zone separates the Atg-serpentinites from metabasites. The foliation of Atg-serpentinite—mostly N-020, dipping 70°–85° to NNE—is oblique to the contacts with the country rocks (Figure 3b).
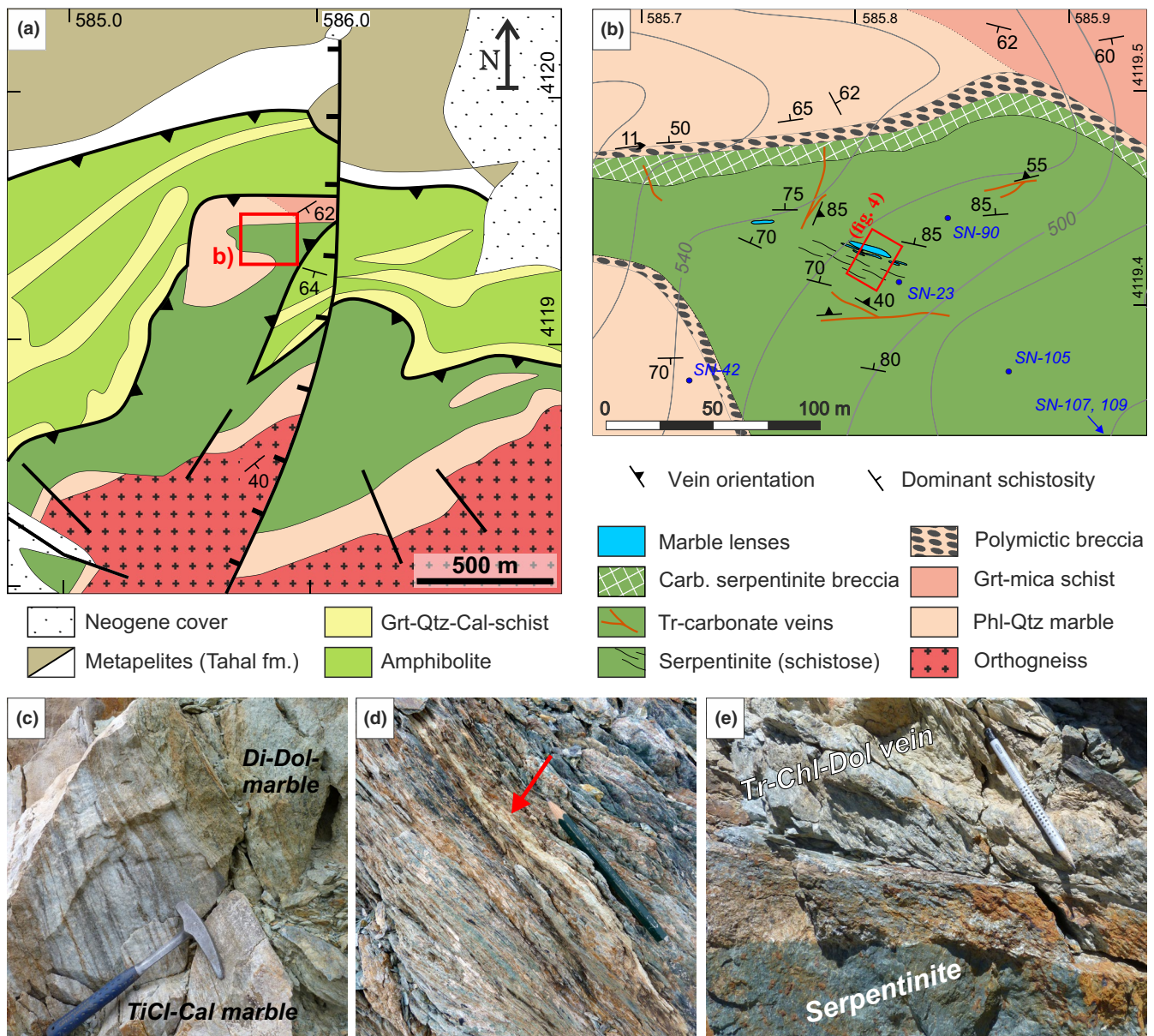


**FIGURE 3** Field relations in the Milagrosa serpentinite massif. (a) Geological map of the Milagrosa serpentinite massif (after Kampschuur & García Monzón, 1975). (b) Detailed geological map from inset in (a) of the Milagrosa serpentinite quarry with location of sampled marble lenses (red field; Figure 4) and Tr-carbonate veins. (c) Banded TiCl-Cal marble and Di–Dol marble lenses within serpentinite. (d) Cpx-serpentinite with brown weathering TiCl-porphyroblasts and carbonate vein (arrow). (e) Massive serpentinite crosscut by a zoned Tr–Chl-carbonate vein. Mineral abbreviations: see Table 1
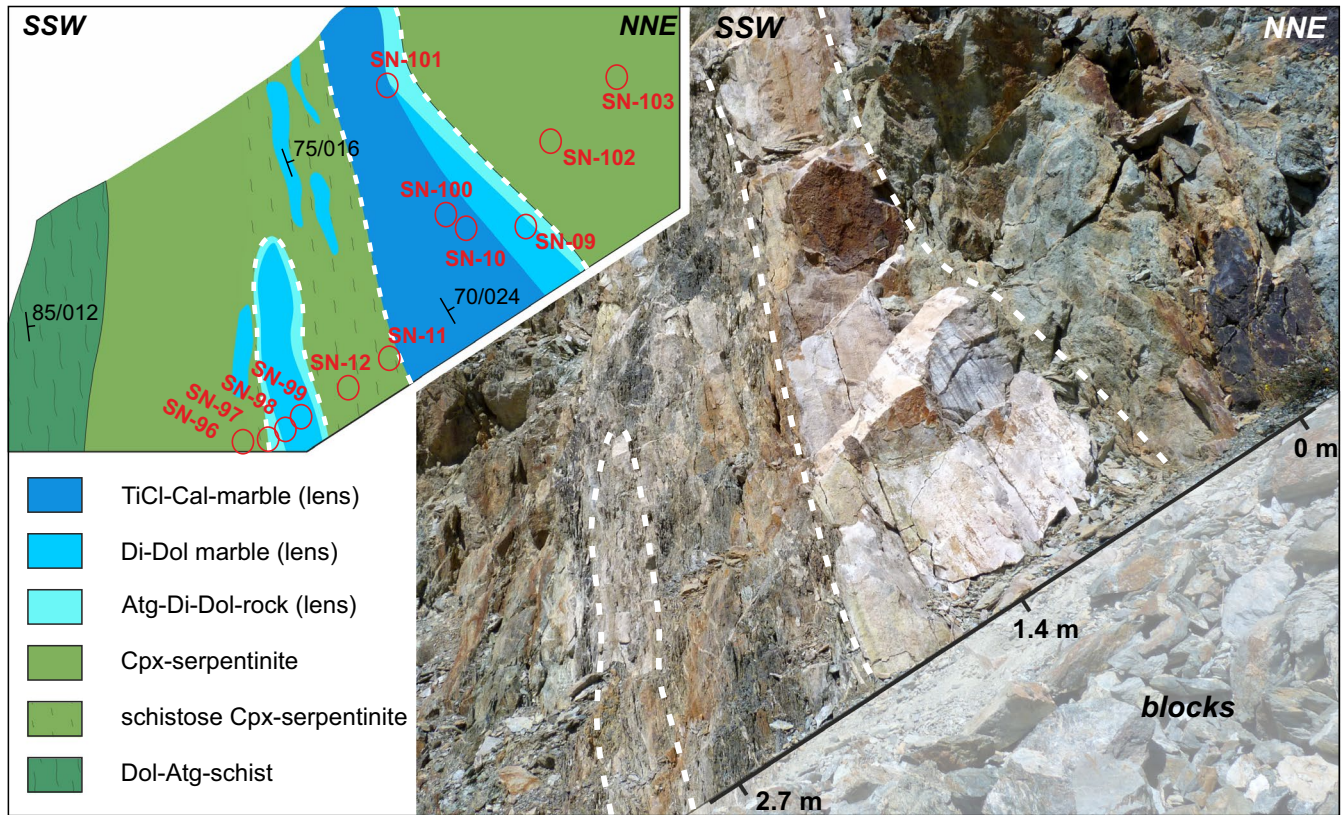
**FIGURE 4** Milagrosa marble lenses within foliated Cpx-serpentinite and corresponding sketch with sampling sites and small-scale lithological changes throughout the illustrated sequence (scale represents true thickness perpendicular to the schistosity)

For the present study, we sampled a sequence of marble lenses and host serpentinites in the central part of the Milagrosa quarry (Figure 4). Table 1 provides a description of the lithologies and their mineral assemblages. The marble lenses occur as boudins—20–130 cm thick and up to 20 m long—oriented sub-parallel to the mylonitic to schistose foliation of the enclosing Atg-serpentinite (Figure 3b) and show a compositional banding due to variations in the silicate mineral content (dark patches; Figure 3c) and relative proportion of calcite to dolomite (white and brown bands respectively; Figure 3c). We distinguish two types of marbles: TiCl-Cal marbles and impure Di–Dol marbles (Figure 4; see Table 1 caption for mineral abbreviations). Atg–Di–Dol rocks (5–20 cm thick) —composed of variable proportions of carbonate, light green diopside, chlorite-antigorite pods and minor magnetite and Ti-clinohumite (Table 1)—occur at the contact between marble and serpentinite (Figure 4).

The serpentinites are massive to foliated, fine-grained Atg-serpentinite and Cpx-serpentinite (Table 1). Atg-serpentinite contains scarce Ti-clinohumite porphyroblasts and veins and lacks olivine. In the vicinity of the marble lenses, dark Cpx-serpentinites with coarse grained, white patchy diopside-rich domains prevail (Figure 4). Towards the contact with the marble lenses, Cpx-serpentinite displays an increasingly penetrative schistose to mylonitic foliation defined by

fine-grained antigorite around Ti-clinohumite porphyroblasts, whitish coarse-grained diopside-rich domains (Figure 4) and, at the lens contact, almond-shaped diopside porphyroblasts. Well-foliated Dol-Atg schists with elongated dolomite-rich patches occur in a 7–10 m wide zone close to the marble lenses (Figure 4).

Carbonate-tremolite-chlorite veins (Table 1), up to 1.5 m thick, are cross-cutting at variable angles the Atg-serpentinite foliation (Figure 3e), and are in turn cross-cut by calcite veins (0.2–1 cm thick; Figure 3d). Because they overprint the prograde Atg-serpentinite foliation, veins are not considered in the present study.

### 3.1.2 | Petrography

TiCl-Cal marbles (Table 1; Figure 5a) are composed of calcite, minor diopside, chlorite, Ti-clinohumite, and dolomite. Accessory phases are apatite, Fe-oxides, pyrrhotite and occasional pyrite, pentlandite and ilmenite. Ilmenite occasionally contains rare Ca-perovskite cores and zirconolite and uraninite inclusions (Figure S1). The marbles show a weak foliation defined by oriented chlorite and a porphyroblastic texture made up of inclusion-rich Ti-clinohumite porphyroblasts with occasional Ti-chondrodite (TiChn) cores in a medium- to fine-grained matrix of calcite, diopside
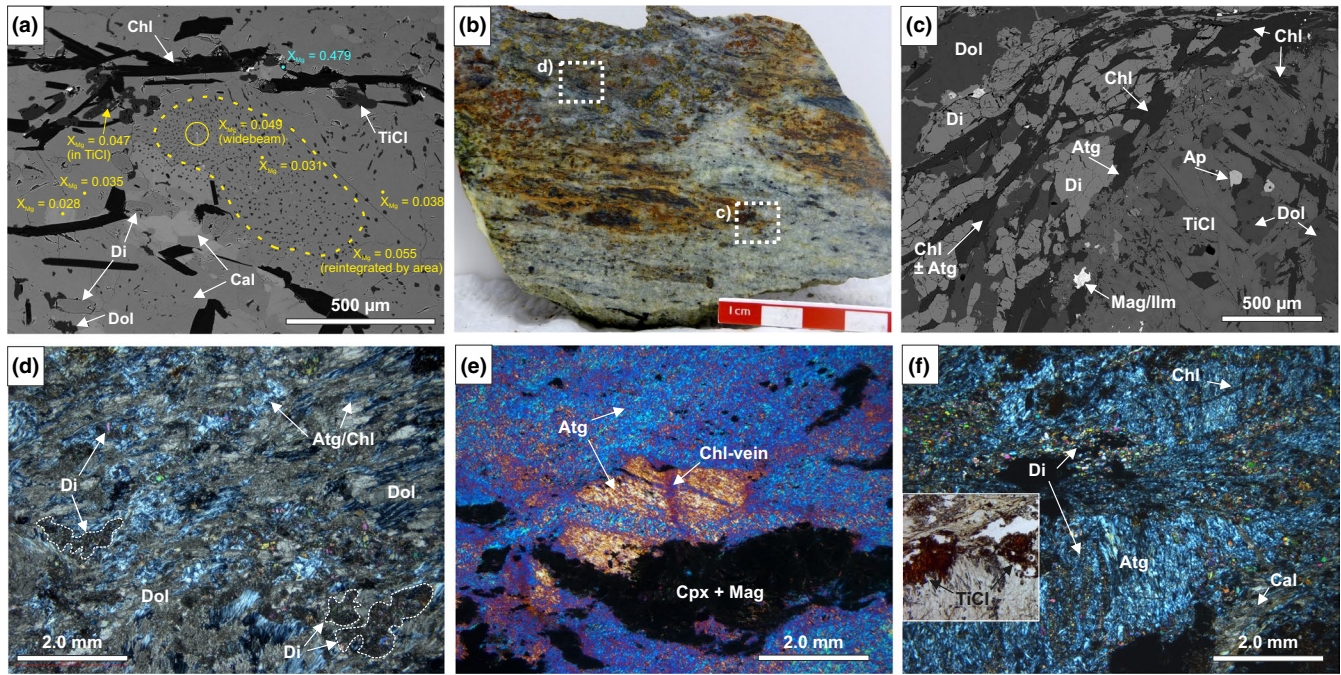
**FIGURE 5** Hand specimen, micrographs and back-scattered electron (BSE) images of host serpentinites, marble lenses and Atg–Di–Dol rocks from Milagrosa. (a) BSE image of TiCl-calcite marble lens displaying the measured $X_{\text{MgCO}_3}$ of carbonates; dolomite forms fine-grained exsolutions from calcite. (b) Polished slab of Atg–Di–Dol rock with darker Atg–Chl domains and red-brown Ti-clinohumite in a Di–Dol-matrix; the approximate positions of micrographs in (c) and (d) are also shown. (c) BSE image of an inclusion-rich Ti-clinohumite-porphyroblast wrapped by diopside, dolomite, chlorite and minor antigorite. (d) Atg–Di–Dol-rock with aligned Atg–Chl aggregates and diopside-rich domains (white dotted lines) (crossed polarizers). (e) Cpx-serpentinite, showing dusty resorbed clinopyroxene–magnetite porphyroblasts and antigorite domains with differing preferred orientation crosscut by chlorite veins, likely after bastite (crossed polarizers with inserted compensator). (f) Cpx-serpentinite rich in chlorite and red-brown Ti-clinohumite (plane polarized inset, at the same position) and diopside neoblasts aligned with antigorite in almond-shaped domains and diopside and chlorite aligned with antigorite in narrow anastomosing bands (crossed polarizers)

and chlorite. Dolomite occurs as small, spotty to vermicular exsolutions in calcite (Figure 5a) and as large resorbed, inclusion-rich aggregates. Quartz occurs as fine-grained retrograde aggregates around Ti-clinohumite or diopside.

Di–Dol marbles are composed of diopside, dolomite and chlorite, minor euhedral tremolite, calcite, magnetite–ilmenite intergrowths, apatite, talc, and rare antigorite. Yellow, pleochroic Ti-clinohumite porphyroblasts occur in domains where tremolite is absent, embedded in a granoblastic matrix.

Atg–Di–Dol rocks (Table 1; Figure 5b–d) have a very heterogeneous modal composition at the hand specimen scale. Diopside, dolomite and antigorite-chlorite aggregates display a weak shape-preferred orientation forming an anastomosing foliation with occasional Ti-clinohumite porphyroblasts with abundant inclusions of dolomite, chlorite, apatite and magnetite-ilmenite intergrowths (Figure 5c). Diopside has inclusions of calcite, dolomite and rare antigorite. Cr-bearing magnetite occurs as porphyroblasts or elongated aggregates of smaller grains. Magnetite porphyroblast cores commonly have abundant chlorite inclusions, while their rims and smaller grains are free of inclusions and occasionally replaced by hematite (Figure S1). Magnetite in the host serpentinites shows

similar textures. Antigorite and chlorite form fine intergrowths with an interlocked texture.

Atg-serpentinites show a weak foliation marked by the shape-preferred orientation of antigorite crystals and a lineation defined by elongated aggregates of anhedral magnetite (3–5 vol.%). Locally, domains of antigorite with an interlocked texture show a distinct shape and crystallographic preferred orientation (Figure 5e). Rare ilmenite-magnetite intergrowths, Ni–Fe–sulphides and Ti-clinohumite—as fragmented grains or in veins—are present (Table 1).

Cpx-serpentinites have a planar texture marked by elongated clinopyroxene aggregates, flattened magnetite and a weak shape-preferred orientation of antigorite. They contain abundant porphyroblasts of dusty and clear clinopyroxene (5–10 vol.%)—often associated with magnetite—, minor chlorite (1–3 vol.%), and rare calcite and tremolite. Near the marble lenses, the modal amounts of diopside (up to 30 vol.%), chlorite (10–20 vol.%), Ti-clinohumite (5–8 vol.%) and minor carbonates increase. Narrow to anastomosing bands of strongly oriented antigorite intersect and wrap around coarse diopside-magnetite aggregates, euhedral Ti-clinohumite porphyroblasts and almond-shaped domains of antigorite with a different orientation (Figure 5f). Elongated aggregates of

diopside neoblasts and chlorite are parallel to the antigorite orientation in bands and almond-shaped domains (Figure 5f). Ti-clinohumite porphyroblasts contain inclusions of chlorite, dolomite and clinopyroxene, and are occasionally rimmed by fine-grained olivine. Rare, red-brown Ni-bearing Fe-Si-aggregates occur in the antigorite matrix, occasionally rimming sulphides and magnetite. Similar Fe–Ni–Si-aggregates are common in HP-serpentinites elsewhere (Malvoisin et al., 2017).

Dol–Atg schists (Table 1) consist of strongly oriented antigorite and flattened domains of magnetite, dolomite and coarse-grained, interlocked antigorite. Magnesite, pentland-ite and cronstedtite are accessory phases.

## 3.2 | The Almirez Massif

### 3.2.1 | Field relations and sampling

The Almirez ultramafic massif is a dismembered section of subducted serpentinite, comprising Atg-serpentinites and their prograde dehydration products, Chl-harzburgites (Figure 6a; Padrón-Navarta et al., 2011; Trommsdorff, López Sánchez-Vizcaíno, Gomez-Pugnaire, & Müntener, 1998). Minor meta-rodingites, clinopyroxenites and carbonate lenses are also present. A sharp isograd—oblique to the prograde HP antigorite-serpentinite foliation—records the HP dehydration of Atg-serpentinite to Chl-harzburgite
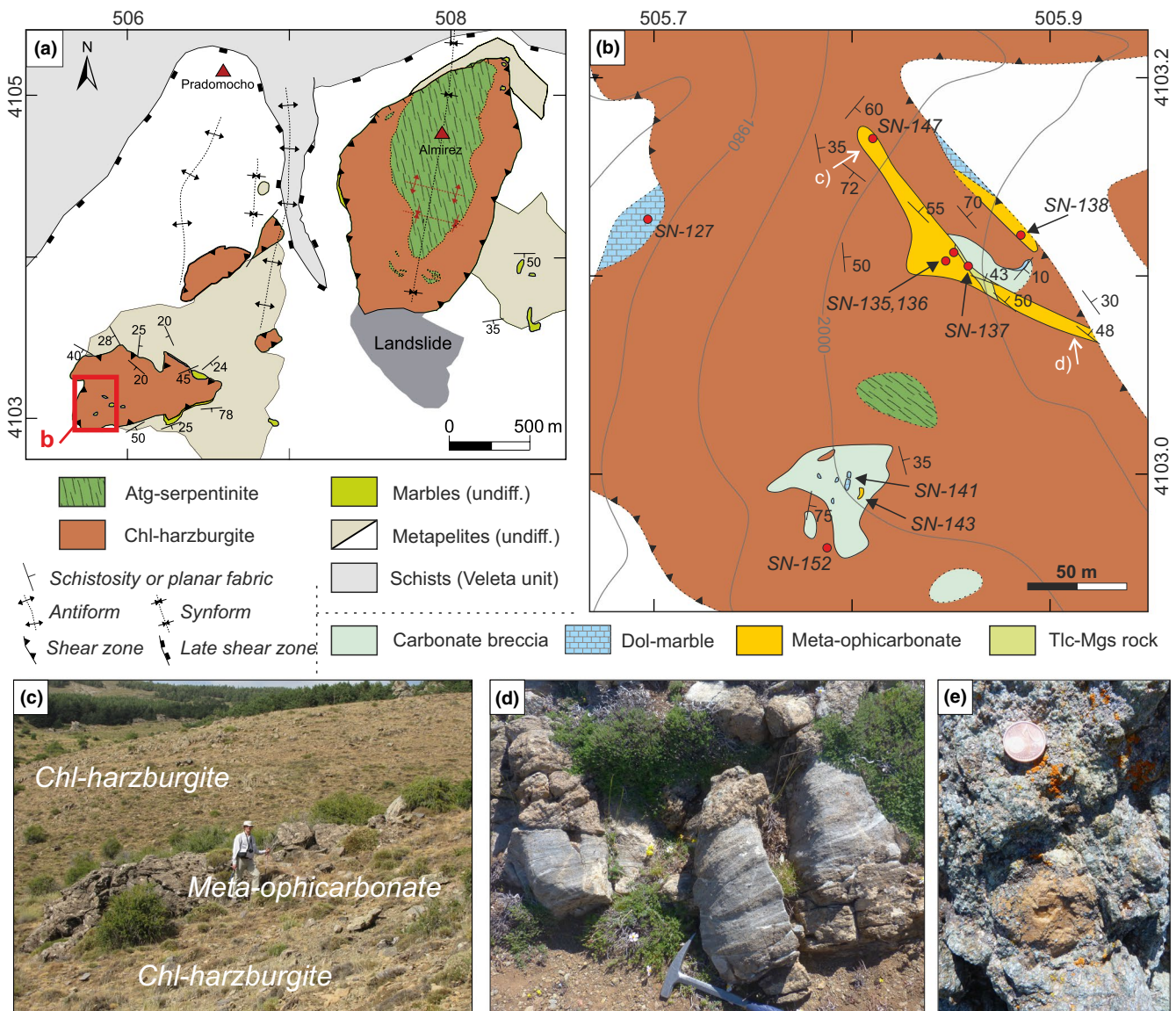


**FIGURE 6** Meta-ophicarbonate lenses within Chl-harzburgite at Almirez. (a) Geological map of the Almirez ultramafic massif (after Jabaloy-Sánchez et al., 2015). (b) Detailed geological map of carbonate lenses in Chl-harzburgite and key sample locations (inset in a); the locations of field pictures (c) and (d) are marked by white arrows. (c) Field picture of the Almirez meta-ophicarbonate lens hosted in Chl-harzburgite. (d) Coarse-grained, granofelsic meta-ophicarbonate rich in olivine and Ti-clinohumite (yellowishbrown in colour), crosscut by gneissic dolomite-dominated meta-ophicarbonate (grey colour). (e) Tlc-Mgs rock with coarse brown magnesite blasts (coin for scale is 2 cm)

(1.8–1.9 GPa, ~660°C) (López Sánchez-Vizcaíno, Gómez-Pugnaire, Garrido, Padrón-Navarta, & Mellini, 2009; Padrón-Navarta, Hermann, et al., 2010).

Carbonate-bearing lithologies occur in the western part of the Almirez Chl-harzburgite section, as lenses of yellow, banded dolomite marble, polymictic carbonate breccia and meta-ophicarbonate (Table 1; Figure 6a,b). The dolomite marbles contain rather simple mineral assemblages (tremolite, quartz; see Table 1) and make up the majority of rock fragments in the carbonate breccias (Table 1). Here, we focus on two lenses of meta-ophicarbonate (5–10 m thick; yellow lenses in Figure 6b,c). The meta-ophicarbonates show a coarse-grained, granofelsic texture with Ti-clinohumite and olivine porphyroblasts (up to 1 cm) and a weak modal layering sub-parallel to the lens elongation (Figures 6b and 7a). The granofelsic meta-ophicarbonate contains grey banded levels (30–50 cm thick) with a gneissic texture (Figures 6d and 7b). Locally, Tlc–Mgs rocks (3–5 m thick) with abundant euhedral magnesite crystals (up to 5 cm) occur in the meta-ophicarbonates (Figure 6b,e; Table 1). Talc-chlorite aggregates in these rocks show a penetrative foliation sub-parallel to the gneissic foliation and the modal layering of the meta-ophicarbonates.

The contact of Chl-harzburgite with meta-ophicarbonate is not well exposed. Chl-harzburgite surrounding the meta-ophicarbonate lenses has—like in other parts of the Almirez massif (Padrón-Navarta et al., 2011)—spinifex and granofels textures and is commonly recrystallized (Figure 6b; Padrón-Navarta, Tommasi, Garrido, & López Sánchez-Vizcaíno, 2012; Padrón-Navarta, Tommasi, et al., 2010). Magnesite- and dolomite-bearing Tr–Chl–TiCl–Ol-rocks (e.g. sample SN-152 in Figure 6b) and Ti-clinohumite bearing magnesite–tremolite–chlorite veins occur locally in Chl-harzburgite.

### 3.2.2 | Petrography

The Almirez meta-ophicarbonates consist of carbonate (~25–45 vol.%; dolomite, calcite and rare aragonite), diopside, olivine, Ti-clinohumite/-chondrodite, chlorite and minor Cr-magnetite, pentlandite, pyrrhotite, and apatite (Table 1). The meta-ophicarbonates show a planar texture marked by chlorite and weakly oriented diopside and dolomite (Figure 7c,d) around olivine and Ti-clinohumite porphyroblasts. Grain boundaries are mostly polygonal

between all phases. Domains richer in diopside, olivine or carbonate, respectively, constitute a modal layering parallel to this planar texture (Figure 7d). Calcite is rare in some coarse-grained dolomite-rich domains (Figure 7e) and gneissic intercalations (Figure 7b; Table 1). The latter further contain rare olivine and sulphides. Ti-clinohumite, olivine and diopside have abundant inclusions of chlorite, calcite, dolomite and, locally, magnetite, sulphides and apatite (Figure 7c–g). Furthermore, electron backscatter diffraction (EBSD) and energy-dispersive spectrometry (EDS) analyses have revealed the presence of aragonite inclusions (5–30 μm in size) in olivine and diopside (Figure 7f–h). Yellow pleochroic Ti-clinohumite porphyroblasts occasionally have TiChn cores and olivine rims (Figure 7c). Cr-bearing magnetite occurs as coarse, elongated aggregates with abundant chlorite inclusions and as inclusion-free rims and subhedral grains in the granoblastic matrix (Figure S1). Lizardite locally replaces Ti-clinohumite and olivine porphyroblasts along veins and grey–black pleochroic rims (Figure 7c,h). Calcite, quartz and tremolite occur locally in veins (0.5–2.0 mm thick) crosscutting the layering.

Meta-ophicarbonate clasts in carbonate breccia (sample SN-143; Table 1) are composed of dolomite, tremolite, chlorite, minor diopside and rare magnesite, Fe-oxide, chromite–ilmenite intergrowths, and apatite. They have a well-developed gneissic texture marked by chlorite orientation and tremolite- and dolomite-rich bands.

The Tlc-Mgs level (Table 1) is made up of coarse magnesite (up to 5 cm; Figure 6e) rimmed by calcite and dolomite and minor chlorite-talc aggregates. Ilmenite, rutile and apatite are accessory phases; Cr-bearing phases (Cr-magnetite or chromite) are absent. Almond-shaped chlorite-talc aggregates define a penetrative foliation.

The host Chl-harzburgites have similar textures and mineral assemblages as elsewhere in the massif (Padrón-Navarta et al., 2011) and are occasionally overprinted by chrysotile/lizardite serpentinization. Tr–Chl–TiCl–Ol-rocks consist of olivine, Ti-clinohumite, chlorite and tremolite and minor magnetite, magnesite and dolomite (~5 vol.% carbonates). Magnesite occurs as coarse interstitial grains rimmed by dolomite and tremolite has inclusions of diopside, indicating that the peak assemblage was TiCl–Ol–Chl–Di–Mgs and tremolite and dolomite formed after diopside and magnesite in the retrograde path.

**FIGURE 7** Petrography of Almirez meta-ophicarbonates. (a) Polished slab of massive meta-ophicarbonate with large red-brown Ti-clinohumite and olivine in a carbonate-diopside-chlorite matrix (sample SN-135). (b) Polished slab of a banded, olivine-poor sample with gneissic appearance (sample SN-136). (c) Micrograph of meta-ophicarbonate in (a); the insets correspond to the positions of the chemical and phase maps in (f), (g) and (h). (d) EBSD phase map showing representative mineral distribution in meta-ophicarbonate (sample SN-135). (e) EBSD phase map of coarse, calcite-poor meta-ophicarbonate (sample SN-147; colour legend as in d). (f) and (g) Chemical false-colour map (EDS) superposed on band-contrast and corresponding EBSD phase map of diopside with aragonite inclusions. (h) EBSD phase map of inset in (d), showing preserved aragonite (red) and re-equilibrated calcite inclusions within olivine crosscut by lizardite veins. White areas in all EBSD phase maps (non-indexed) are mainly chlorite and lizardite
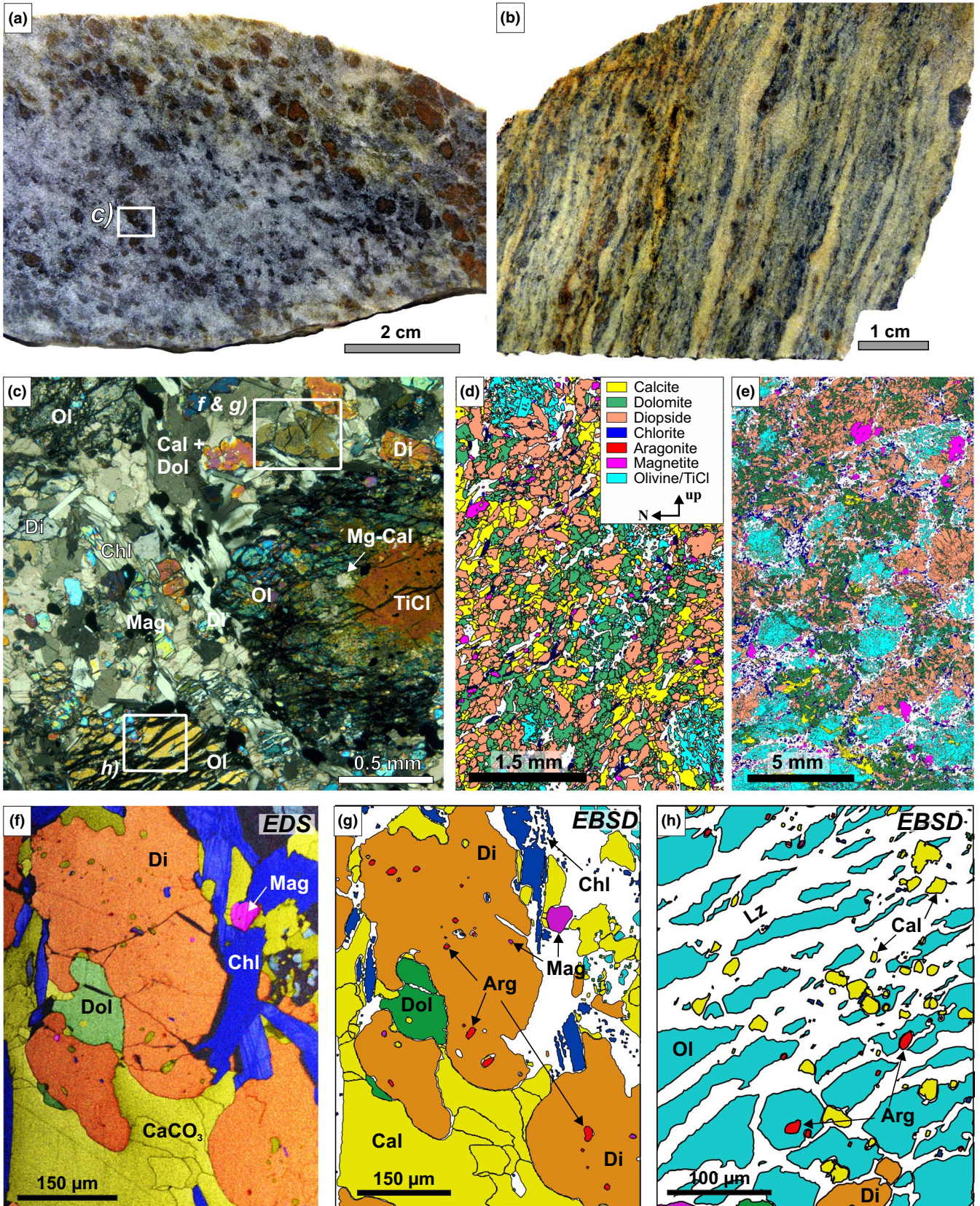
**TABLE 2** Whole-rock major element compositions of the serpentinites, marbles and meta-ophicarbonates from Milagrosa and Almirez; analysed by XRF (major and minor elements), IR-spectroscopy (C, S), potentiometric titration (FeO$_{(titr)}$) and Chittick apparatus (calcite & dolomite fractions). Oxides and S are given in wt%; Cr, Co, Cu, Ni, V, and Zn in ppm

| Locality | Milagrosa | | | | | | | | | | | | | |
|---|---|---|---|---|---|---|---|---|---|---|---|---|---|---|
| Lithology | Dol-Atg schist | Atg-serpentinite | | Cpx-serpentinite | | | | | Atg-Di-Dol rock | | Di-Dol marble | | TiCl-Cal marble | |
| Sample | SN-23 | SN-107 | SN-109 | SN-90 | SN-96 | SN-105 | SN-102 | SN-11 | SN-97 | SN-98 | SN-99 | SN-09 | SN-101 | SN-10 |
| SiO$_2$ (wt%) | 40.35 | 39.15 | 39.95 | 39.46 | 39.44 | 40.34 | 42.22 | 32.03 | 29.87 | 24.23 | 19.10 | 13.72 | 5.36 | 3.59 |
| TiO$_2$ | 0.01 | 0.09 | 0.11 | 0.11 | 0.13 | 0.10 | 0.05 | 0.21 | 0.10 | 0.08 | 0.09 | 0.09 | 0.01 | 0.01 |
| Al$_2$O$_3$ | 0.84 | 2.94 | 3.07 | 3.44 | 3.39 | 3.36 | 2.79 | 3.08 | 2.52 | 2.11 | 2.25 | 2.03 | 0.65 | 0.53 |
| Fe$_2$O$_3$ [a] | 5.73 | 5.87 | 4.74 | 6.33 | 6.26 | 5.08 | 5.37 | 3.79 | 3.75 | 2.78 | 1.64 | 1.38 | 0.57 | 0.35 |
| FeO $_{(titr)}$ | 1.82 | 2.06 | 2.69 | 2.43 | 1.90 | 3.20 | 1.94 | 1.80 | 1.23 | 1.15 | 1.07 | 1.05 | 0.48 | 0.27 |
| MnO | 0.10 | 0.09 | 0.11 | 0.12 | 0.11 | 0.12 | 0.07 | 0.08 | 0.10 | 0.11 | 0.08 | 0.12 | 0.11 | 0.11 |
| MgO | 37.02 | 37.00 | 36.73 | 34.98 | 34.92 | 35.11 | 31.69 | 28.11 | 27.00 | 22.05 | 18.52 | 19.52 | 6.44 | 3.88 |
| CaO | 0.32 | 0.11 | 0.03 | 1.64 | 1.17 | 1.04 | 3.33 | 12.32 | 13.89 | 22.23 | 28.21 | 27.59 | 45.55 | 49.72 |
| BaO | b.d. | b.d. | b.d. | b.d. | b.d. | b.d. | b.d. | b.d. | b.d. | b.d. | b.d. | b.d. | b.d. | b.d. |
| Na$_2$O | b.d. | b.d. | 0.06 | b.d. | 0.09 | 0.03 | b.d. | b.d. | b.d. | b.d. | 0.02 | b.d. | b.d. | b.d. |
| K$_2$O | 0.01 | 0.01 | 0.01 | 0.01 | 0.02 | 0.01 | 0.01 | 0.01 | 0.01 | 0.01 | 0.01 | b.d. | b.d. | b.d. |
| P$_2$O$_5$ | 0.002 | 0.003 | 0.009 | 0.004 | 0.002 | 0.005 | b.d. | 0.019 | 0.008 | 0.009 | 0.015 | 0.015 | 0.007 | 0.004 |
| LOI | 12.80 | 11.90 | 11.98 | 10.97 | 11.94 | 11.37 | 12.22 | 17.88 | 21.16 | 24.83 | 28.87 | 33.92 | 40.43 | 41.09 |
| S | 0.004 | 0.005 | b.d. | b.d. | 0.013 | 0.015 | b.d. | 0.028 | b.d. | 0.008 | b.d. | b.d. | b.d. | 0.028 |
| CO$_2$ (TC) | 0.55 | 0.12 | 0.03 | 0.04 | 0.61 | 0.03 | 2.19 | 10.08 | 13.82 | 21.16 | 26.40 | 30.01 | 39.31 | 40.88 |
| Cr (ppm) | 2600 | 2532 | 2326 | 2942 | 2395 | 2463 | 3079 | 1642 | 1505 | 1026 | 411 | 342 | 137 | 68 |
| Co | 109 | 94 | 88 | 87 | 80 | 93 | 51 | 67 | 42 | 34 | 18 | 23 | b.d. | b.d. |
| Cu | b.d. | b.d. | 27 | 15 | 26 | b.d. | 24 | b.d. | 21 | b.d. | b.d. | b.d. | b.d. | b.d. |
| Ni | 2320 | 1877 | 1506 | 1946 | 2423 | 3570 | 1696 | 1438 | 989 | 805 | 419 | 450 | 243 | 64 |
| V | 34 | 67 | 63 | 78 | 78 | 74 | 69 | 55 | 49 | 39 | 35 | 31 | 15 | 13 |
| Zn | 45 | 36 | 51 | 51 | 51 | 51 | 55 | 45 | 31 | 26 | 18 | 19 | 9 | 7 |
| *Total* | 99.63 | 99.81 | 100.00 | 100.14 | 99.98 | 100.51 | 100.32 | 99.73 | 99.97 | 99.83 | 99.98 | 99.54 | 99.66 | 99.58 |
| Fe$^{3+}$/Fe$_{total}$ | 0.74 | 0.72 | 0.61 | 0.70 | 0.75 | 0.59 | 0.71 | 0.65 | 0.73 | 0.69 | 0.58 | 0.54 | 0.52 | 0.54 |
| *FeO$_{model}$* [b] | | | 1.47 | 1.24 | | | | | 1.49 | 0.92 | | | 0.90 | 0.12 |
| X$_{Serp}$ [c] | 0.99 | 1.00 | 1.00 | 0.99 | 0.98 | 0.99 | 0.95 | 0.80 | 0.74 | 0.58 | 0.47 | 0.45 | 0.16 | 0.09 |
| Cal (wt%) | | | | | | | | | 12.67 | 17.71 | 24.20 | 35.29 | 35.83 | 73.08 | 84.13 |
| Dol (wt%) | | | | | | | | | 10.67 | 12.59 | 34.09 | 24.32 | 30.05 | 11.36 | 8.18 |
| Cal/Dol ratio | | | | | | | | | 1.19 | 1.41 | 0.71 | 1.45 | 1.19 | 6.43 | 10.28 |
| Carb. fraction | | | | | | | | | 0.23 | 0.30 | 0.58 | 0.60 | 0.66 | 0.84 | 0.92 |

b.d.: below detection limit; n.a.: not analysed; LOI: loss on ignition (corrected for oxidation gain).
[a]Fe$_2$O$_3$ by difference from total Fe$_2$O$_3$ (XRF) and FeO (determined separately). [b]Estimated effective FeO used in pseudosection models after subtracting magnetite and Fe$^{3+}$ in antigorite (estimated by mass-balance and image analysis; c.f. Sec. 4.4). [c]X$_{Serp}$ = projected position on the compositional mixing vector serpentinite-calcite used in Fig. 15 [calculated as $\sum$ (Mg, Si, Al, Fe, H$_2$O) / $\sum$ (Mg, Si, Al, Fe, H$_2$O, Ca, CO$_2$)]

# 4 | METHODS

## 4.1 | Bulk rock analyses

Rock chips were cut from homogeneous and non-weathered parts of the samples, cleaned in distilled water ultrasonic bath, crushed in a jaw crusher and powdered (<50 μm mesh) in an agate vibratory ring mill. Analyses were carried out at the GeoLabs of the Ontario Geological Service (Canada) (Table 2). Major elements (ISO-accredited) and Co, Cu, Cr, Ni, V, and Zn were analysed using XRF on fused glass beads. Ferrous iron was determined by potentiometric titration and total carbon and sulphur by furnace infrared absorption. Absolute carbonate amounts and the relative fractions of Ca-carbonate versus Dolomite/Mg-carbonate were analysed using a Chittick apparatus (Dreimanis, 1962). Duplicate analyses of sample aliquots show reproducibility better than 3% for most elements. The accuracy of major elements analyses is better than 5% for most elements as deduced from analyses of the reference materials dolomite JDo-1 (Geological Society of Japan) and calcareous sandstone Ou-8 (International Association of Geoanalysts).

| Calc-schist | | Almirez Meta-ophicarbonate | | | | Tlc-Mgs rock | Tr-Mgs rock | Dol-marble | | | | (Carb-bearing) Chl-harzburgite | | | |
|---|---|---|---|---|---|---|---|---|---|---|---|---|---|---|---|
| SN-30 | SN-42 | SN-143 | SN-136 | SN-135 | SN-138 | SN-137b | SN-131 | SN-124 | SN-127a | SN-141 | SN-130 | SN-128 | SN-134 | SN-139 | SN-146 |
| 41.57 | 34.70 | 26.42 | 25.18 | 23.26 | 25.74 | 8.52 | 14.44 | 2.92 | 2.27 | 2.73 | 6.35 | 41.93 | 36.92 | 38.34 | 41.45 |
| 0.19 | 0.05 | 0.07 | 0.03 | 0.03 | 0.06 | 0.12 | 0.17 | 0.01 | 0.02 | 0.02 | 0.12 | 0.05 | 0.03 | 0.05 | 0.08 |
| 4.21 | 1.14 | 2.19 | 1.86 | 1.94 | 2.29 | 2.30 | 5.12 | 0.41 | 0.46 | 0.46 | 2.64 | 2.59 | 2.09 | 1.68 | 2.82 |
| 1.13 | 0.29 | 1.14 | 3.65 | 3.33 | 4.06 | 2.38 | 1.89 | 0.04 | 0.00 | 0.42 | 1.28 | 3.63 | 3.73 | 6.07 | 5.91 |
| 0.91 | 0.22 | 1.37 | 2.09 | 2.09 | 2.25 | 1.77 | 2.88 | 0.30 | 0.23 | 0.15 | 1.89 | 4.24 | 2.72 | 2.15 | 2.67 |
| 0.31 | 0.01 | 0.06 | 0.12 | 0.13 | 0.13 | 0.26 | 0.11 | 0.04 | 0.04 | 0.03 | 0.09 | 0.09 | 0.07 | 0.10 | 0.10 |
| 0.66 | 1.80 | 17.92 | 18.61 | 21.17 | 23.47 | 25.65 | 28.47 | 20.26 | 20.30 | 14.74 | 14.79 | 37.84 | 32.38 | 34.50 | 32.81 |
| 26.90 | 32.69 | 26.44 | 23.73 | 24.10 | 20.87 | 19.64 | 12.98 | 29.26 | 29.75 | 35.94 | 32.50 | 0.04 | 5.82 | 1.27 | 3.83 |
| 0.01 | b.d. | b.d. | b.d. | b.d. | b.d. | 0.02 | 0.01 | b.d. | b.d. | b.d. | b.d. | b.d. | b.d. | b.d. | b.d. |
| 0.64 | 0.07 | 0.28 | 0.02 | b.d. | b.d. | b.d. | 0.05 | b.d. | b.d. | 0.03 | 0.17 | b.d. | b.d. | b.d. | 0.07 |
| 0.50 | 0.35 | 0.06 | 0.01 | 0.01 | 0.01 | 0.01 | 0.01 | 0.15 | 0.12 | 0.09 | 0.03 | 0.01 | 0.01 | 0.01 | 0.02 |
| 0.063 | 0.060 | 0.028 | 0.019 | 0.014 | 0.006 | 0.010 | 0.067 | 0.009 | 0.011 | 0.011 | 0.037 | 0.012 | 0.010 | 0.011 | 0.004 |
| 22.53 | 28.00 | 23.82 | 24.13 | 23.01 | 19.71 | 39.44 | 33.01 | 45.73 | 46.06 | 44.76 | 39.61 | 9.20 | 15.69 | 14.21 | 9.28 |
| b.d. | 0.022 | b.d. | b.d. | 0.120 | 0.182 | 0.007 | 0.013 | b.d. | b.d. | b.d. | b.d. | 0.025 | 0.010 | 0.008 | 0.103 |
| 21.87 | 28.40 | 22.07 | 21.88 | 19.63 | 16.50 | 38.26 | 28.97 | 46.15 | 44.72 | 45.85 | 39.24 | 0.48 | 4.72 | 1.20 | 0.65 |
| b.d. | b.d. | 1642 | 2189 | 2395 | 2874 | b.d. | 684 | b.d. | b.d. | b.d. | b.d. | 2668 | 1779 | 2600 | 2395 |
| 12 | b.d. | 38 | 83 | 146 | 120 | 93 | 124 | b.d. | b.d. | b.d. | 22 | 96 | 69 | 103 | 94 |
| 62 | b.d. | 43 | 74 | 36 | 15 | 46 | 404 | b.d. | b.d. | b.d. | b.d. | b.d. | b.d. | b.d. | b.d. |
| 27 | b.d. | 1077 | 1456 | 1659 | 2087 | 2002 | 4198 | b.d. | b.d. | 15 | 102 | 2078 | 1543 | 2362 | 1803 |
| 35 | 18 | 62 | 48 | 52 | 62 | 22 | 37 | 13 | 11 | 11 | 27 | 57 | 40 | 55 | 68 |
| 42 | 34 | 22 | 43 | 64 | 53 | 22 | 45 | 10 | 10 | 9 | 27 | 64 | 60 | 74 | 47 |
| 99.64 | 99.39 | 100.16 | 99.94 | 99.63 | 99.25 | 100.34 | 99.79 | 99.13 | 99.26 | 99.38 | 99.52 | 100.25 | 99.91 | 99.03 | 99.59 |
| 0.53 | 0.54 | 0.43 | 0.61 | 0.59 | 0.62 | 0.55 | 0.37 | 0.10 | 0.00 | 0.72 | 0.38 | 0.43 | 0.55 | 0.72 | 0.67 |
| | | | | | 1.25 | | | | | | | | | | |
| | | 0.51 | 0.54 | 0.57 | 0.63 | | | | | | | 0.99 | 0.91 | 0.98 | 0.96 |
| | 59.75 | 24.72 | 18.48 | 25.60 | 20.19 | | | 27.51 | 36.51 | 30.88 | 29.34 | | 7.82 | | |
| | 8.03 | 22.77 | 30.05 | 24.59 | 17.53 | | | 69.90 | 62.11 | 57.63 | 50.92 | | 6.38 | | |
| | 7.44 | 1.09 | 0.61 | 1.04 | 1.15 | | | 0.39 | 0.59 | 0.54 | 0.58 | | 1.23 | | |
| | 0.68 | 0.47 | 0.49 | 0.50 | 0.38 | | | 0.97 | 0.99 | 0.89 | 0.80 | | 0.14 | | |

## 4.2 | Electron microprobe analyses

Mineral chemistry was analysed using a JEOL JXA-8230 electron microprobe at the Scientific and Technological Center of the University of Barcelona (Spain) on carbon-coated thin sections. Typical analytical conditions and standards were adopted for silicate minerals (WDS spot analysis [1 μm], 20 kV excitation voltage, 10 nA beam current, using wollastonite [Ca, Si], corundum [Al], synthetic $Fe_2O_3$ [Fe], $Cr_2O_3$ [Cr], synthetic Ni [Ni], rutile [Ti], periclase [Mg], albite [Na], orthoclase [K], rhodonite [Mn], AgCl [Cl] and fluorite [F] as standards) and carbonate minerals (WDS widened beam [5–10 μm], 20 kV, 10 nA, with synthetic $CaCO_3$ [Ca] and $Fe_2O_3$ [Fe], periclase [Mg], rhodonite [Mn], barite [Ba], celestine [Sr] and wollastonite [Si] as standards). For silicates, peak measurement times of 10 s were used for Na, K, Mg, Ca, Al, Si, Mn, F, Cl; 20 s for Cr and Ti and 30 s for Ni. In carbonates, Si, Ca and Mg were measured for 10 s, Fe and Mn for 30 s, and Ba and Sr for 60 and 40 s, respectively. Major elements and volatile elements were analysed first and for short times to prevent possible volatilization or drift due to beam damage on carbonates and sheet silicates.

## 4.3 | Scanning electron microscopy analyses

We obtained EDS and EBSD maps using a Zeiss EVO MA 15 scanning electron microscopy (SEM) equipped with an Oxford Instruments 80 mm$^2$ X-Max$^N$ EDS silicon drift detector and Nordlys Nano EBSD at the Instituto Andaluz de Ciencias de la Tierra (IACT, Granada, Spain). The Oxford Instruments AZtec software platform was used for data acquisition and processing. Simultaneous EBSD–EDS maps were carried out in geographically oriented thin sections, using a standard setup (70° tilt, 24 mm working distance) in non-coated thin sections with a final colloidal silica polishing. EDS and EBSD maps were acquired at ~$10^{-5}$ mbar for most samples and at 10 Pa in carbonate-rich and serpentinite thin sections to avoid charging. For large area EBSD maps and depending on the grain size of the sample, we used step sizes of 4–15 μm. For high-resolution mapping of carbonate inclusions and fine-grained antigorite, we used step sizes of 0.8–1.5 μm. Mean angular deviations were in the range of 0.3–0.6° for carbonates, diopside and olivine and 0.7–0.9° for chlorite and antigorite. Misindexation of Ti-clinohumite and Ti-chondrodite as olivine was common.

Removal of wild spikes and successive filling of non-indexed pixels based on 8, 7 and 6 neighbouring pixel orientations, were performed during data treatment using the Oxford Channel 5 software. Misindexation of calcite and dolomite analyses induced by their close crystal symmetries were discriminated using the simultaneously acquired EDS spectra. Systematic misindexation of olivine (60° [100]), dolomite (180° [100]), calcite (60° [001]) and antigorite (60° and 120° [001]), was removed using the Channel 5 software rotation algorithm. The Matlab toolbox MTEX (version 4.5.2; Bachmann, Hielscher, & Schaeben, 2010) was used for grain boundary rendering (15° segmentation angle) and small grains removal (5 and 8 pixel threshold in high resolution and large area maps, respectively).

## 4.4 | Thermodynamic modelling

To investigate the *P–T* conditions of equilibration, phase relationships and equilibrium fluid composition, we calculated *P–T*, *T–X*$_{CO_2}$ and *T–X* pseudosections in the FeO–CaO–MgO–Al$_2$O$_3$–SiO$_2$–H$_2$O–CO$_2$ (FCMASHC) system using Perple_X 6.7.3 (Connolly, 2009). For these calculations, we used the internally consistent thermodynamic database of Holland and Powell (1998) (version 2002) and the compensated Redlich-Kwong (CORK) equation of state (Holland & Powell, 1991) for H$_2$O–CO$_2$ fluids, because they allow the consistent application of solid solution models, such as the antigorite model by Padrón-Navarta et al. (2013) that accounts for Al Tschermak's and Fe–Mg exchanges. All applied solid solution models and their references are provided in Appendix S1.

Because the available antigorite solid solution model does not consider Fe$^{3+}$ in antigorite, which may have Fe$^{3+}$/Fe$_{total}$ up to 0.7 (Debret et al., 2014), this solution model overestimates Al Tschermak's-exchange and may result in an erroneous prediction of brucite and olivine in detriment of chlorite. Due to this limitation, we estimated the amounts of Fe$_2$O$_3$ in antigorite and of magnetite in the bulk samples by mass balance and from the modal abundance in serpentinites, using Fe$^{3+}$/Fe$_{total}$ = 0.6 as an intermediate estimate for ferric iron in antigorite (Debret et al., 2015). The equivalent quantities of FeO and Fe$_2$O$_3$ were then subtracted from the bulk compositions, to obtain model FeO contents for bulk compositions in the FCMASH system (FeO$_{model}$ in Table 2). This subtraction improves the calculation of phase relations between olivine, clinopyroxene and tremolite in serpentinites with high bulk Fe$^{3+}$/Fe$_{total}$ at 500–650°C and reproduces the observed assemblage Cpx–Tr–Atg. However, because in this way the bulk rock Mg/(Mg+Fe) is fixed and magnetite assumed to be non-reactive, the model underestimates the Fe content of olivine at high temperature and modelled temperatures of dehydration reactions may be slightly overestimated (Bretscher, Hermann, & Pettke, 2018). Ti-clinohumite was not included because an F-rich end-member is not available, leading to an overestimation of the amount of olivine in the calculations.

To explore the effect of electrolytic fluids on carbon solubility – as opposed to simple binary H$_2$O–CO$_2$ fluids used in classic thermodynamic approaches for impure marbles and meta-ophicarbonate rocks (e.g. Connolly & Trommsdorff, 1991; Trommsdorff & Evans, 1977) – we calculated the speciation of carbon-bearing solutes in equilibrium with meta-ophicarbonate rocks using the 'lagged speciation' algorithm of Perple_X 6.8.5 (Connolly & Galvez, 2018). This iterative Gibbs free energy minimization algorithm allows accounting for electrolytic fluid chemistry using the extension of the Helgeson–Kirkham–Flowers formulation (Helgeson, Kirkham, & Flowers, 1981) to high pressures by the Deep Earth Water (DEW) model (Sverjensky, Harrison, & Azzolini, 2014), while considering overall equilibrium between rock, solvent and solute species (Connolly & Galvez, 2018; Galvez, Manning, Connolly, & Rumble, 2015). In contrast to the DEW model, non-ideal molecular solution models are used to treat neutral carbonic volatiles as solvent species (COH-Fluid), because predictions of their concentration as solute species in a pure H$_2$O solvent become unreliable at high concentrations (Galvez et al., 2015, 2016). In the computation, the fluid speciation, ionic strength and pH are derived from the chemical potentials defined by the phase stabilities, concentrations and partial molar Gibbs free energies of solvent and solids, using charge-balance and the Davies extension of the Debye–Hueckel equation to compute activity coefficients for electrolytes (Galvez et al., 2015, 2016). The solution consistent with the solute-free initial condition is iteratively refined until chemical potentials converge to

conform to mass-balance between solid, solvent and solute (Connolly & Galvez, 2018). More details on the computation method are available in Connolly and Galvez (2018), and Galvez et al. (2015).

To be consistent with the classical models with binary $X_{CO_2}$ fluids, we used the implementation of aqueous species thermochemical data of the DEW model (Sverjensky et al., 2014; May 2017 version) in the thermodynamic database of Holland and Powell (1998; version 2002), the same mineral solid solution models as described previously (Appendix S1) and the CORK equation of state for $H_2O$ and $CO_2$. For $CH_4$, we employed the modified Redlich–Kwong equation of state, even though calculations showed that reduced carbon species are negligible in fluids in equilibrium with carbonate-rich rocks. The use of different hybrid solvent equations of state results in only slight differences in speciation and solubility for the conditions of interest of this study. Minor differences between carbon solubilities predicted by binary $X_{CO_2}$ models and those from electrolytic fluids are further due to different fluid mixing models. Redox conditions in the speciation calculation were fixed by using a bulk oxygen content corresponding to the respective metal oxides, all carbon as $CO_2$ and $Fe^{3+}/Fe_{total}$ fixed to 0.57, providing a redox budget similar to that of natural serpentinites (Debret et al., 2015) and meta-ophicarbonates (Table 2). Because no Na- or K-bearing solid phases occur in the Milagrosa serpentinites, Atg–Di–Dol rocks and marble lenses or in the Almirez meta-ophicarbonates (Table 1) and concentrations of both elements are on the threshold of detection limits (Table 2), we restricted the calculations to the Fe–Ca–Mg–Al–Si–C–H–O system. Highly fluid mobile elements such as Cl were also neglected because antigorite breakdown fluids have a relatively low salinity (Scambelluri et al., 2004) and accounting for them would require externally constrained chemical potentials (Galvez et al., 2016). As a result, our calculations slightly underestimate carbon solubility, because the models do not consider potentially C-bearing complexes—such as $NaHCO_3$ (Facq et al., 2016)—that form in the presence of Na, K or Cl (Facq et al., 2016; Galvez et al., 2016).

# 5 | RESULTS

## 5.1 | Bulk rock chemistry

The major bulk rock composition of the Milagrosa marbles, Atg–Di–Dol rocks and serpentinites and the Almirez meta-ophicarbonates and host Chl-harzburgites are given in Table 2. In the CaO–MgO–SiO₂ ternary, the bulk compositions of Milagrosa and Almirez carbonate lenses plot along the calcite–antigorite join, mostly due to highly variable CaO and $CO_2$ contents at nearly constant Mg/Si ratio (Figure 8a). In this ternary, the Milagrosa serpentinites and

the Almirez Chl-harzburgite hosting the carbonate lenses have similar or lower Mg/Si ratios and have variable Ca/Si ratios plotting away from antigorite towards enstatite, tremolite and diopside (Figure 8b). Milagrosa serpentinite has bulk compositions similar to Almirez serpentinite (Garrido et al., 2005 ; Marchesi, Garrido, Padrón-Navarta, López Sánchez-Vizcaíno, & Gomez-Pugnaire, 2013) and to abyssal peridotite, but are slightly richer in CaO, $Al_2O_3$ and $SiO_2$ (Figure 8b; Table 2).

Milagrosa TiCl-Cal marbles have the lowest $SiO_2$ and MgO and the highest CaO contents among the investigated samples (Figure 8a). Associated Di–Dol marbles have higher $SiO_2$ contents and lower CaO/MgO ratios, plotting close to the intersection of the antigorite–calcite and dolomite–diopside joins (Figure 8a). The Milagrosa Atg–Di–Dol rocks are richer in $SiO_2$ and MgO while poorer in CaO and $CO_2$, remarkably similar to the Almirez meta-ophicarbonates (Figure 8a).

Major variations in CaO, MgO and $SiO_2$ contents of the carbonate-bearing lithologies in both localities correlate with variable bulk rock $CO_2$ content, as illustrated by the inverse linear correlation between $CO_2$ and $SiO_2$ (Figure 8c). The $Al_2O_3$ and total $Fe_2O_3$ contents decrease with increasing CaO and $CO_2$ and range from the relatively high $Al_2O_3$ (2.8–3.5 wt%) and $Fe_2O_3$ (7.5–9.1 wt%) in the host serpentinites and Chl-harzburgite to very low $Al_2O_3$ (0.5–0.7 wt%) and $Fe_2O_3$ (0.6–1.1 wt%) of the Milagrosa TiCl–Cal marble lenses (Table 2). Milagrosa Atg–Di–Dol rocks and Almirez meta-ophicarbonates have intermediate $Al_2O_3$ (1.9–2.3 wt%) and $Fe_2O_3$ (4.0–6.2 wt%) contents.

The $Na_2O$ and $K_2O$ contents of carbonate lenses are close to or below the detection limits of XRF analyses, as in the host serpentinites and Chl-harzburgites (Table 2). The Almirez meta-ophicarbonate lenses are highly enriched in Ni and Cr (>2,000 ppm), approaching contents typical of mantle peridotites and similar to those of the host Chl-harzburgite (Figure 8d). The Milagrosa Atg–Di–Dol rocks and Di–Dol marbles show a lesser, but significant, enrichment in Ni and Cr, which decreases with increasing carbonate content (Figure 8c,d). These bulk chemical characteristics distinguish the Milagrosa and Almirez serpentinite-hosted carbonate rocks (marble lenses, Atg–Di–Dol rocks and meta-ophicarbonates) from other widespread carbonate rocks of the NFC Mulhacén unit. These carbonate rocks that are not hosted in serpentinites or Chl-harzburgite have markedly different bulk MgO/SiO₂ ratios (grey and dashed fields in Figure 8a), and Ni and Cr contents below detection limit of XRF analysis (Table 2). Likewise, the calcite to dolomite ratio in the carbonate fraction of the Almirez and Milagrosa carbonate lenses mostly ranges between 0.6 and 1.4 (except for TiCl-Cal marbles), independently of the bulk rock $CO_2$-content and metamorphic grade (Figure 8e). In contrast, the carbonate fraction in NFC Dol-marbles
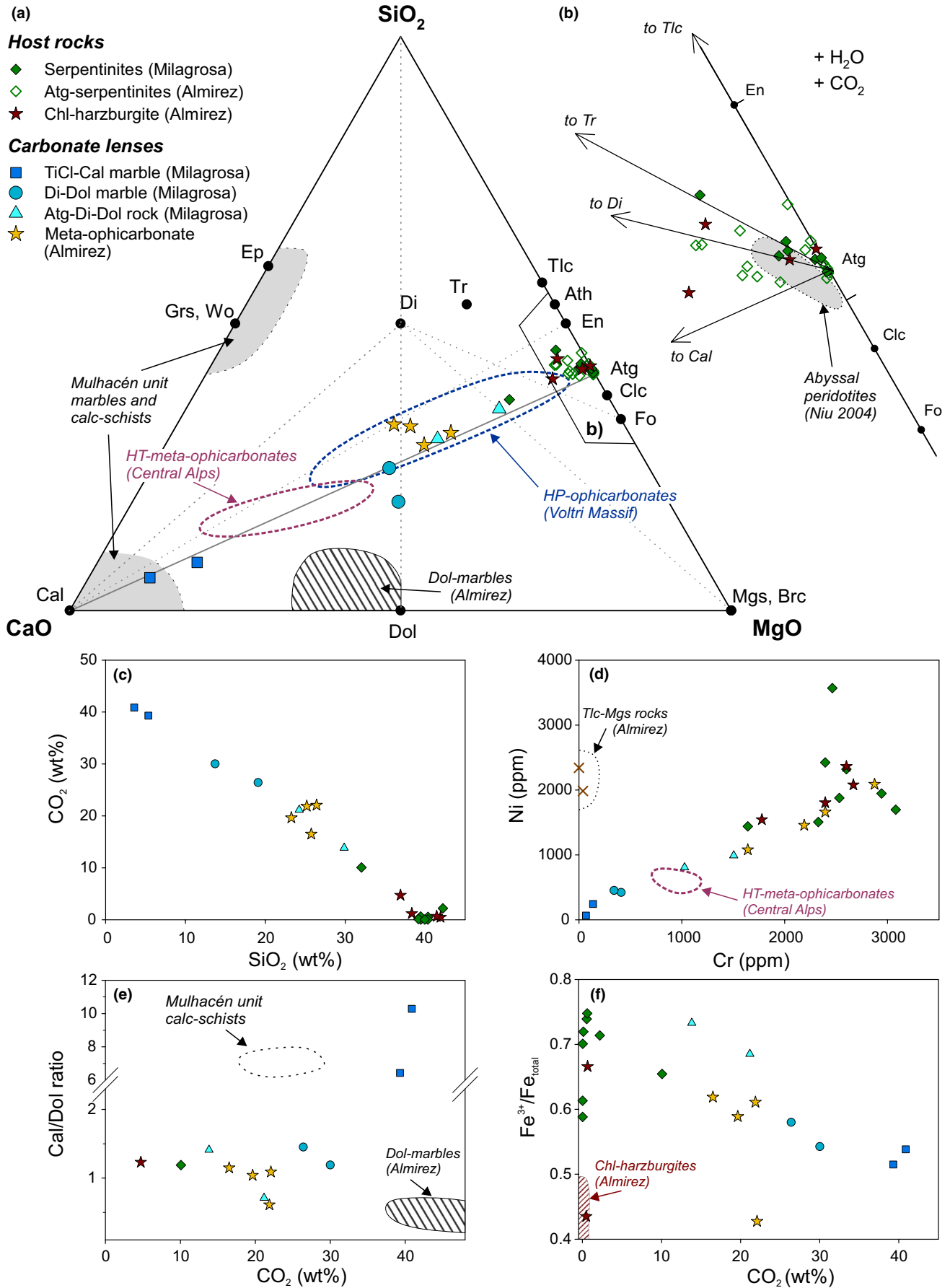
**(a)**

*Host rocks*
- ◆ Serpentinites (Milagrosa)
- ◇ Atg-serpentinites (Almirez)
- ★ Chl-harzburgite (Almirez)

*Carbonate lenses*
- ■ TiCl-Cal marble (Milagrosa)
- ● Di-Dol marble (Milagrosa)
- ▲ Atg-Di-Dol rock (Milagrosa)
- ★ Meta-ophicarbonate (Almirez)

**FIGURE 8** Bulk rock compositional variations of carbonate lenses and host peridotites from Milagrosa and Almirez. (a) CaO–MgO–SiO$_2$ (CMS) ternary compositional diagram with molar whole rock proportions and projected mineral end-members for comparison. Typical meta-sedimentary carbonate rocks fall within the field to the left of the dolomite–diopside join. Fields for compositions of other meta-ophicarbonates shown as a reference (Voltri Massif: Scambelluri et al., 2016; Central Alps: Stucki, 2001; Figure 1). See text for further discussion. (b) Detail from the Ca-poor part of the CMS-diagram in (a). Data of Almirez Atg-serpentinites (hollow symbols) are from Garrido et al. (2005 ), Alt et al. (2012) and Marchesi et al. (2013). (c) Total carbon given as CO$_2$ versus whole rock SiO$_2$. (d) Ni and Cr whole rock contents. (e) Calcite–dolomite weight ratio (as obtained from analysis by Chittick apparatus) of carbonate-rich lithologies plotted against CO$_2$-content. (f) Molar ferric/total iron ratio against CO$_2$-content; field of Almirez Chl-harzburgites after Marchesi et al. (2013)

and calc-schists is either dominated by dolomite or calcite (Figure 8e; Table 2).

The bulk rock Fe$^{3+}$/Fe$_{total}$ ratio decreases with increasing CO$_2$-contents, from 0.59 to 0.75 in Milagrosa serpentinites to 0.52–0.54 in the TiCl-Cal marble lenses (Figure 8f; Table 2). Milagrosa Atg–Di–Dol rocks have bulk rock Fe$^{3+}$/Fe$_{total}$ ratios similar to some of their host serpentinites (Figure 8f) and higher than the Almirez meta-ophicarbonate of equivalent major element composition. These differences may be due to the incorporation of Fe$^{3+}$ in antigorite in the lower metamorphic grade Milagrosa serpentinites and Atg–Di–Dol rocks, while in the Almirez antigorite-absent meta-ophicarbonate ferric iron is mostly partitioned into magnetite. The lower bulk Fe$^{3+}$/Fe$_{total}$ of meta-ophicarbonate lenses within prograde Almirez Chl-harzburgites relative to the serpentinite-hosted Milagrosa Atg–Di–Dol rocks (Figure 8f) is in accordance with the decrease in bulk Fe$^{3+}$/Fe$_{total}$ from Atg-serpentinite to Chl-harzburgite described elsewhere in Almirez (Debret et al., 2015; their Figure 4). However, the Almirez meta-ophicarbonates have generally higher bulk Fe$^{3+}$/Fe$_{total}$ (~0.6) than the host Chl-harzburgite (0.4–0.5; Figure 8f).

## 5.2 | Mineral chemistry

Representative compositions and structural formulae of all minerals are listed in Tables S1–S5.

### 5.2.1 | Carbonates

In the Milagrosa marble lenses, calcite in the matrix shows a large variation in $X_{MgCO_3}$ [$X_{MgCO_3}$ = Mg/(Mg+Ca+Fe)] from nearly pure CaCO$_3$ to Mg-calcite with $X_{MgCO_3}$ = 0.047 (Figure 5a and Figure S2). Tr-bearing Di–Dol marbles contain calcite with generally lower $X_{MgCO_3}$ values (0.005–0.038) than the TiCl-Cal-marbles, but in both cases there is a relatively large variability of Mg-contents within single samples; often with sharp compositional contrasts between neighbouring calcite grains (Figure 5a). The highest Mg-contents in Mg-calcite are present in inclusions within Ti-clinohumite and diopside ($X_{MgCO_3}$ = 0.024–0.072). Such Mg-calcite inclusions can be used to estimate minimum peak temperatures for the formation of the host mineral phases (Ferry, 2001; Mizuochi, Satish-Kumar, Motoyoshi, & Michibayashi,

2010). Using the Fe-free formulation of the calcite-dolomite solvus thermometer by Anovitz and Essene (1987), calcite inclusions with the highest Mg-contents within Ti-clinohumite and diopside from the Milagrosa marble lenses (five measurements) yield temperatures of 515–600°C (Table S1). In matrix calcite, reintegration of vermicular dolomite exsolutions (using microprobe analysis with a widened beam and image analysis to estimate the fraction of exsolved dolomite; Figure 5a) gives $X_{MgCO_3}$ values of 0.049–0.055, corresponding to 520–550°C. Calcite in all Milagrosa lithologies mostly has very low Fe-contents ($X_{FeCO_3}$ < 0.005). Dolomite has similar low Fe-contents in TiCl-Cal-marbles and is significantly Fe-richer in Di–Dol marbles and Atg–Di–Dol rocks ($X_{FeCO_3}$ = 0.009–0.150).

Calcite in Almirez meta-ophicarbonates shows similarly variable $X_{MgCO_3}$ values (Figure S2). The highest measured Mg-content ($X_{MgCO_3}$ = 0.096) in a Mg-calcite inclusion within a Ti-clinohumite porphyroblast yields a minimum peak temperature of ~660°C. Matrix calcite in equilibrium with dolomite has substantially lower $X_{MgCO_3}$ (0.017–0.052; corresponding to 310–580°C) than Mg-calcite inclusions. Aragonite inclusions in olivine, diopside and Ti-clinohumite have $X_{MgCO_3}$-values close to or below the detection limit and negligible Fe-contents (Table S1). Unlike Mg-calcite, dolomite has relatively homogeneous compositions ($X_{CaCO_3}$ = 0.503–0.513). Dolomite in the Almirez meta-ophicarbonates is not zoned, unlike dolomite in HP/UHP carbonate rocks elsewhere (e.g. Ferrando et al., 2017; Li, Klemd, Gao, & Meyer, 2014). In the Mgs-Tlc level, dolomite has a very restricted compositional range ($X_{CaCO_3}$ = 0.496–0.501) and magnesite is rich in iron (3.5–4.0 wt%). Scarce dolomite and magnesite in Chl-harzburgites close to the carbonate lenses have compositions very similar to those in the Mgs-Tlc level. Dolomite in meta-ophicarbonate clasts enclosed in carbonate breccia (Tr–Di–Dol rocks) is enriched in Fe and has lower $X_{CaCO_3}$ (0.498–0.508) than in the meta-ophicarbonate lens.

### 5.2.2 | Olivine

Olivine in Almirez meta-ophicarbonate has a forsterite content of $X_{Mg}$ = 0.93–0.95 [$X_{Mg}$ = Mg/(Mg-Fe)] (Figure 9a), significantly higher than olivine in the host Chl-harzburgites and in Cpx-serpentinites at Almirez ($X_{Mg}$ = 0.89–0.91 and
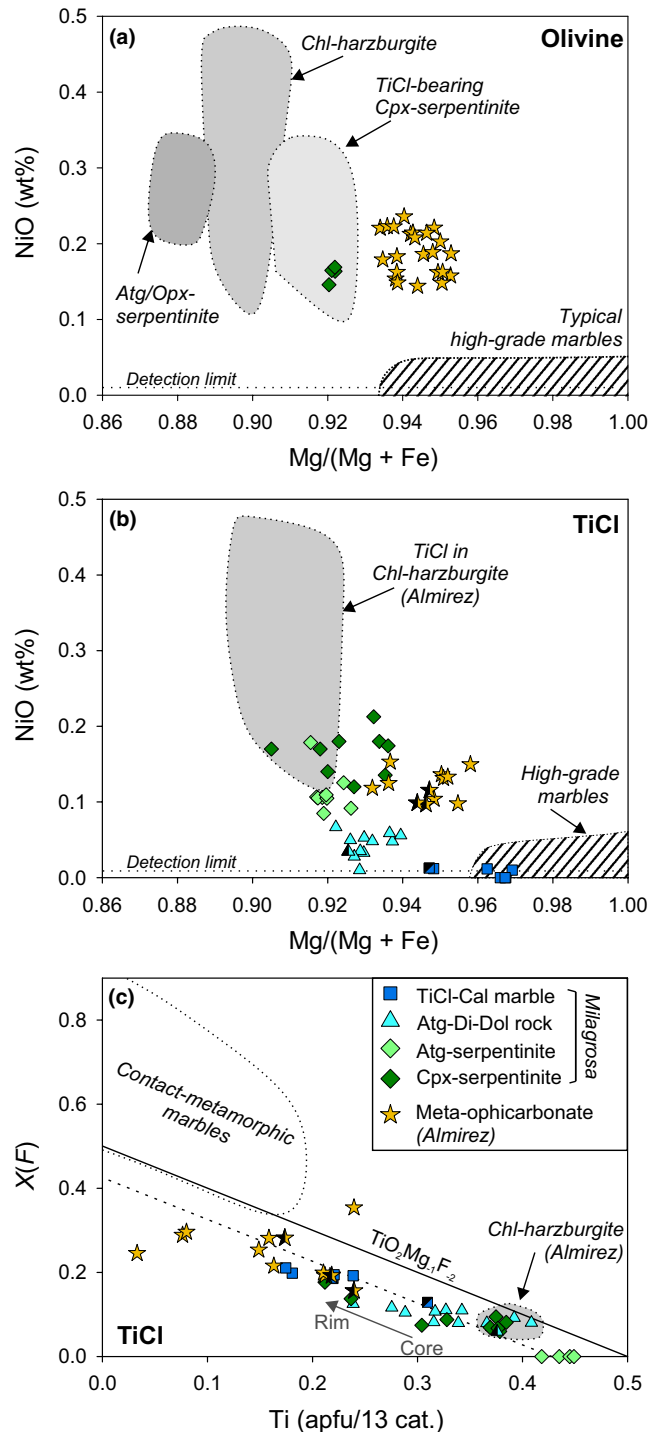
**FIGURE 9** Composition of olivine (a) and Ti-clinohumite (b and c) in carbonate lenses and host peridotites at Milagrosa and Almirez (common legend in Figure 9c); in comparison with olivine and Ti-clinohumite from Almirez Chl-harzburgites and serpentinites (grey fields; López Sánchez-Vizcaíno et al., 2005; Padrón-Navarta et al., 2011) and contact metamorphic high-grade marbles of the western Betics (Mazzoli et al., 2013 ). $X(F) = F$ (atoms per 13 cations)/2. Half-black symbols in b and c show coexisting Ti-chondrodite compositions (normalized to seven cations)
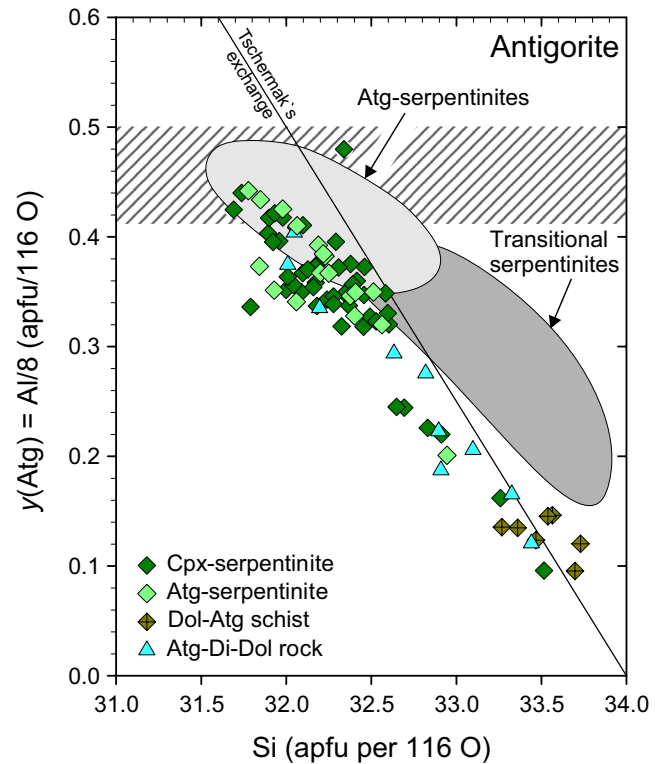


**FIGURE 10** Antigorite compositions in Milagrosa serpentinites and Atg–Di–Dol-rocks in comparison to Almirez serpentinites and transitional rocks (grey fields; after Padrón-Navarta et al., 2011) in a $y(Atg) =$ total Al/8 versus Si plot (calculated on the basis of 116 O, assuming a polysome m = 17). The line represents an ideal Tschermak's exchange, with the maximum solubility of Al in Atg indicated by the horizontal band (Padrón-Navarta et al., 2013)

0.91–0.93, respectively; Padrón-Navarta et al., 2011) and is not zoned. Notably, olivine in the meta-ophicarbonate has high NiO (0.12–0.24 wt%) and relatively high MnO contents (0.25–0.36 wt%; Table S2), which is comparable to olivine compositions in Atg-serpentinite and Cpx-serpentinite at Almirez (Padrón-Navarta et al., 2011). In contrast, olivine in high grade or contact-metamorphic marbles has typically very low NiO (normally below detection limit) and contains less iron (e.g. Mazzoli et al., 2013 ; Mizuochi et al., 2010). Rare olivine in Cpx-serpentinites at Milagrosa has compositions similar to those of Cpx-serpentinites at Almirez (about Fo$_{92}$, with relatively low NiO contents; Figure 9a).

## 5.2.3 | Ti-clinohumite and TiChn

Divalent cation contents (Mg, Fe, Mn, Ni) in Ti-clinohumite in Almirez meta-ophicarbonate are very similar to those of coexisting olivine ($X_{Mg}$ = 0.93–0.96 and slightly lower NiO values; Figure 9b; Table S2). This agrees with the nearly equal partitioning of divalent cations between olivine and
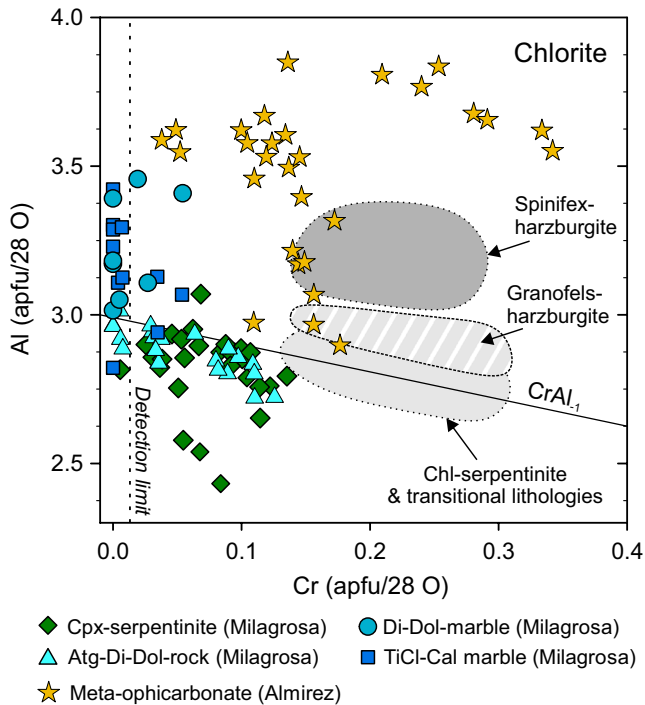
**FIGURE 11** Al versus Cr compositions of chlorite in Milagrosa carbonate lenses and host serpentinites and in Almirez meta-ophicarbonate. The grey fields show the range of chlorite compositions in the Almirez serpentinites and Chl-harzburgite (from Padrón-Navarta et al., 2011); the line represents the $CrAl_{-1}$ exchange vector

Ti-clinohumite reported by López Sánchez-Vizcaíno et al. (2005) for Atg-serpentinites and Chl-harzburgites at Almirez. Ti-clinohumite and olivine in the meta-ophicarbonate lenses contain less Fe than those in the host Chl-harzburgites (Figure 10a,b), in accordance with the lower Fe contents of the bulk rock. This is also the case at Milagrosa: while Ti-clinohumite contains only little Fe and no NiO in TiCl-Cal-marbles, the content of these two elements in Ti-clinohumite increases to $X_{Mg}$ = 0.92–0.94 and up to 0.07 wt% NiO in Atg–Di–Dol rock and to $X_{Mg}$ = 0.91–0.93 and up to 0.20 wt% NiO in host serpentinites (Figure 9b).

TiCl-Cal marbles lenses at Milagrosa contain Ti-clinohumite with $X_{Ti}$ = 0.17–0.24 ($X_{Ti}$ = Ti atoms per 13 cations) and $X_F$ = 0.18–0.21 ($X_F$ = F/2; Figure 9c). In contrast, Ti-clinohumite is fluorine-free and nearly saturated in Ti in Atg-serpentinites (5.1–5.5 wt% $TiO_2$, $X_{Ti}$ = 0.42–0.47), similar to that in the Almirez Atg-serpentinites (López Sánchez-Vizcaíno et al., 2005). Ti-clinohumite in Milagrosa Cpx-serpentinite and Atg–Di–Dol rock has intermediate compositions between the two extremes, with $X_{Ti}$ = 0.28–0.39 and $X_F$ = 0.07–0.10 in cores and rim compositions of $X_{Ti}$ = 0.2 and $X_F$ = 0.18 (Figure 9c). These values are somewhat similar to Ti-clinohumite compositions in Chl-harzburgites at Almirez (López Sánchez-Vizcaíno et al., 2005), but with a more pronounced variability along

the $TiO_2Mg_{-1}F_{-2}$ exchange vector. Ti-clinohumite in the Almirez meta-ophicarbonate lenses is clearly distinct from Ti-clinohumite reported by López Sánchez-Vizcaíno et al. (2005) and Padrón-Navarta et al. (2011) for the host Chl-harzburgites, showing high fluorine contents (Figure 9c). High-$T$ metamorphic Ti-clinohumite in sedimentary marbles—as, for example, from the western Betic Cordillera, Spain (Mazzoli et al., 2013 ) or from the Bergell contact aureole (Gieré, 1987)—tend to have even higher fluorine contents, which often exceed the 1:1 $TiO_2Mg_{-1}F_{-2}$ exchange that is limited by the maximum Ti-content in TiCl of $X_{Ti}$ = 0.5 (Figure 9c).

Ti-chondrodite is preserved occasionally in the cores of Ti-clinohumite porphyroblasts in Milagrosa carbonate lenses and Almirez meta-ophicarbonate. Compared to Ti-clinohumite, TiChn is generally richer in $TiO_2$ (~3–4 wt% higher than coexisting Ti-clinohumite) and has lower $X_F$, with similar NiO contents and $X_{Mg}$ values (half-black symbols in Figure 9b,c; Table S2).

## 5.2.4 | Clinopyroxene

Clinopyroxene in the carbonate rock lenses from Milgrosa and Almirez is almost pure diopside ($X_{Mg}$ = 0.97–0.99). $Al_2O_3$-contents of diopside are low in both cases, but they are slightly higher in the Almirez meta-ophicarbonates (~0.05–0.09 wt%) than in the marble lenses and Atg–Di–Dol rocks at Milagrosa (<0.03 wt%). In the Milagrosa Cpx-serpentinites, relict primary clinopyroxene is partially preserved, with 0.8–1.4 wt% $Al_2O_3$, ~0.4 wt% $Cr_2O_3$, 0.25–0.48 wt% $Na_2O$ and 0.2–0.5 wt% $TiO_2$, but most clinopyroxene is also relatively pure diopside (with $X_{Mg}$ = 0.96–0.98; Table S3).

## 5.2.5 | Antigorite

Antigorite in the Milagrosa serpentinites is generally rich in $Al_2O_3$ (up to 4 wt%), rather poor in Fe [Mg/(Mg+FeO$_{total}$) = 0.95–0.97], $Cr_2O_3$ (up to 0.4 wt%) and NiO (<0.35 wt%; Table S4) and diverges from the ideal Tschermak's exchange vector towards lower Al and Si values (Figure 10). No major compositional differences exist between antigorite in Cpx-serpentinite and Atg-serpentinite. In a plot of Si versus $y_{Atg}$ = Al/8 (Padrón-Navarta et al., 2013; Figure 10), most of the analyses cluster close to the maximum solubility of Al in antigorite. In contrast to the very high Al-contents of Atg in the Milagrosa serpentinites, Atg–Di–Dol rocks contain antigorite with $y_{Atg}$ = 0.1–0.4. The lower $y_{Atg}$ values correspond to mineral assemblages dominated by Di–Dol–Chl with only minor antigorite, while the higher $y_{Atg}$ values characterize rocks in which antigorite is more abundant than chlorite. Antigorite in Dol-Atg-schists situated

~6 m apart from the Milagrosa marble lenses has distinctly lower $y_{Atg}$ (~0.13).

## 5.2.6 | Chlorite

Chlorite in host peridotites and carbonate rock lenses at both Milagrosa and Almirez is dominantly penninite with high $X_{Mg}$ (0.94–0.98). $Al_2O_3$-contents are relatively low (12–16 wt%; 2.8–3.8 Al atoms per formula unit per 28 O; Table S4). Chlorite in Cpx-serpentinites from Milagrosa shows minor deviation from an ideal Tschermak's exchange due to the substitution of up to 0.14 apfu Cr for Al (Figure 11). The same trend of chlorite compositions along the $CrAl_{-1}$ exchange is typical for peridotites and has been reported for Chl-serpentinites and transitional lithologies at Almirez (Padrón-Navarta et al., 2011). The Cr content in chlorite from Milagrosa TiCl-Cal-marble and Di–Dol-marble lenses is below or close to the detection limit, whereas Atg–Di–Dol rocks contain chlorite with Cr-contents resembling those of the host serpentinites. Chlorite in the Almirez meta-ophicarbonate lenses has elevated contents of Al (3.0–3.9 apfu) and Cr (up to 0.35 apfu). The trend towards higher Al-contents in these rocks is comparable to that of chlorite formed during Atg-breakdown in spinifex-harzburgites at Almirez (grey fields in Figure 11), but with a higher Tschermak's exchange.

## 5.2.7 | Other phases

Scarce tremolite in Milagrosa Cpx-serpentinites and retrograde tremolite in carbonate lenses are very close to the pure end-member, with $X_{Mg} = 0.97–0.99$, Na and Al < 0.15 wt% (Table S3). Notably, magnetite in the Almirez meta-ophicarbonates is enriched in $Cr_2O_3$ (3–6 wt%), MgO (1.5–2.5 wt%), MnO and NiO (both ~0.3–0.6 wt%; Table S5). Magnetite in Milagrosa Atg–Di–Dol rocks and Di–Dol marble shows a similar, but less pronounced enrichment in Cr, Mg, Mn and Ni. Associated ilmenite has high MgO and MnO contents (up to 9.1 and 4.5 wt%, respectively).

## 5.3 | *P–T–t* constraints

### 5.3.1 | Milagrosa serpentinite and marble lenses

Calcite–dolomite thermometry in Milagrosa serpentinite-hosted marble lenses yields peak metamorphic temperatures in the range of ~550–600°C (cf. Section 5.2.1). Although metamorphic olivine is abundant in typical serpentinite at this temperature range (Bucher & Grapes, 2011), olivine is mostly absent in Milagrosa serpentinites due to their relatively low Mg/Si and high $Fe^{3+}/Fe_{tot}$ bulk rock ratios (Figure 8). In the *P–T* pseudosection of Cpx-serpentinite—obtained
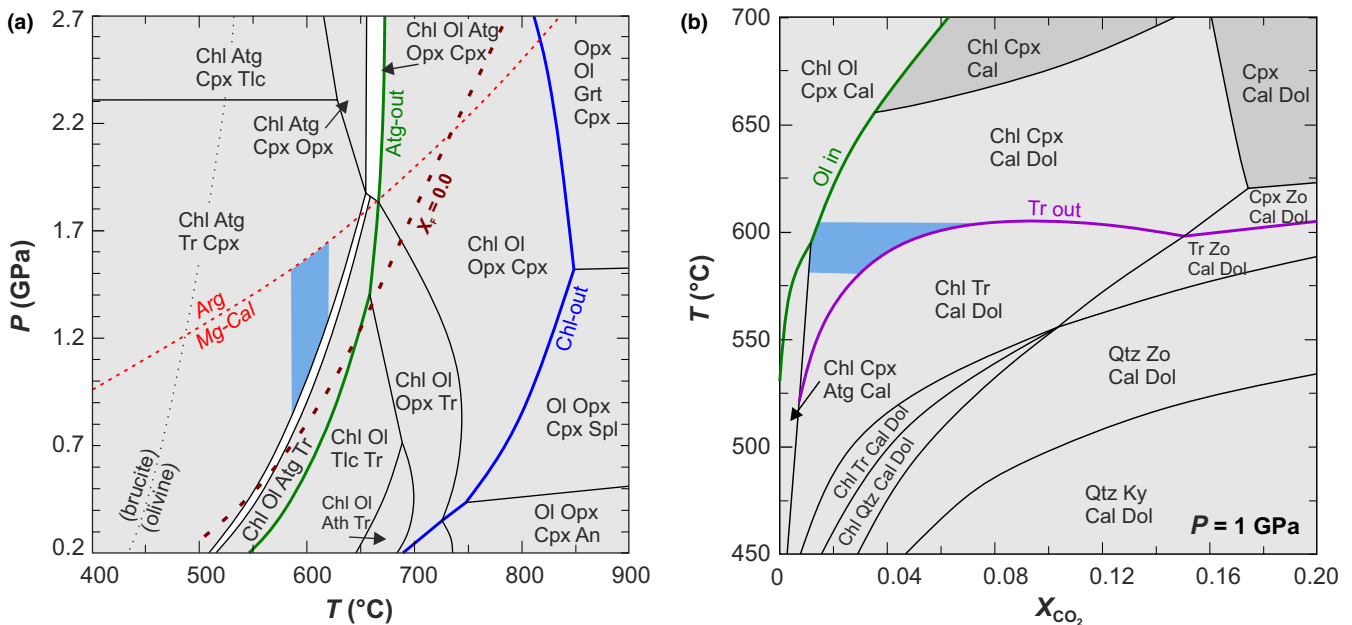


**FIGURE 12** *P–T* constraints for Milagrosa Cpx-serpentinite (a) and TiCl-Cal marble (b). (a) *P–T* section computed from bulk composition SN-90 using a reduced model FeO content (Table 2; Section 4.4). The blue box area represents the estimated field of peak metamorphism when assuming that no aragonite was present. The TiCl-breakdown curve (brown dashed line) at $X_F = 0.0$ for F-free, Ti-saturated Ti-clinohumite in serpentinite is taken from experiments by Weiss (1997). All fields contain a $H_2O$-fluid phase. (b) Fluid-saturated, isobaric $T–X_{CO_2}$ pseudosection of Milagrosa TiCl-Cal-marble (SN-10). The range of temperature and $X_{CO_2}$ conditions estimated for peak metamorphism is shown in blue
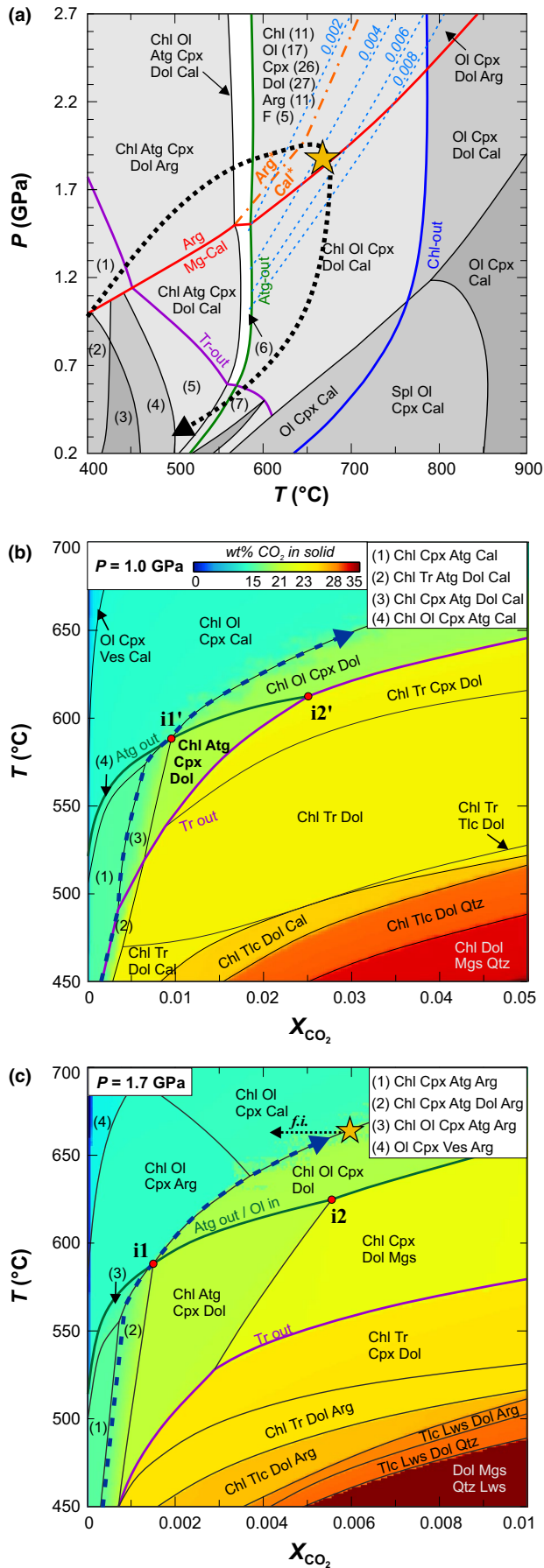
**FIGURE 13** $P$–$T$–$X_{CO_2}$ constraints of meta-ophicarbonate. (a) $P$–$T$ pseudosection of Almirez meta-ophicarbonate (SN-138; Table 2). Calculated mineral modes (wt%; including fluid F) are given in brackets at the peak conditions (yellow star) according to the Almirez $P$–$T$ path (black dotted arrow, after Laborda-López et al., 2018). All fields contain fluid, with $X_{CO_2}$ shown as blue dashed lines. The aragonite–calcite transition is shown as predicted by the model (red solid line) and as determined experimentally by Hermann et al. (2016) in a carbonate-pure system (orange stippled line). Assemblages in numbered fields: (1) Chl Atg Tr Dol arag, (2) Atg Tr Dol Cal, (3) Atg Tr Cal, (4) Chl Atg Tr Cal, (5) Chl Atg Tr Cpx Cal, (6) Chl Ol Atg Cpx Dol Cal, (7) Chl Ol Tr Dol Cal. (b and c) Isobaric fluid-saturated $T$-$X_{CO_2}$ pseudosections at 1.0 and 1.7 GPa for the same rock composition as in (a), superposed on the solid rock $CO_2$ content (common colour scale in (b)). Coexisting aragonite/calcite and dolomite indicate a rock-buffered fluid evolution path as shown by the blue dashed arrows. Black dotted arrow (f.i.): expected evolution if pervasive fluid-infiltration decarbonation during host serpentinite dehydration occurs

after subtracting the bulk rock ferric iron in magnetite (cf. Section 4.4)— the observed assemblage Chl–Atg–Tr–Cpx in Milagrosa Cpx-serpentinite is stable in a large divariant field (Figure 12a). The absence of serpentinite with Chl–Ol–Atg–Tr and Chl–Atg–Cpx–Opx assemblages constrains the equilibrium temperature to <550–650°C, depending on the equilibration pressure (Figure 12a). At ~600°C—as obtained from carbonate thermometry in the marble lenses—olivine would form at <0.9 GPa, providing a minimum pressure estimate for the assemblage Chl–Atg–Tr–Cpx (Figure 12a). The equilibration of Milagrosa serpentinite at >0.8 GPa and <650°C is further supported by the lack of petrographic evidence of breakdown of F-free, Ti-saturated Ti-clinohumite to olivine+ilmenite (brown dashed line in Figure 12a), which is observed in higher temperature Atg-serpentinite from the Almirez massif (López Sánchez-Vizcaíno et al., 2005, 2009).

The minimum temperatures of 550–600°C estimated by calcite–dolomite thermometry of Mg-calcite inclusions in Ti-clinohumite from the marble lenses (cf. Section 5.2.1; Figure 5a) are consistent with pseudosection constraints of marble lenses and Atg–Di–Dol rocks (Figure 12b). In the fluid-saturated isobaric $T$–$X_{CO_2}$ pseudosection of the TiCl-Cal marble (Figure 12b), the absence of tremolite or antigorite at 1 GPa in the peak assemblage Chl–Cpx–Cal–Dol constrains equilibration temperature >525°C at $0.01 > X_{CO_2} > 0.08$. Although F and Ti stabilize Ti-clinohumite and TiChn at high temperature (Engi & Lindsley, 1980; Evans & Trommsdorff, 1983; Grützner, Klemme, Rohrbach, Gervasoni, & Berndt, 2017; López Sánchez-Vizcaíno et al., 2005), no suitable solid solution models exist to model phase relations of Ti-clinohumite and TiChn in fluorine- and titanium-bearing carbonate systems (Weiss, 1997). In the computed pseudo-section of Figure 12b (F- and Ti-free system) these phases

are metastable but their topologies are likely similar to that of olivine (Franz & Ackermand, 1980; Rice, 1980).

Figure 13a shows the *P–T* pseudosection for Almirez meta-ophicarbonates. This pseudosection is also appropriate to illustrate the phase relations of Milagrosa Atg–Di–Dol rocks due to their similar bulk composition (cf. Section 5.1; Figure 8; Table 2). The isobaric prograde evolution for this bulk composition as a function of $X_{CO_2}$ is illustrated in *T*–$X_{CO_2}$ pseudosections at 1.0 and 1.7 GPa (Figure 13b,c). In Milagrosa Atg–Di–Dol rocks, the common assemblage Atg–Chl–Cpx–Dol (±Cal, without Tr) provides a minimum *P–T* range of stability of >0.6 GPa at 550°C (Tr-out line in Figure 13a) and 1.0 GPa at 580°C (Figure 13b; Connolly & Trommsdorff, 1991; their Figures 9b and 10b). These minimum *P–T* estimates are consistent with those derived from Milagrosa serpentinite and marble lenses (Figure 12). The absence of olivine in Milagrosa Atg–Di–Dol rocks constrains their maximum equilibration temperature to <615°C (at 1.0 GPa) (Figure 13b). At higher temperature, antigorite reacts out to form olivine, regardless of the fluid $X_{CO_2}$ (Figure 13b). For this bulk composition, upper conditions for the stability of antigorite are 615°C and $X_{CO_2} < 0.025$ at 1.0 GPa (point i2' in Figure 13b) or 625°C and $X_{CO_2} < 0.006$ at 1.7 GPa (point i2 in Figure 13c). In the range of equilibration temperature (550–600°C) of Milagrosa serpentinites and marble lenses, the absence of aragonite bounds their equilibration pressure to <1.4–1.5 GPa (aragonite-in reaction in Figure 13a). Due to the fast kinetics of the aragonite–calcite phase transition, we cannot exclude, however, that aragonite was present at peak pressure but broke down to Mg-calcite during exhumation. The *P–T* conditions (1.0–1.4 GPa; 550–600°C) estimated for the Milagrosa carbonate–silicate rocks are within the range of peak metamorphic conditions inferred for marbles, calc-schists and amphibolite and garnet-mica schists of the eastern part of the NFC, but are lower than the peak conditions recorded in eclogites and metaevaporites (Booth-Rea et al., 2015; Gómez-Pugnaire et al., 1994; Gómez-Pugnaire et al., in press; López Sánchez-Vizcaíno et al., 1997).

### 5.3.2 | Almirez meta-ophicarbonate lenses

Experimental work, phase modelling and petrological constraints indicate that dehydration of Atg-serpentinite to Chl-harzburgite in Almirez occurred at ~660°C and 1.8–1.9 GPa (Figure 13a; yellow star on the *P–T–t* path; López Sánchez-Vizcaíno et al., 2009; Padrón-Navarta, Hermann, et al., 2010). Thermodynamic phase modelling reveals that the Almirez meta-ophicarbonates reached similar *P–T* peak conditions as their host Chl-harzburgite (Figure 13a,c). The assemblage Chl–Ol–Cpx–Dol–Arg of Almirez meta-ophicarbonate requires equilibration at *T* > 580°C and *P* > 1.6 GPa (Figure 13c). These minimum equilibration conditions are

consistent with the absence of antigorite (Figure 13a,c; temperature beyond the Atg-out condition) and the coexistence of aragonite in equilibrium with diopside and olivine (Figures 7g,h and 13a, solid red and stippled orange lines). The composition of calcite inclusions ($X_{CaCO_3} = 0.897$) in olivine and Ti-clinohumite is similar to that of Mg-calcite formed after aragonite breakdown as experimentally determined at 650–670°C and 1.8–2 GPa (Hermann, Troitzsch, & Scott, 2016). The phase proportions predicted by thermodynamic modelling at these *P–T* conditions are in good agreement with the observed modal proportions (yellow star in Figure 13a). These data indicate that Almirez meta-ophicarbonate was stable in the Chl-harzburgite facies beyond the conditions of antigorite dehydration (Figure 13a). For peak temperatures in the range of 670–680°C (Figure 13a; *P–T–t* path after Laborda-López et al., 2018), the assemblage Chl–Ol–Cpx–Dol–Cal limits the composition of the fluid to $0.004 < X_{CO_2} < 0.007$ (yellow star in Figure 13a,c). Calcite–dolomite thermometry of matrix carbonate yields *T* < 550°C, which records retrograde re-equilibration conditions (Table S1), a common feature of high-grade metamorphic carbonate rocks (Ferry, 2001; Mizuochi et al., 2010).

## 6 | DISCUSSION

### 6.1 | Origin of the protoliths of NFC serpentinite-hosted carbonate–silicate rocks

Meta-serpentinites from the NFC record a history of Jurassic seafloor alteration (Alt et al., 2012; Laborda-López et al., 2018; Puga et al., 2011) possibly in an ocean-continent transition setting (the S–SE Iberian palaeo-margin) and narrow oceanic basin, similar to that proposed for the origin of their Alps and Apennines counterparts (Lagabrielle, Vitale Brovarone, & Ildefonse, 2015). In the middle Miocene, subduction of the Iberian margin beneath the extended Alborán continental domain caused HP metamorphism of the NFC (cf. Section 2; Figure 2c). In the investigated NFC ultramafic massifs, carbonates occur in the Milagrosa TiCl–Cal and Di–Dol marbles and Atg–Di–Dol rocks, all of them hosted in serpentinite (Figure 8a), while in the Almirez massif they occur as meta-ophicarbonate lenses hosted in Chl-harzburgite; hereafter, we will refer to all these lithologies as (meta-) serpentinite-hosted carbonate–silicate rocks. These NFC lithologies may have formed—and modified—during the Jurassic oceanic stage of development of the passive margin, and the ensuing Miocene subduction of this basin and its continental margin (Figure 14).

Ophicarbonates and related carbonate–silicate rocks with variable bulk major element compositions—notably $SiO_2$, CaO and MgO—may form in oceanic and subduction settings (Figure 14), by leaching of alkali earth elements from silicate minerals and precipitation of carbonate upon
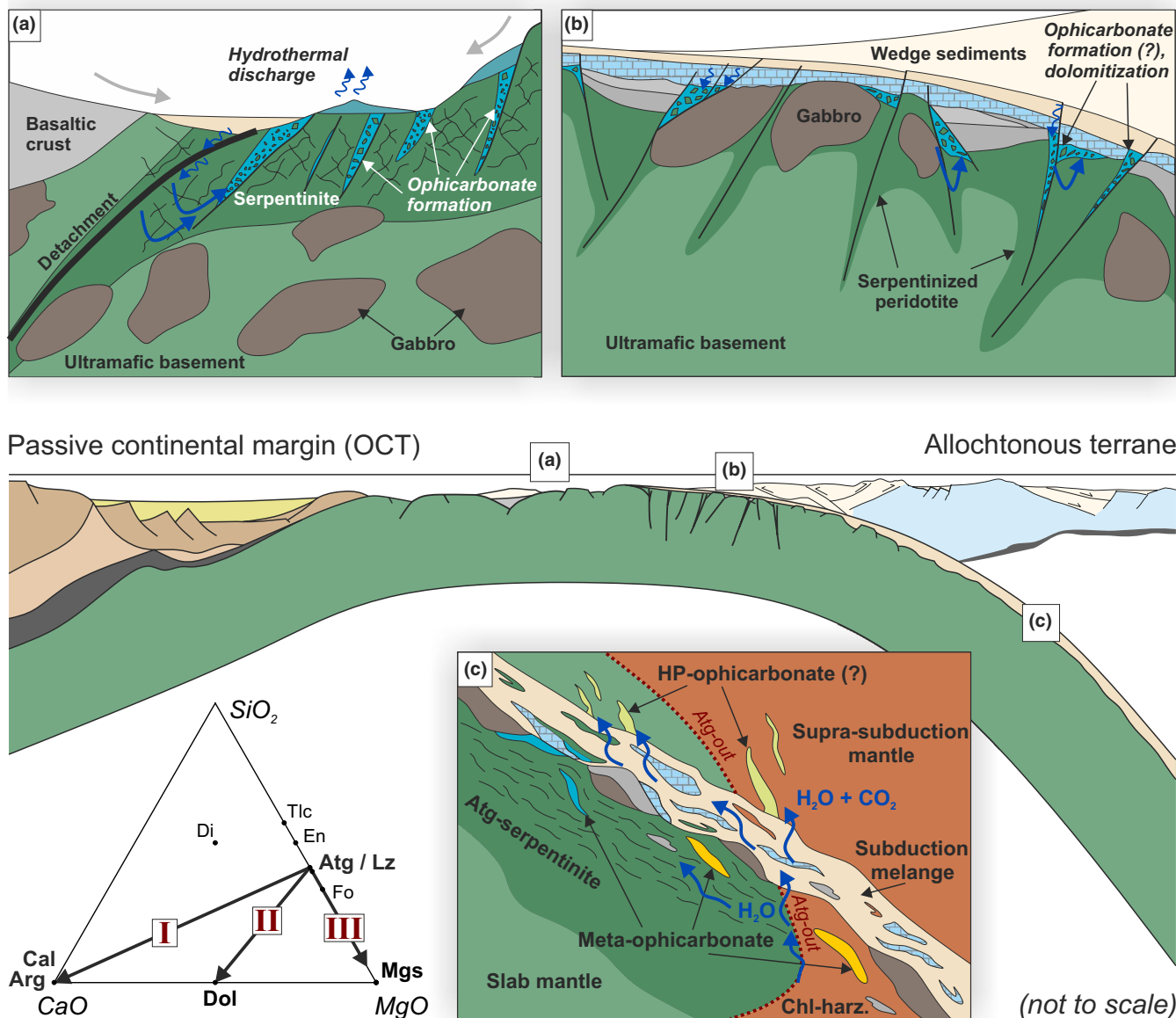
**FIGURE 14** Conceptual sketch of settings in which ophicarbonates may form. (a) Oceanic stage, sub-seafloor serpentinite-hosted hydrothermal systems in slow spreading crust (modified after Lafay et al., 2017). (b) By fluid interaction between marine sediments and serpentinite along bend faults in the outer rise of subduction. (c) During subduction by interaction of fluids derived from devolatilization reactions (e.g. Atg-out) with serpentinite or Chl-harzburgite in the slab, along the plate interface or in the supra-subduction mantle (light green lenses). Blue and yellow lenses illustrate Atg-bearing and partially dehydrated slab meta-ophicarbonates, respectively. The CaO–MgO–SiO$_2$ ternary shows bulk chemical trends corresponding to the formation of ophicalcite (I), ophidolomite (II) and ophimagnesite (III)

mixing with dissolved inorganic carbon. In slow spreading mid-ocean ridges (Figure 14a), serpentinite-hosted carbonate–silicate rocks occur in the stockwork of submarine low-$T$ hydrothermal fields (Lafay et al., 2017; Ludwig, Kelley, Butterfield, Nelson, & Früh-Green, 2006; Schwarzenbach, Früh-Green, Bernasconi, Alt, & Plas, 2013), in detachment faults of oceanic core complexes (Bach et al., 2011; Picazo, Manatschal, Cannat, & Andréani, 2013; Schroeder et al., 2015) and in transform faults (Alt et al., 2018; Bonatti,

Lawrence, Hamlyn, & Breger, 1980). In these settings, carbonates are heterogeneously distributed at different scales in veins, replacing serpentine mesh textures and as matrix cement of tectonic or sedimentary serpentinite breccias (Figure 14a; Bonatti et al., 1980; Grozeva, Klein, Seewald, & Sylva, 2017; Klein et al., 2015; Lafay et al., 2017; Picazo et al., 2013; Schroeder et al., 2015). Infiltration of seawater into deeply rooted faults in intermediate- to fast-spreading oceanic crust and faults formed during bending of the slab in

the outer rise of subduction zones (Ranero, Phipps Morgan, McIntosh, & Reichert, 2003) might also result in serpentinization and carbonation of sub-crustal peridotite (Figure 14b). Serpentinite-hosted ophicalcites are symptomatic of seawater carbonation because the relatively low $a\mathrm{CO_{2,aq}}$ and Mg/Ca ratio of seawater and serpentinization fluids—in comparison to metamorphic fluids—promote crystallization of calcite and aragonite instead of Mg-carbonates (Bonatti et al., 1980; Eickmann, Bach, Rosner, & Peckmann, 2009; Grozeva et al., 2017; Schroeder et al., 2015; Schwarzenbach et al., 2013).

In subduction zones, serpentinite-hosted carbonate–silicate rocks may also form in the subducting slab, the slab interface and in the overlying mantle wedge (Figure 14c). Metamorphic devolatilization reactions of altered oceanic crust and sediments in the slab generate C- and Mg/Ca-rich fluids (Caciagli & Manning, 2003; Facq et al., 2014; Tiraboschi et al., 2017). At different arc depths, reaction of these fluids with slab and mantle wedge serpentinites may produce ophimagnesite (magnesite–antigorite rocks), talc–magnesite rocks and listvenites (Falk & Kelemen, 2015; Menzel et al., 2018; Sieber, Hermann, & Yaxley, 2018), HP-ophicarbonate (e.g. Scambelluri et al., 2016) and carbonate–enstatite rocks (Tumiati et al., 2013). Tectonic mixing and prograde metamorphism of serpentinite and carbonate-bearing sediments in the slab interface may also generate hybrid rocks with a bulk composition similar to that of ophicarbonates (Scambelluri et al., 2016).

In the $\mathrm{SiO_2}$–MgO–CaO ternary, the bulk compositions of the Milagrosa and Almirez (meta-)serpentinite-hosted carbonate–silicate rocks plot along the calcite–antigorite join (Figure 8a–c), indicating that their bulk compositions can be accounted for by mixtures of ophicalcite (calcite±aragonite) and serpentinite-group minerals (Figure 14). High-*T* (700–750°C, 0.6 GPa; Figure 1) meta-ophicarbonates from the central Alps (Stucki, 2001) and Voltri Massif (Ligurian Alps) serpentinite-hosted HP ophicarbonates (>500°C, 2.0–2.5 GPa; Figure 1) composed of garnet-dolomite marbles and hybrid rocks (Scambelluri et al., 2016), also plot along this join (Figure 8a). Most ophicalcites in ophiolites from the Alps, Apennines and Pyrenees are thought to have formed during their oceanic evolution due to seawater interaction with serpentinite (Figure 14a; Clerc, Boulvais, Lagabrielle, & de Saint Blanquat, 2014; Collins et al., 2015; Lafay et al., 2017; Pozzorini & Früh-Green, 1996; Schwarzenbach et al., 2013).

Subduction metamorphism and deformation have obliterated the primary textures of Milagrosa and Almirez serpentinite-hosted carbonate-bearing rocks, preventing any inference from their primary structure. However, variable mixtures of serpentinite and ophicalcite account well for the bulk compositional trend of Milagrosa and Almirez carbonate rocks along the $\mathrm{CaCO_3}$–Serpentine-group mineral join (Figure 14; trend I), suggesting that their protoliths formed

during the Jurassic oceanic stage. The elevated Ni and Cr bulk rock contents (Figure 8d), enrichment of Ni in Ti-clinohumite (Figure 9b) and Cr in chlorite (Figure 11) and the trace occurrence of pyrrhotite, pentlandite, ilmenite/perovskite and Cr-bearing magnetite (Table 1; Figure S1), are in agreement with the formation of Milagrosa TiCl-Cal-marbles and Di–Dol marbles by prograde metamorphism of a carbonated serpentinite protolith. Milagrosa TiCl-Cal-marbles (Figure 4) might then have formed after ophicarbonates precipitated in high-permeability zones and Atg–Di–Dol rocks (Figure 4) in domains of lower fluid flux or after carbonate-bearing veins and breccias in adjacent serpentinites. Alternatively, the protoliths of the Milagrosa marble lenses may have originated from mixtures of marine carbonates and serpentinite detritus (Figure 14a). Tectonic mixing, dissolution of marble carbonates and coeval Ca-metasomatism of host serpentinites during HP metamorphism may account for the current tectonic fabric and mineral assemblages of Milagrosa Atg–Di–Dol rocks and Di–Dol-marbles.

Like in the Milagrosa serpentinite-hosted carbonate rocks, the high bulk rock Cr and Ni contents (Figure 8e) and Ti-clinohumite and olivine composition (Figure 9) of Almirez meta-ophicarbonate demonstrate that diopside, olivine and Ti-clinohumite derived from prograde metamorphism of a carbonate–serpentinite protolith. In the $\mathrm{SiO_2}$–CaO–MgO ternary, Almirez meta-ophicarbonate lenses plot at a relatively high MgO/CaO ratio along the calcite–antigorite tie-line (Figure 8a), implying higher contents of serpentinite-group mineral in their bulk composition than in the Milagrosa TiCl-Cal marble lenses. Precipitation or replacement of serpentine minerals by calcite and aragonite in an ellipsoid-shaped vein network or ophicarbonate breccia zone in oceanic fault zones might account well for the Almirez protolith.

The calcite–antigorite trend of NFC serpentinite-hosted carbonate–silicate rocks indicates the limited role of open-system precipitation or mechanical mixing of dolomite and magnesite in the genesis of their protoliths. Binary mixtures of these carbonate minerals with serpentinite plot along the dolomite–antigorite (Figure 14; Trend II) and magnesite–antigorite joins (Figure 14; Trend III). Serpentinite-hosted dolomite (ophidolomite) and magnesite (i.e. ophimagnesite, talc-magnesite rocks and listvenite) assemblages require higher $a\mathrm{CO_{2,aq}}$ and Mg/Ca ratios than those of seawater hydrothermal systems (cf. figure 6b of Grozeva et al., 2017) and, consequently, are uncommon in seafloor serpentinites (Eickmann, Bach, & Peckmann, 2009; Grozeva et al., 2017) and ophiolite-related ophicarbonates (Lafay et al., 2017). Interaction of Mg- and C-bearing fluids equilibrated with serpentine-bearing sediments may favour the precipitation of dolomite (Figure 14b; Trend II), which might occur, for instance, during reactivation of normal faults in the outer rise of the incoming oceanic slab (Figure 14b). Open-system formation of dolomite

and magnesite is also preponderant in the forearc—associated to listvenites (Menzel et al., 2018)—and during HP precipitation of magnesite veins (ophimagnesite; Tumiati et al., 2013; Figure 14c; Trend III). Milagrosa and Almirez late carbonate-tremolite veins and Tlc-Mgs rocks (Table 1; Figures 3b and 6e) may record such open-system HP precipitation of dolomite and magnesite, but their conditions of formation are beyond the scope of the present study.

## 6.2 | Metamorphic evolution

### 6.2.1 | Phase relationships and devolatilization reactions

To illustrate the phase relations during subduction metamorphism of hybrid compositions with variable serpentinite and meta-ophicarbonate fractions, such as those encountered in

Milagrosa and Almirez (Section 6.1; Figure 8a), we calculated a $T$–$X_{Serp}$ pseudosection covering the compositional variation between pure $CaCO_3$ and natural serpentinite (Figure 15a), where $X_{Serp}$ corresponds to the weight fraction of serpentinite in the binary mixing with $CaCO_3$. The $T$–$X$ pseudosection is computed for eclogite facies (1.7 GPa; Figure 15a) relevant for the metamorphic conditions at Almirez, but is applicable to lower pressures because phase assemblages in meta-ophicarbonates do not change much with pressure (Figure 13a). Also shown are the changes in modal mineral abundances with temperature for different bulk compositions (Figure 15b–d), which illustrate the different prograde reactions provided in Table 3.

At blueschist facies conditions (450–550°C), an assemblage composed of antigorite and aragonite, with minor clinopyroxene, dolomite and chlorite, is predicted for most compositions (Figure 15a). The formation of olivine after
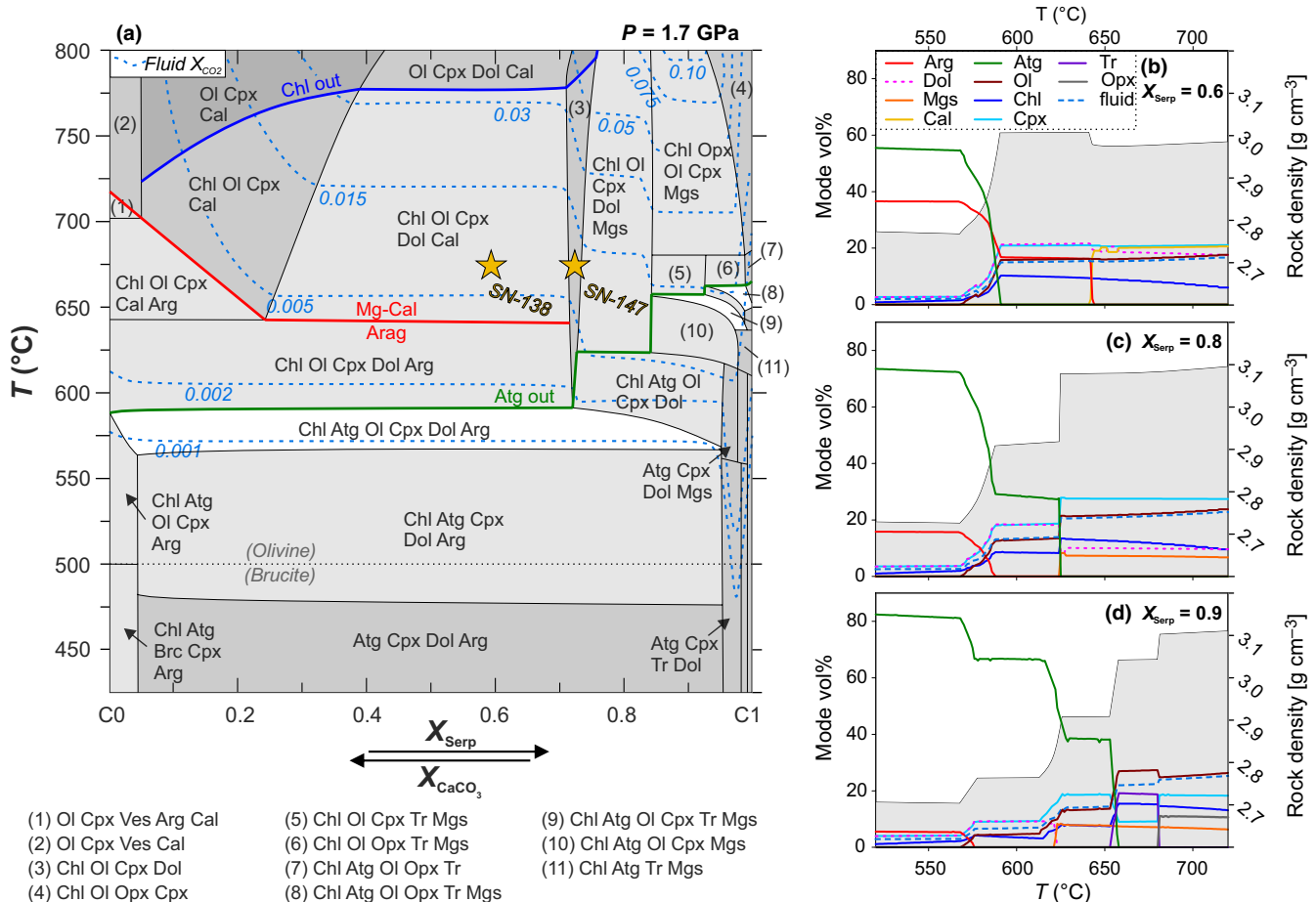


**FIGURE 15** (a) Isobaric $T$–$X$ pseudosection for the compositional variation between pure $CaCO_3$ (C0) and serpentinite (C1); and (b–d) evolution of the modal phase abundance (including fluid) and solid rock density (grey shaded background and axis on the right) with temperature at three representative $X_{Serp}$ showing different devolatilization behaviour at 1.7 GPa ($X_{Serp}$ = fraction of serpentinite composition C1; see text for discussion). For the model serpentinite composition C1, the Fe-content of the bulk chemical composition of serpentinite sample SN-109 (Table 2) was modified by subtracting 2.0 wt% $Fe_2O_3$ to account for $Fe^{3+}$ in antigorite and 4.1 wt% magnetite, resulting in a model C1 FeO content of 1.47 wt% (cf. Section 4.4). If less $Fe_2O_3$ is subtracted, the brucite/olivine stability fields at $T$ < 570°C expand to compositions with higher $X_{Serp}$ at the expense of dolomite (grey dotted line). The blue dashed lines in (a) show fluid $X_{CO2}$ in equilibrium with the mineral assemblage. Yellow stars: compositions and peak metamorphic conditions of Almirez meta-ophicarbonates

| Reaction numbers | Reaction |
|---|---|
| (1) | $Atg + 6\,CaCO_3 = 6\,Di + 18\,Fo + 0.5\,Chl + 6\,CO_2 + 27\,H_2O$ |
| (2) | $Atg + 42\,CaCO_3 + 12\,CO_2 = 15\,Di + 27\,Dol + 0.5\,Chl + 27\,H_2O$ |
| (1+2) [a] | $Atg + 17.92\,CaCO_3 = 8.98\,Di + 12.04\,Fo + 8.94\,Dol + 0.5\,Chl + 27\,H_2O + 0.04\,CO_2$ |
| (3) | $Atg + 4.5\,Dol = 4.5\,Di + 21\,Fo + 0.5\,Chl + 9\,CO_2 + 27\,H_2O$ |
| (4) | $Atg + 15\,Dol + 27\,CO_2 = 15\,Di + 42\,Mgs + 0.5\,Chl + 27\,H_2O$ |
| (3+4) [b] | $Atg + 8.93\,Dol = 8.93\,Di + 12.14\,Fo + 0.5\,Chl + 17.72\,Mgs + 27\,H_2O + 0.14\,CO_2$ |
| (5) | $Di + 3\,Dol = 2\,Fo + 4\,CaCO_3 + 2\,CO_2$ |
| (6) | $Di + 4\,Mgs = 2\,Fo + Dol + 2\,CO_2$ |

**TABLE 3** Key prograde reactions in meta-ophicarbonates in the CaO–MgO–$Al_2O_3$–$SiO_2$–$H_2O$–$CO_2$ system, using simplified compositions of Atg [$Mg_{47}Al_2Si_{33}O_{85}(OH)_{62}$], Chl [$Mg_{10}Al_4Si_6O_{20}(OH)_{16}$] and Dol [$CaMg(CO_3)_2$]. Depending on $P$–$T$, $CaCO_3$ may be calcite or aragonite

[a]Balanced overall reaction, for $X_{CO_2} = 0.0015$ at 580°C, 1.7 GPa (point i1 in Figure 13c). [b]Balanced overall reaction, for $X_{CO_2} = 0.0052$ at 620°C, 1.7 GPa.

brucite ($T > 500$°C and $X_{Serp} < 0.05$ in Figure 15a) depends on the bulk rock $(Mg+Fe^{2+})/Si$; this reaction would also occur for compositions near the serpentinite end-member (grey dotted line in Figure 15a) for bulk $Fe^{3+}/Fe^{2+}$ lower than those considered in our calculation (see Section 4.4).

The first major prograde devolatilization event occurs at 570–590°C with the reaction of antigorite with $CaCO_3$ to diopside, chlorite and olivine (Reaction 1 in Table 3). The $CO_2$ released in this reaction may be buffered by Reaction 2 (Table 3) decreasing the $X_{CO_2}$ of the fluid (~0.0014 at 1.7 GPa) by forming additional dolomite (Table 3; this reaction step corresponds to pseudo-invariant point i1 in Figure 13b,c). For bulk compositions with $X_{Serp} < 0.72$ (>28 wt% $CaCO_3$ in the precursor ophicarbonate) at $T > 590$°C, antigorite is consumed by Reaction 1+2 (Table 3) resulting in a partially dehydrated Chl–Ol–Cpx–Dol–$CaCO_3$ assemblage similar to that of Almirez meta-ophicarbonate (Figure 15a,b).

For bulk compositions with $X_{Serp} > 0.72$ (Figure 15a), antigorite is still present after reaction with $CaCO_3$ (Figure 15c,d; see also additional $T$-$X_{CO_2}$ pseudosections in Figure S3). At 625°C, this antigorite reacts with dolomite (mostly produced by Reaction 2) to form diopside, olivine and chlorite (Reaction 3 in Table 3; Figure 15c). The formation of magnesite according to Reaction 4 (Table 3) buffers the fluid $X_{CO_2}$ to 0.005 (at 1.7 GPa; blue dotted lines in Figure 15a). The overall reaction (Reaction 3+4 in Table 3; Figure 15c) of antigorite with dolomite to diopside, olivine, chlorite and magnesite—corresponding to pseudo-invariant points i2 in Figure 13c and Figure S3—produces the high-grade assemblage Chl–Ol–Cpx–Dol–Mgs (Figure 15a). At lower pressure (e.g. 1 GPa), the reaction product is tremolite instead of diopside (e.g. Trommsdorff & Evans, 1977) and the fluid is buffered to higher $X_{CO_2}$ (pseudo-invariant points i2' in Figure 13b and Figure S3).

For $X_{Serp} > 0.84$ (Figure 15a), three dehydration reaction steps involving antigorite occur, consuming $CaCO_3$ by Reactions 1 and 2 at 570–590°C and dolomite by Reactions 3 and 4 at 615–625°C (Figure 15d). Excess antigorite breaks down at 650–660°C to olivine, orthopyroxene and

chlorite, producing the assemblage Chl–Opx–Ol–Cpx–Mgs (Figure 15a,d). At $P < 1.8$ GPa, tremolite may form at the expense of diopside in an intermediate reaction step (fields 5 and 6 in Figure 15a; Figure 15d). With continued heating ($T > 620$°C), reactions of diopside with dolomite (for $X_{Serp}$ <0.75) or magnesite (for $0.72 < X_{Serp} < 0.84$; Figure 15a) to olivine+carbonate release $CO_2$, increasing the fluid $X_{CO_2}$ (Reactions 5 and 6 in Table 3; blue dotted arrow in Figure 13c). Chlorite eventually breaks down to Al-bearing clinopyroxene and olivine (Figures 13a and 15a), producing lower fluid amounts compared to the breakdown of antigorite. Like antigorite, chlorite breakdown occurs at lower temperatures in $CaCO_3$-richer compositions (~780°C for $X_{Serp} < 0.75$; Figure 15a) than in pure serpentinite (>820°C; Figure 12a).

## 6.2.2 | Role of infiltration-driven devolatilization

As long as the fluid composition is rock-buffered (Ferrando et al., 2017; Kerrick & Connolly, 1998), the prograde devolatilization reactions in meta-ophicarbonate do not lead to substantial decarbonation during subduction because the $X_{CO_2}$ isopleths are essentially parallel to subduction $P$–$T$ paths (Figures 1 and 13a). However, fluids derived from devolatilization and dissolution reactions of different subducting lithologies (Bebout & Penniston-Dorland, 2016; Figure 14c) can lead to open-system carbonation or removal of carbon. Subduction metamorphic terranes show evidence of infiltration-driven devolatilization and carbon release caused by channelized fluid flushing (Ague & Nicolescu, 2014; Angiboust, Pettke, De Hoog, Caron, & Oncken, 2014; Vitale Brovarone et al., 2018). Carbonate re-deposited in veins in lower grade subduction lithologies further provides indirect evidence of high carbon mobility in subduction fluids (e.g. Piccoli, Vitale Brovarone, & Ague, 2018). In serpentinite-hosted carbonate–silicate rocks, infiltration of $H_2O$-rich fluids at isobaric and isothermal conditions (e.g. Figure 13c, black dotted arrow labelled f.i.) induces decarbonation

through Reactions 5 or 6 (Table 3). On the other hand, in-filtration of $CO_2$-rich fluids stabilizes dolomite and magnesite over Ca-carbonate (fields with Chl–Atg–Cpx–Dol, Chl–Ol–Cpx–Dol and Chl–Cpx–Dol–Mgs assemblages in Figure 13c). During prograde subduction metamorphism of serpentinite, fluids are released by the breakdown of brucite and antigorite. Infiltration of $H_2O$-rich fluids—causing isothermal, infiltration-driven devolatilization reactions—was probable in the serpentinite-hosted carbonate–silicate rocks at Milagrosa and Almirez, because their peak metamorphic temperatures exceed the stability conditions of brucite and antigorite respectively (Sections 5.3.1 and 5.3.2).

The mineral assemblages and compositions of Milagrosa Atg–Di–Dol rocks and marble lenses are consistent with their formation by incipient reaction of antigorite with carbonate (Reaction 1+2 in Table 3). The absence of antigorite in TiCl-Cal marble, along with the predominance of dolomite and lack of olivine in Atg–Di–Dol rock (Table 1), indicates that the $X_{CO_2}$ of fluid at peak metamorphic conditions (Figure 12b; and Chl–Atg–Cpx–Dol field in Figure 13b) was higher than that predicted for an internally buffered fluid evolution path of a calcite-antigorite protolith (blue dashed arrow in Figure 13b). This could be explained by dolomitization of the antigorite–calcite protolith prior to peak metamorphism or by infiltration of $CO_2$-bearing fluids during subduction metamorphism. Thus, the observed phase-relations of the Milagrosa carbonate–silicate rocks do not show a clear record of $H_2O$-rich fluid infiltration.

In the Almirez meta-ophicarbonates several observations indicate that during prograde dehydration and decarbonation reactions the fluid composition was buffered by the rock, following a fluid evolution similar to that shown in Figure 13c (blue dashed arrow). The abundance of aragonite, dolomite and chlorite inclusions in olivine and diopside (Figure 7g–h) indicates that these two minerals formed by Reactions 1 and 2 (Table 3). This implies that the fluid evolved along a path that passed through the pseudo-invariant point i1 in Figure 13c. The composition of chlorite, olivine and Ti-clinohumite shows that they formed by reaction of Ni- and Cr-bearing antigorite with carbonate. Dolomite and $CaCO_3$ (mainly calcite)—with well-equilibrated polygonal grain boundaries—are abundant in most samples (Figure 7c,d; Table 2), showing that the fluid $X_{CO_2}$ evolved along the pseudo-univariant line defined by the Chl–Ol–Cpx–Dol–Arg assemblage (Figure 13c). If the fluid composition was controlled externally and the time-integrated fluid flux large, $CaCO_3$ (external fluid with $X_{CO_2} > 0.005$) or dolomite (if $X_{CO_2} < 0.005$ at 650°C) would have become unstable (Reaction 5 in Table 3). Dolomite is the main carbonate phase in gneissic-textured meta-ophicarbonate (Figures 6d and 7b; sample SN-136) and in one granofelsic sample (Figure 7e; sample SN-147), which may point to infiltration-driven open-system reactions (Reaction 5 or 6, Table 3). The observed assemblage

chlorite-diopside-dolomite-Ti-clinohumite (with minor or rare olivine and Ca-carbonate) in the gneissic meta-ophicarbonate intercalations may point to infiltration of $CO_2$-bearing fluids and a related depletion in sulphur in these domains (Sample SN-136 in Table 2), but the timing of this event in relation to the metamorphic evolution is unclear. In the case of the granofelsic, dolomite-rich meta-ophicarbonate (Figure 7e; sample SN-147), aragonite inclusions are abundant while magnesite is absent, suggesting that the dolomite-rich assemblage was controlled by the protolith composition (close to $X_{Serp} = 0.73$; field 3 in Figure 15a) and not by $H_2O$-rich fluid infiltration. Zonation in carbonates indicative of dissolution and re-precipitation by fluids observed in subduction-related carbonate rocks elsewhere (Ferrando et al., 2017) are not present in the Almirez meta-ophicarbonates. All these observations point to a limited role of open system fluid-driven decarbonation in Milagrosa and Almirez serpentinite-hosted meta-ophicarbonates.

## 6.2.3 | Equilibrium fluid composition and speciation: implications for carbon mobility

During prograde subduction, metamorphism of serpentinite-hosted meta-ophicarbonates of variable composition (Figure 15b–d) may produce differing $X_{CO_2}$ fluid composition (blue dashed isopleths in Figure 15a). At the same temperature, the $X_{CO_2}$ of fluid in equilibrium with bulk compositions with low $CaCO_3$ content is higher than for $CaCO_3$-rich compositions (Figure 15a). For instance, at 660°C and 1.7 GPa, $X_{CO_2}$ of fluids is ~0.006 for $X_{Serp} < 0.72$, 0.011 for $X_{Serp}$ 0.72–0.84, and ~0.015 for $X_{Serp}$ 0.84–0.98 (see also Figure S3). During prograde subduction metamorphism and devolatilization, the variable fluid $X_{CO_2}$ in serpentinite-hosted ophicarbonates with variable effective bulk compositions may lead to dissolution and/or precipitation at different length scales (Figures 4 and 7a–e). Therefore, serpentinite-hosted ophicarbonates with low bulk $CaCO_3$ content ($X_{Serp} > 0.72$)—e.g. marginal veined ophicalcite zones—would release more carbon into dehydration fluids than carbonate-rich domains ($X_{Serp} < 0.72$; Figure 15a). At 720°C, for a bulk composition with $X_{Serp}$ of 0.98 (~0.88 wt% $CO_2$), all carbon is dissolved in the fluid phase (field 4 in Figure 15a), while for a bulk rock composition similar to that of the Almirez meta-ophicarbonate lenses fluids would only contain ~0.2 wt% $CO_2$. On the other hand, devolatilization fluids produced by dolomite-consuming Reactions 3 and 4 (Table 2) in bulk rocks with $X_{Serp} > 0.72$ may precipitate carbonate if they infiltrate into meta-ophicarbonate with $X_{Serp} < 0.72$ because the fluid would be buffered to lower $X_{CO_2}$ (Figure 15a and Figure S3).

Previous studies have shown that accounting for electrolytic fluids in thermodynamic models increases the solubility of carbon in subduction fluids by a factor of ~2 relative to
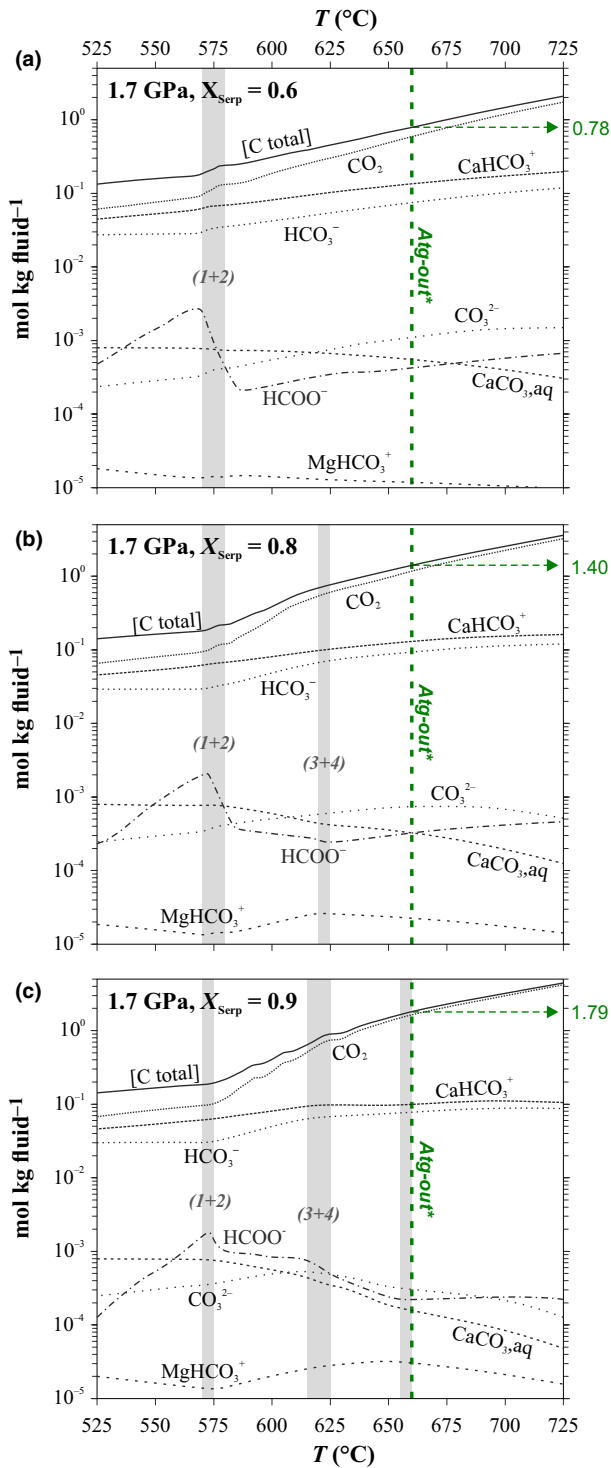
**FIGURE 16** Predicted carbon speciation and solubility (C total) in fluid in equilibrium with different meta-ophicarbonate compositions ($X_{Serp}$ = 0.6, 0.8, and 0.9) at 1.7 GPa. Grey fields show temperature ranges of prograde devolatilization reactions (see Table 3; Figure 15). The green dashed line illustrates conditions of Atg-breakdown in host serpentinite and total carbon solubility (mol/kg fluid) at this temperature. Calculated using lagged speciation mode for electrolytic fluids in Perple_X 6.8.5 (cf. Section 4.4)
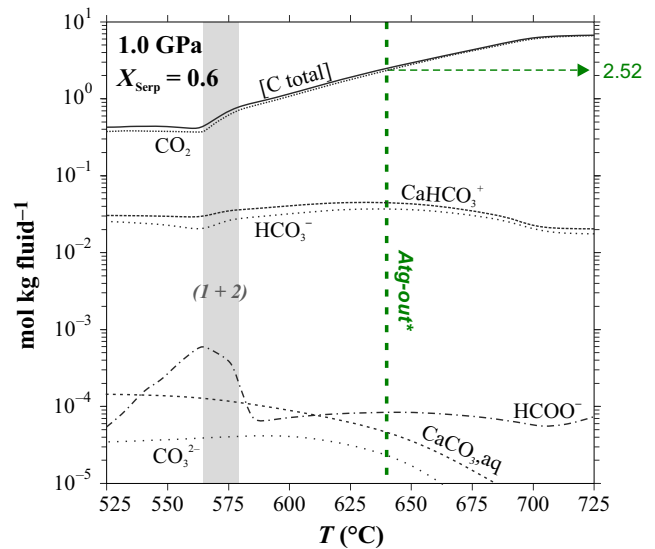


**FIGURE 17** Predicted carbon speciation and solubility (C total) in fluid in equilibrium with meta-ophicarbonate ($X_{Serp}$ = 0.6) at 1.0 GPa. Grey fields show temperature ranges of prograde devolatilization reactions and the green dashed line conditions and total C solubility (mol/kg fluid) at serpentinite dehydration, as in Figure 16 (computation details cf. Section 4.4)

models that use pure molecular $H_2O$–$CO_2$ fluids (Connolly & Galvez, 2018; Kelemen & Manning, 2015). The effect of variable bulk composition, pressure and temperature in the speciation of carbon-bearing solutes in equilibrium with meta-ophicarbonate rocks are shown in Figures 16 and 17 (cf. Section 4.4 for details on the computation). At the $P$–$T$ conditions of antigorite breakdown, molecular $CO_2$ is the dominant C-bearing species in fluid in equilibrium with serpentinite-hosted carbonate–silicate rocks with variable bulk composition (Figure 16). While the calculations likely slightly underestimate carbon solubility due to neglecting solute species involving Na, K and Cl (cf. Section 4.4), charged carbon-bearing species, such as $CaHCO_3^+$, $CaCO_{3,aq}$ and $HCO_3^-$, are generally minor and result in a small increase in the solubility of total carbon in the fluid (e.g. by ~0.2 mol C per kg fluid at 660°C, 1.7 GPa; Figure 16). Congruent dissolution of $CaCO_3$ to $CaHCO_3^+_{aq}$ and $HCO_3^-_{aq}$ is more important at <550–575°C and higher pressure (Figures 16 and 17). On the other hand, the contribution of charged carbon-bearing species to total carbon solubility becomes insignificant at $T$ > 650°C and $P$ < 1 GPa (Figure 17). These results suggest that—at the conditions of interest and considering the general uncertainties in thermodynamic data—molecular models underestimate only slightly the fluid carbon solubility relative to models accounting for electrolyte fluids and, therefore, are appropriate to model phase relations and devolatilization reactions in carbonate–silicate rocks such as those at Milagrosa and Almirez

(Table 3; Figures 13 and 15; see also Trommsdorff & Evans, 1977; Will, Powell, & Holland, 1990).

The dissolution of carbonate by external fluids depends on the local fluid/rock ratio and the relative permeability of meta-ophicarbonates and their host serpentinites. If local equilibrium between rock, solvent and solute is attained, the predominance of molecular $CO_2$ in the fluids (Figures 16 and 17) implies that infiltration-driven devolatilization of meta-ophicarbonates would be mainly controlled by reactions involving carbonates and silicates (Section 6.2.2; e.g. Reactions 5 and 6 in Table 3). This condition may be attained at low fluid-rock ratios and fast reaction kinetics, resulting in olivine and Ca-carbonate-rich assemblages when infiltrated by $H_2O$-fluids (see Section 6.2.2). High fluid/rock ratios and slower kinetics of silicate mineral dissolution may lead to a preferential congruent dissolution of carbonate relative to that of silicates. This process may produce diopside–olivine–chlorite rocks after carbonate–silicate rock and precipitation of secondary carbonate upstream along the fluid path.

The Almirez meta-ophicarbonates show no evidence of such disequilibrium processes indicating that fluid infiltration was limited, as also shown by the phase relations (Section 6.2.2). Relative to the dehydration of antigorite in the host serpentinite, the lower temperature of the main devolatilization reactions in carbonate–silicate rocks may favour their preservation beyond the conditions of antigorite breakdown. The presence of Ca-carbonate in the protolith changes the nature of the overall antigorite dehydration from a single discontinuous reaction for carbonate-free serpentinite at 660°C to a stepwise reaction series at lower temperatures in meta-ophicarbonates (Figure 15a–d). If fluids produced by devolatilization Reactions 1–4 (Table 3) are efficiently drained, stepwise dehydration increases the density of the solid rock (grey filled curves in Figure 15b–d). Meta-ophicarbonate lenses may then attain very low permeability domains relative to the host dehydrating serpentinite, favouring anisotropic fluid channelling around such lenses. Furthermore, at the conditions of antigorite breakdown in host serpentinite at 1.7 GPa, differences in bulk rock composition imply a 1 molal higher carbon solubility of fluids in equilibrium with Chl–Ol–Cpx–Tr–Mgs rocks (field 5 in Figure 15a; $X_{Serp} = 0.9$ in Figure 16) than with Chl–Ol–Cpx–Dol–Cal rocks ($X_{Serp} = 0.6$ in Figure 16). Hence, carbonate-rich assemblages such as those in the Almirez meta-ophicarbonate lenses are more likely to be preserved during antigorite breakdown than domains that contained low carbonate amounts in the protolith.

# 7 | CONCLUSIONS

Subduction-related, serpentinite-hosted, carbonate–silicate rocks from the NFC record a prograde metamorphic evolution to conditions prior and beyond the breakdown of antigorite in a warm subduction setting. Thermodynamic modelling and phase relations indicate peak metamorphic conditions for the carbonate–silicate rocks consistent with those recorded in the host serpentinite (Milagrosa massif; 550–600°C and 1.0–1.4 GPa) and Chl-harzburgite (Almirez massif; 1.7–1.9 GPa and 680°C), at low fluid $X_{CO_2}$.

Microstructures, mineral chemistry and phase relations show that the hybridized carbonate–silicate rocks formed before peak metamorphism, likely by seawater-related hydrothermal alteration, and were modified by subduction metamorphism and deformation. In the $CaO$–$MgO$–$SiO_2$ ternary, these processes resulted in a compositional variability of the NFC serpentinite-hosted carbonate–silicate rocks along the serpentinite-calcite mixing trend, similar to that of other serpentinite-hosted carbonate-rocks in palaeo-subducted metamorphic terranes. Thermodynamic modelling shows that during prograde subduction metamorphism the compositional variability along this binary determines the temperature of the main devolatilization reactions, the fluid composition and the mineral assemblages of reaction products. In comparison to classical $X_{CO_2}$ molecular fluid models, thermodynamic models considering electrolytic fluids slightly increase the total carbon solubility in fluids at the conditions of interest of this study, without significant changes in the topology of phase relations.

Phase relations in the Milagrosa and Almirez (meta) serpentinite-hosted carbonate–silicate rocks are consistent with fluid and rock equilibrium during peak metamorphism. The predominance of molecular $CO_2$ in contrast to charged carbon-bearing aqueous species at the conditions of HP antigorite breakdown indicates that carbon release from serpentinite-hosted carbonate–silicate rocks during subduction is intimately linked to devolatilization reactions involving carbonate and silicate minerals and, therefore, mostly depends on the bulk rock composition.

These results from our study show that carbonates can remain stable in (meta)serpentinite-hosted carbonate–silicate rocks despite the relatively high carbon solubility in a warm subduction setting and the high fluid fluxes produced by dehydration reactions in the host serpentinite. In subduction settings where carbonated peridotite in the slab is common (e.g. in slow spreading ocean crust), substantial amounts of carbonate may, therefore, be preserved beyond the conditions of antigorite breakdown at sub-arc depths, thus allowing recycling of carbon deeper into the mantle.

## CONFLICT OF INTEREST

The authors have no conflict of interest to declare.

## ORCID

*Manuel D. Menzel* 🆔 https://orcid.org/0000-0002-4681-9447

## REFERENCES

Ague, J. J., & Nicolescu, S. (2014). Carbon dioxide released from subduction zones by fluid-mediated reactions. *Nature Geoscience*, *7*(5), 355–360. https://doi.org/10.1038/ngeo2143

Alt, J. C., Crispini, L., Gaggero, L., Levine, D., Lavagnino, G., Shanks, P., & Gulbransen, C. (2018). Normal faulting and evolution of fluid discharge in a Jurassic seafloor ultramafic-hosted hydrothermal system. *Geology*, *46*(6), 523–526. https://doi.org/10.1130/g40287.1

Alt, J. C., Garrido, C. J., Shanks, W. C., Turchyn, A., Padrón-Navarta, J. A., López Sánchez-Vizcaíno, V., … Marchesi, C. (2012). Recycling of water, carbon, and sulfur during subduction of serpentinites: A stable isotope study of Cerro del Almirez, Spain. *Earth and Planetary Science Letters*, *327–328*, 50–60. https://doi.org/10.1016/j.epsl.2012.01.029

Angiboust, S., Pettke, T., De Hoog, J. C. M., Caron, B., & Oncken, O. (2014). Channelized fluid flow and eclogite-facies metasomatism along the subduction shear zone. *Journal of Petrology*, *55*(5), 883–916. https://doi.org/10.1093/petrology/egu010

Anovitz, L. M., & Essene, E. J. (1987). Phase equilibria in the system CaCO₃-MgCO₃-FeCO₃. *Journal of Petrology*, *28*(2), 389–415. https://doi.org/10.1093/petrology/28.2.389

Bach, W., Rosner, M., Jöns, N., Rausch, S., Robinson, L. F., Paulick, H., & Erzinger, J. (2011). Carbonate veins trace seawater circulation during exhumation and uplift of mantle rock: Results from ODP Leg 209. *Earth and Planetary Science Letters*, *311*(3–4), 242–252. https://doi.org/10.1016/j.epsl.2011.09.021

Bachmann, F., Hielscher, R., & Schaeben, H. (2010). Texture analysis with MTEX-free and open source software toolbox. Vol. 160. *Solid State Phenomena*, *160*, 63–68 https://doi.org/10.4028/www.scientific.net/SSP.160.63

Bebout, G. E., & Penniston-Dorland, S. C. (2016). Fluid and mass transfer at subduction interfaces – The field metamorphic record. *Lithos*, *240–243*, 228–258. https://doi.org/10.1016/j.lithos.2015.10.007

Behr, W. M., & Platt, J. P. (2012). Kinematic and thermal evolution during two-stage exhumation of a Mediterranean subduction complex. *Tectonics*, *31*(4). https://doi.org/10.1029/2012tc003121

Bonatti, E., Lawrence, J. R., Hamlyn, P. R., & Breger, D. (1980). Aragonite from deep sea ultramafic rocks. *Geochimica et Cosmochimica Acta*, *44*(8), 1207–1214. https://doi.org/10.1016/0016-7037(80)90074-5

Booth-Rea, G., Martínez-Martínez, J. M., & Giaconia, F. (2015). Continental subduction, intracrustal shortening, and coeval upper-crustal extension: P-T evolution of subducted south Iberian paleomargin metapelites (Betics, SE Spain). *Tectonophysics*, *663*, 122–139. https://doi.org/10.1016/j.tecto.2015.08.036

Bretscher, A., Hermann, J., & Pettke, T. (2018). The influence of oceanic oxidation on serpentinite dehydration during subduction. *Earth and Planetary Science Letters*, *499*, 173–184. https://doi.org/10.1016/j.epsl.2018.07.017

Bromiley, G. D., & Pawley, A. R. (2003). The stability of antigorite in the systems MgO-SiO₂-H₂O (MSH) and MgO-Al₂O₃-SiO₂-H₂O (MASH): The effects of Al³⁺ substitution on high-pressure stability. *American Mineralogist*, *88*(1), 99–108. https://doi.org/10.2138/am-2003-0113

Bucher, K., & Grapes, R. (2011). *Petrogenesis of metamorphic rocks* (8th ed.). Springer, Heidelberg Dordrecht London New York: Springer. https://doi.org/10.1007/978-3-540-74169-5

Caciagli, N. C., & Manning, C. E. (2003). The solubility of calcite in water at 6–16 kbar and 500–800°C. *Contributions to Mineralogy and Petrology*, *146*(3), 275–285. https://doi.org/10.1007/s00410-003-0501-y

Clerc, C., Boulvais, P., Lagabrielle, Y., & de Saint Blanquat, M. (2014). Ophicalcites from the northern Pyrenean belt: A field, petrographic and stable isotope study. *International Journal of Earth Sciences*, *103*(1), 141–163. https://doi.org/10.1007/s00531-013-0927-z

Collins, N. C., Bebout, G. E., Angiboust, S., Agard, P., Scambelluri, M., Crispini, L., & John, T. (2015). Subduction zone metamorphic pathway for deep carbon cycling: II. Evidence from HP/UHP metabasaltic rocks and ophicarbonates. *Chemical Geology*, *412*, 132–150. https://doi.org/10.1016/j.chemgeo.2015.06.012

Connolly, J. A. D. (2005). Computation of phase equilibria by linear programming: A tool for geodynamic modeling and its application to subduction zone decarbonation. *Earth and Planetary Science Letters*, *236*(1–2), 524–541. https://doi.org/10.1016/j.epsl.2005.04.033

Connolly, J. A. D. (2009). The geodynamic equation of state: What and how. *Geochemistry, Geophysics, Geosystems*, *10*(10). https://doi.org/0.1029/2009gc002540

Connolly, J. A. D., & Galvez, M. E. (2018). Electrolytic fluid speciation by Gibbs energy minimization and implications for subduction zone mass transfer. *Earth and Planetary Science Letters*, *501*, 90–102. https://doi.org/10.1016/j.epsl.2018.08.024

Connolly, J. A. D., & Trommsdorff, V. (1991). Petrogenetic grids for metacarbonate rocks – Pressure-temperature phase-diagram projection for mixed-volatile systems. *Contributions to Mineralogy*

*and Petrology*, *108*(1–2), 93–105. https://doi.org/10.1007/bf00307329

Cook-Kollars, J., Bebout, G. E., Collins, N. C., Angiboust, S., & Agard, P. (2014). Subduction zone metamorphic pathway for deep carbon cycling: I. Evidence from HP/UHP metasedimentary rocks, Italian Alps. *Chemical Geology*, *386*, 31–48. https://doi.org/10.1016/j.chemgeo.2014.07.013

Dasgupta, R. (2013). Ingassing, Storage, and Outgassing of Terrestrial Carbon through Geologic Time. *Reviews in Mineralogy and Geochemistry*, *75*(1), 183–229. https://doi.org/doi:10.2138/rmg.2013.75.7

Dasgupta, R., Hirschmann, M. M., & Withers, A. C. (2004). Deep global cycling of carbon constrained by the solidus of anhydrous, carbonated eclogite under upper mantle conditions. *Earth and Planetary Science Letters*, *227*(1–2), 73–85. https://doi.org/10.1016/j.epsl.2004.08.004

Debret, B., Andreani, M., Munoz, M., Bolfan-Casanova, N., Carlut, J., Nicollet, C., … Trcera, N. (2014). Evolution of Fe redox state in serpentine during subduction. *Earth and Planetary Science Letters*, *400*, 206–218. https://doi.org/10.1016/j.epsl.2014.05.038

Debret, B., Bolfan-Casanova, N., Padrón-Navarta, J. A., Martin-Hernandez, F., Andreani, M., Garrido, C. J., … Trcera, N. (2015). Redox state of iron during high-pressure serpentinite dehydration. *Contributions to Mineralogy and Petrology*, *169*(4), 1–18. https://doi.org/10.1007/s00410-015-1130-y

Debret, B., & Sverjensky, D. A. (2017). Highly oxidising fluids generated during serpentinite breakdown in subduction zones. *Scientific Reports*, *7*(1), 10351. https://doi.org/10.1038/s41598-017-09626-y

Dilissen, N., Hidas, K., Garrido, C. J., Kahl, W.-A., López Sánchez-Vizcaíno, V., & Padrón-Navarta, J. A. (2018). Textural evolution during high-pressure dehydration of serpentinite to peridotite and its relation to stress orientations and kinematics of subducting slabs: Insights from the Almirez ultramafic massif. *Lithos*, *320–321*, 470–489. https://doi.org/10.1016/j.lithos.2018.09.033

Dreimanis, A. (1962). Quantitative gasometric determination of calcite and dolomite by using Chittick apparatus. *Journal of Sedimentary Research*, *32*(3), 520–529. https://doi.org/10.1306/74d70d08-2b21-11d7-8648000102c1865d

Eickmann, B., Bach, W., & Peckmann, J. (2009). Authigenesis of carbonate minerals in Modern and Devonian ocean-floor hard rocks. *The Journal of Geology*, *117*(3), 307–323. https://doi.org/10.1086/597362

Eickmann, B., Bach, W., Rosner, M., & Peckmann, J. (2009). Geochemical constraints on the modes of carbonate precipitation in peridotites from the Logatchev hydrothermal vent field and Gakkel ridge. *Chemical Geology*, *268*(1–2), 97–106. https://doi.org/10.1016/j.chemgeo.2009.08.002

Engi, M., & Lindsley, D. H. (1980). Stability of titanian clinohumite: Experiments and thermodynamic analysis. *Contributions to Mineralogy and Petrology*, *72*(4), 415–424. https://doi.org/10.1007/BF00371348

Evans, B. W. (2004). The serpentinite multisystem revisited: Chrysotile is metastable. *International Geology Review*, *46*(6), 479–506. https://doi.org/10.2747/0020-6814.46.6.479

Evans, K. A., Reddy, S. M., Tomkins, A. G., Crossley, R. J., & Frost, B. R. (2017). Effects of geodynamic setting on the redox state of fluids released by subducted mantle lithosphere. *Lithos*, *278–281*, 26–42. https://doi.org/10.1016/j.lithos.2016.12.023

Evans, B. W., & Trommsdorff, V. (1983). Fluorine hydroxyl titanian clinohumite in Alpine recrystallized garnet peridotite: Compositional controls and petrologic significance. *American Journal of Science*, *283 A*, 355–369.

Facq, S., Daniel, I., Montagnac, G., Cardon, H., & Sverjensky, D. A. (2014). In situ Raman study and thermodynamic model of aqueous carbonate speciation in equilibrium with aragonite under subduction zone conditions. *Geochimica et Cosmochimica Acta*, *132*, 375–390. https://doi.org/10.1016/j.gca.2014.01.030

Facq, S., Daniel, I., Montagnac, G., Cardon, H., & Sverjensky, D. A. (2016). Carbon speciation in saline solutions in equilibrium with aragonite at high pressure. *Chemical Geology*, *431*, 44–53. https://doi.org/10.1016/j.chemgeo.2016.03.021

Falk, E. S., & Kelemen, P. B. (2015). Geochemistry and petrology of listvenite in the Samail ophiolite, Sultanate of Oman: Complete carbonation of peridotite during ophiolite emplacement. *Geochimica et Cosmochimica Acta*, *160*, 70–90. https://doi.org/10.1016/j.gca.2015.03.014

Ferrando, S., Groppo, C., Frezzotti, M. L., Castelli, D., & Proyer, A. (2017). Dissolving dolomite in a stable UHP mineral assemblage: Evidence from Cal-Dol marbles of the Dora-Maira Massif (Italian Western Alps). *American Mineralogist*, *102*(1), 42–60. https://doi.org/10.2138/am-2017-5761

Ferry, J. M. (2001). Calcite inclusions in forsterite. *American Mineralogist*, *86*(7–8), 773–779. https://doi.org/10.2138/am-2001-0701

Franz, G., & Ackermand, D. (1980). Phase relations and metamorphic history of a clinohumite-chlorite-serpentine-marble from the Western Tauern Area (Austria). *Contributions to Mineralogy and Petrology*, *75*(2), 97–110. https://doi.org/10.1007/BF00389771

Galvez, M. E., Connolly, J. A. D., & Manning, C. E. (2016). Implications for metal and volatile cycles from the pH of subduction zone fluids. *Nature*, *539*(7629), 420–424. https://doi.org/10.1038/nature20103

Galvez, M. E., Manning, C. E., Connolly, J. A. D., & Rumble, D. (2015). The solubility of rocks in metamorphic fluids: A model for rock-dominated conditions to upper mantle pressure and temperature. *Earth and Planetary Science Letters*, *430*, 486–498. https://doi.org/10.1016/j.epsl.2015.06.019

Garrido, C. J., López Sanchez-Vizcaíno, V., Gómez-Pugnaire, M. T., Trommsdorff, V., Alard, O., Bodinier, J., … Godard, M. (2005). Enrichment of HFSE in chlorite-harzburgite produced by high-pressure dehydration of antigorite-serpentinite: Implications for subduction magmatism. *Geochemistry, Geophysics, Geosystems*, *6*(1),. https://doi.org/doi:10.1029/2004gc000791

Gieré, R. (1987). Titanian clinohumite and geikielite in marbles from the Bergell contact aureole. *Contributions to Mineralogy and Petrology*, *96*(4), 496–502. https://doi.org/10.1007/bf01166694

Gómez-Pugnaire, M. T., Franz, G., & López Sánchez-Vizcaíno, V. (1994). Retrograde formation of NaCl-scapolite in high pressure metaevaporites from the Cordilleras Béticas (Spain). *Contributions to Mineralogy and Petrology*, *116*(4), 448–461. https://doi.org/10.1007/BF00310911

Gómez-Pugnaire, M. T., Nieto, F., Abad, I., Velilla, N., Garrido, C. J., Acosta-Vigil, A., … López Sánchez-Vizcaíno, V. (in press). Alpine Metamorphism in the Betic Internal Zones. In C. Quesada & J.T. Oliveira (Eds.), *The geology of Iberia: A geodynamic approach. The Alpine Cycle* (*3*), (pp. 1–26). New York, NY: Springer.

Gómez-Pugnaire, M. T., Rubatto, D., Fernández-Soler, J. M., Jabaloy, A., López Sánchez-Vizcaíno, V., González-Lodeiro, F., & Padrón-Navarta, J. A. (2012). Late Variscan magmatism in the

Nevado-Filábride Complex: U-Pb geochronologic evidence for the pre-Mesozoic nature of the deepest Betic complex (SE Spain). *Lithos*, *146–147*, 93–111. https://doi.org/10.1016/j.lithos.2012.03.027

Gorman, P. J., Kerrick, D. M., & Connolly, J. A. D. (2006). Modeling open system metamorphic decarbonation of subducting slabs. *Geochemistry, Geophysics, Geosystems*, *7*(4). https://doi.org/10.1029/2005gc001125

Grozeva, N. G., Klein, F., Seewald, J. S., & Sylva, S. P. (2017). Experimental study of carbonate formation in oceanic peridotite. *Geochimica et Cosmochimica Acta*, *199*, 264–286. https://doi.org/10.1016/j.gca.2016.10.052

Grützner, T., Klemme, S., Rohrbach, A., Gervasoni, F., & Berndt, J. (2017). The role of F-clinohumite in volatile recycling processes in subduction zones. *Geology*, *45*(5), 443–446. https://doi.org/10.1130/G38788.1

Helgeson, H. C., Kirkham, D. H., & Flowers, G. C. (1981). Theoretical prediction of the thermodynamic behavior of aqueous electrolytes by high pressures and temperatures; IV, Calculation of activity coefficients, osmotic coefficients, and apparent molal and standard and relative partial molal properties to 600 degrees C and 5kb. *American Journal of Science*, *281*(10), 1249–1516. https://doi.org/10.2475/ajs.281.10.1249

Hermann, J., Troitzsch, U., & Scott, D. (2016). Experimental sub-solidus phase relations in the system $CaCO_3$–$CaMg(CO_3)_2$ up to 6.5 GPa and implications for subducted marbles. *Contributions to Mineralogy and Petrology*, *171*(10), 84. https://doi.org/10.1007/s00410-016-1296-y https://doi.org/10.1007/s00410-016-1296-y

Hinsbergen, D. J. J., Vissers, R. L. M., & Spakman, W. (2014). Origin and consequences of western Mediterranean subduction, rollback, and slab segmentation. *Tectonics*, *33*(4), 393–419. https://doi.org/10.1002/2013TC003349

Holland, T., & Powell, R. (1991). A compensated-Redlich-Kwong (CORK) equation for volumes and fugacities of $CO_2$ and $H_2O$ in the range 1 bar to 50 kbar and 100-1600°C. *Contributions to Mineralogy and Petrology*, *109*(2), 265–273. https://doi.org/10.1007/BF00306484

Holland, T., & Powell, R. (1998). An internally consistent thermodynamic data set for phases of petrological interest. *Journal of Metamorphic Geology*, *16*(3), 309–343.

Jabaloy-Sánchez, A., Gómez-Pugnaire, M. T., Padrón-Navarta, J. A., López Sánchez-Vizcaíno, V., & Garrido, C. J. (2015). Subduction- and exhumation-related structures preserved in metaserpentinites and associated metasediments from the Nevado-Filábride Complex (Betic Cordillera, SE Spain). *Tectonophysics*, *644–645*, 40–57. https://doi.org/10.1016/j.tecto.2014.12.022

Kampschuur, W., & García Monzón, G. (Cartographer). (1975). Vera

Kelemen, P. B., & Manning, C. E. (2015). Reevaluating carbon fluxes in subduction zones, what goes down, mostly comes up. *Proceedings of the National Academy of Sciences of the United States of America*, *112*(30), E3997–E4006. https://doi.org/10.1073/pnas.1507889112

Kerrick, D. M., & Connolly, J. A. D. (1998). Subduction of ophicarbonates and recycling of $CO_2$ and $H_2O$. *Geology*, *26*(4), 375–378. https://doi.org/10.1130/0091-7613(1998)

Kerrick, D. M., & Connolly, J. A. D. (2001). Metamorphic devolatilization of subducted marine sediments and the transport of volatiles into the Earth`s mantle. *Nature*, *411*, 293. https://doi.org/10.1038/35077056

Kirchner, K. L., Behr, W. M., Loewy, S., & Stockli, D. F. (2016). Early Miocene subduction in the western Mediterranean: Constraints

from Rb-Sr multimineral isochron geochronology. *Geochemistry, Geophysics, Geosystems*, *17*(5), 1842–1860. https://doi.org/10.1002/2015GC006208

Klein, F., Humphris, S. E., Guo, W., Schubotz, F., Schwarzenbach, E. M., & Orsi, W. D. (2015). Fluid mixing and the deep biosphere of a fossil Lost City-type hydrothermal system at the Iberia Margin. *Proceedings of the National Academy of Sciences of the United States of America*, *112*(39), 12036–12041. https://doi.org/10.1073/pnas.1504674112

Laborda-López, C., López Sánchez-Vizcaíno, V., Marchesi, C., Gómez-Pugnaire, M. T., Garrido, C. J., Jabaloy-Sánchez, A., … Hidas, K. (2018). High-P metamorphism of rodingites during serpentinite dehydration (Cerro del Almirez, Southern Spain): Implications for the redox state in subduction zones. *Journal of Metamorphic Geology*, *36*(9), 1141–1173. https://doi.org/10.1111/jmg.12440

Lafay, R., Baumgartner, P. L., Schwartz, S., Picazo, S., Montes-Hernandez, G., & Vennemann, T. (2017). Petrologic and stable isotopic studies of a fossil hydrothermal system in ultramafic environment (Chenaillet ophicalcites, Western Alps, France): Processes of carbonate cementation. *Lithos*, *294–295*, 319–338. https://doi.org/10.1016/j.lithos.2017.10.006

Lagabrielle, Y., Vitale Brovarone, A., & Ildefonse, B. (2015). Fossil oceanic core complexes recognized in the blueschist metaophiolites of Western Alps and Corsica. *Earth-Science Reviews*, *141*, 1–26. https://doi.org/10.1016/j.earscirev.2014.11.004

Li, J.-L., Klemd, R., Gao, J., & Meyer, M. (2014). Compositional zoning in dolomite from lawsonite-bearing eclogite (SW Tianshan, China): Evidence for prograde metamorphism during subduction of oceanic crust. *American Mineralogist*, *99*(1), 206–217. https://doi.org/10.2138/am.2014.4507

Li, B., & Massonne, H. J. (2018). Two Tertiary metamorphic events recognized in high-pressure metapelites of the Nevado-Filábride Complex (Betic Cordillera, S Spain). *Journal of Metamorphic Geology*, *36*(5), 603–630. https://doi.org/10.1111/jmg.12312

López Sánchez-Vizcaíno, V., Connolly, J. A. D., & Gomez-Pugnaire, M. T. (1997). Metamorphism and phase relations in carbonate rocks from the Nevado-Filibride Complex (Cordilleras Beticas, Spain): Application of the Ttn+Rt+Cal+Qtz+Gr buffer. *Contributions to Mineralogy and Petrology*, *126*(3), 292–302. https://doi.org/10.1007/s004100050251

López Sánchez-Vizcaíno, V., Gómez-Pugnaire, M. T., Garrido, C. J., Padrón-Navarta, J. A., & Mellini, M. (2009). Breakdown mechanisms of titanclinohumite in antigorite serpentinite (Cerro del Almirez massif, S. Spain): A petrological and TEM study. *Lithos*, *107*(3–4), 216–226. https://doi.org/10.1016/j.lithos.2008.10.008

López Sánchez-Vizcaíno, V., Rubatto, D., Gómez-Pugnaire, M. T., Trommsdorff, V., & Müntener, O. (2001). Middle Miocene high-pressure metamorphism and fast exhumation of the Nevado-Filabride Complex, SE Spain. *Terra Nova*, *13*(5), 327–332. https://doi.org/10.1046/j.1365-3121.2001.00354.x

López Sánchez-Vizcaíno, V., Trommsdorff, V., Gómez-Pugnaire, M. T., Garrido, C. J., Müntener, O., & Connolly, J. A. D. (2005). Petrology of titanian clinohumite and olivine at the high-pressure breakdown of antigorite serpentinite to chlorite harzburgite (Almirez Massif, S. Spain). *Contributions to Mineralogy and Petrology*, *149*(6), 627–646. https://doi.org/10.1007/s00410-005-0678-3

Ludwig, K. A., Kelley, D. S., Butterfield, D. A., Nelson, B. K., & Früh-Green, G. (2006). Formation and evolution of carbonate chimneys

at the Lost City hydrothermal field. *Geochimica et Cosmochimica Acta*, *70*(14), 3625–3645. https://doi.org/10.1016/j.gca.2006.04.016

Malvoisin, B., Chopin, C., Baronnet, A., Brunet, F., Bezacier, L., & Guillot, S. (2017). Fe–Ni-rich silicate aggregates formed after sulfides in high-pressure serpentinites. *Journal of Petrology*, *58*(5), 963–978. https://doi.org/10.1093/petrology/egx042

Marchesi, C., Garrido, C. J., Padrón-Navarta, J. A., López Sánchez-Vizcaíno, V., & Gomez-Pugnaire, M. T. (2013). Element mobility from seafloor serpentinization to high-pressure dehydration of antigorite in subducted serpentinite: Insights from the Cerro del Almirez ultramafic massif (southern Spain). *Lithos*, *178*, 128–142. https://doi.org/10.1016/j.lithos.2012.11.025

Martínez-Martínez, J. M., Torres-Ruiz, J., Pesquera, A., & Gil-Crespo, P. P. (2010). Geological relationships and U-Pb zircon and 40Ar/39Ar tourmaline geochronology of gneisses and tourmalinites from the Nevado-Filabride complex (western Sierra Nevada, Spain): Tectonic implications. *Lithos*, *119*(3–4), 238–250. https://doi.org/10.1016/j.lithos.2010.07.002

Mazzoli, S., Martín-Algarra, A., Reddy, S. M., López Sánchez-Vizcaíno, V., Fedele, L., & Noviello, A. (2013). The evolution of the footwall to the Ronda subcontinental mantle peridotites: insights from the Nieves Unit (western Betic Cordillera). *Journal of the Geological Society*, *170*(3), 385–402. https://doi.org/10.1144/jgs2012-105

Menzel, M. D., Garrido, C. J., López Sánchez-Vizcaíno, V., Marchesi, C., Hidas, K., Escayola, M. P., & Delgado Huertas, A. (2018). Carbonation of mantle peridotite by $CO_2$-rich fluids: The formation of listvenites in the Advocate ophiolite complex (Newfoundland, Canada). *Lithos*, *323*, 238–261. https://doi.org/10.1016/j.lithos.2018.06.001

Mizuochi, H., Satish-Kumar, M., Motoyoshi, Y., & Michibayashi, K. (2010). Exsolution of dolomite and application of calcite-dolomite solvus geothermometry in high-grade marbles: An example from Skallevikshalsen, East Antarctica. *Journal of Metamorphic Geology*, *28*(5), 509–526. https://doi.org/10.1111/j.1525-1314.2010.00877.x

Padrón-Navarta, J. A., Hermann, J., Garrido, C. J., López Sánchez-Vizcaíno, V., & Gómez-Pugnaire, M. T. (2010). An experimental investigation of antigorite dehydration in natural silica-enriched serpentinite. *Contributions to Mineralogy and Petrology*, *159*(1), 25–42. https://doi.org/10.1007/s00410-009-0414-5

Padrón-Navarta, J. A., López Sánchez-Vizcaíno, V., Garrido, C. J., & Gomez-Pugnaire, M. T. (2011). Metamorphic record of high-pressure dehydration of antigorite serpentinite to chlorite harzburgite in a subduction setting (Cerro del Almirez, Nevado-Filabride Complex, Southern Spain). *Journal of Petrology*, *52*(10), 2047–2078. https://doi.org/10.1093/petrology/egr039

Padrón-Navarta, J. A., López Sánchez-Vizcaíno, V., Hermann, J., Connolly, J. A. D., Garrido, C. J., Gómez-Pugnaire, M. T., & Marchesi, C. (2013). Tschermak's substitution in antigorite and consequences for phase relations and water liberation in high-grade serpentinites. *Lithos*, *178*, 186–196. https://doi.org/10.1016/j.lithos.2013.02.001

Padrón-Navarta, J. A., Tommasi, A., Garrido, C. J., & López Sánchez-Vizcaíno, V. (2012). Plastic deformation and development of antigorite crystal preferred orientation in high-pressure serpentinites. *Earth and Planetary Science Letters*, *349–350*, 75–86. https://doi.org/10.1016/j.epsl.2012.06.049

Padrón-Navarta, J. A., Tommasi, A., Garrido, C. J., López Sánchez-Vizcaíno, V., Gómez-Pugnaire, M. T., Jabaloy, A., & Vauchez, A. (2010). Fluid transfer into the wedge controlled by high-pressure

hydrofracturing in the cold top-slab mantle. *Earth and Planetary Science Letters*, *297*(1–2), 271–286. https://doi.org/10.1016/j.epsl.2010.06.029

Picazo, S., Manatschal, G., Cannat, M., & Andréani, M. (2013). Deformation associated to exhumation of serpentinized mantle rocks in a fossil ocean continent transition: The Totalp unit in SE Switzerland. *Lithos*, *175–176*, 255–271. https://doi.org/10.1016/j.lithos.2013.05.010

Piccoli, F., Vitale Brovarone, A., & Ague, J. J. (2018). Field and petrological study of metasomatism and high-pressure carbonation from lawsonite eclogite-facies terrains, Alpine Corsica. *Lithos*, *304–307*, 16–37. https://doi.org/10.1016/j.lithos.2018.01.026

Piccoli, F., Vitale Brovarone, A., Beyssac, O., Martinez, I., Ague, J. J., & Chaduteau, C. (2016). Carbonation by fluid-rock interactions at high-pressure conditions: Implications for carbon cycling in subduction zones. *Earth and Planetary Science Letters*, *445*, 146–159. https://doi.org/10.1016/j.epsl.2016.03.045

Platt, J. P., Anczkiewicz, R., Soto, J.-I., Kelley, S. P., & Thirlwall, M. (2006). Early Miocene continental subduction and rapid exhumation in the western Mediterranean. *Geology*, *34*(11), 981–984. https://doi.org/10.1130/g22801a.1

Platt, J. P., Behr, W. M., Johanesen, K., & Williams, J. R. (2013). The Betic-Rif arc and its Orogenic hinterland: A review. *Annual Review of Earth and Planetary Sciences*, *41*(1), 313–357. https://doi.org/10.1146/annurev-earth-050212-123951

Poli, S. (2015). Carbon mobilized at shallow depths in subduction zones by carbonatitic liquids. *Nature Geoscience*, *8*(8), 633–636. https://doi.org/10.1038/ngeo2464

Pozzorini, D., & Früh-Green, G. L. (1996). Stable isotope systematics of the Ventina Ophicarbonate Zone, Bergell contact aureole. *Schweizerische Mineralogische Und Petrographische Mitteilungen*, *76*(3), 549–564.

Proyer, A., Mposkos, E., Baziotis, I., & Hoinkes, G. (2008). Tracing high-pressure metamorphism in marbles: Phase relations in high-grade aluminous calcite–dolomite marbles from the Greek Rhodope massif in the system $CaO–MgO–Al_2O_3–SiO_2–CO_2$ and indications of prior aragonite. *Lithos*, *104*(1–4), 119–130. https://doi.org/10.1016/j.lithos.2007.12.002

Puga, E., Fanning, M., Díaz de Federico, A., Nieto, J. M., Beccaluva, L., Bianchini, G., & Díaz Puga, M. A. (2011). Petrology, geochemistry and U-Pb geochronology of the Betic Ophiolites: Inferences for Pangaea break-up and birth of the westernmost Tethys Ocean. *Lithos*, *124*(3), 255–272. https://doi.org/10.1016/j.lithos.2011.01.002

Ranero, C. R., Phipps Morgan, J., McIntosh, K., & Reichert, C. (2003). Bending-related faulting and mantle serpentinization at the Middle America trench. *Nature*, *425*(6956), 367–373. https://doi.org/10.1038/nature01961

Rice, J. M. (1980). Phase equilibria involving humite minerals in impure dolomitic limestones. *Contributions to Mineralogy and Petrology*, *71*(3), 219–235. https://doi.org/10.1007/BF00371664

Rüpke, L. H., Morgan, J. P., Hort, M., & Connolly, J. A. D. (2004). Serpentine and the subduction zone water cycle. *Earth and Planetary Science Letters*, *223*(1–2), 17–34. https://doi.org/10.1016/j.epsl.2004.04.018

Scambelluri, M., Bebout, G. E., Belmonte, D., Gilio, M., Campomenosi, N., Collins, N., & Crispini, L. (2016). Carbonation of subduction-zone serpentinite (high-pressure ophicarbonate; Ligurian Western Alps) and implications for the deep carbon cycling. *Earth and*

*Planetary Science Letters*, *441*, 155–166. https://doi.org/10.1016/j.epsl.2016.02.034

Scambelluri, M., Müntener, O., Ottolini, L., Pettke, T. T., & Vannucci, R. (2004). The fate of B, Cl and Li in the subducted oceanic mantle and in the antigorite breakdown fluids. *Earth and Planetary Science Letters*, *222*(1), 217–234. https://doi.org/10.1016/j.epsl.2004.02.012

Schroeder, T., Bach, W., Jöns, N., Jöns, S., Monien, P., & Klügel, A. (2015). Fluid circulation and carbonate vein precipitation in the footwall of an oceanic core complex, Ocean Drilling Program Site 175, Mid-Atlantic Ridge. *Geochemistry, Geophysics, Geosystems*, *16*(10), 3716–3732. https://doi.org/10.1002/2015GC006041

Schwarzenbach, E. M., Früh-Green, G. L., Bernasconi, S. M., Alt, J. C., & Plas, A. (2013). Serpentinization and carbon sequestration: A study of two ancient peridotite-hosted hydrothermal systems. *Chemical Geology*, *351*, 115–133. https://doi.org/10.1016/j.chemgeo.2013.05.016

Sieber, M. J., Hermann, J., & Yaxley, G. M. (2018). An experimental investigation of C–O–H fluid-driven carbonation of serpentinites under forearc conditions. *Earth and Planetary Science Letters*, *496*, 178–188. https://doi.org/10.1016/j.epsl.2018.05.027

Siivola, J., & Schmid, R. (2007). A systematic nomenclature for metamorphic rocks 12. List of mineral abbreviations. Recommendations by the IUGS Subcommission on the Systematics of Metamorphic Rocks.

Stucki, A. (2001). High grade Mesozoic ophiolites of the Southern Steep Belt, Central Alps (PhD thesis), Swiss Federal Institute of Technology Zürich (ETH).

Sverjensky, D. A., Harrison, B., & Azzolini, D. (2014). Water in the deep Earth: The dielectric constant and the solubilities of quartz and corundum to 60 kb and 1200°C. *Geochimica et Cosmochimica Acta*, *129*, 125–145. https://doi.org/10.1016/j.gca.2013.12.019

Tiraboschi, C., Tumiati, S., Sverjensky, D., Pettke, T., Ulmer, P., & Poli, S. (2017). Experimental determination of magnesia and silica solubilities in graphite-saturated and redox-buffered high-pressure COH fluids in equilibrium with forsterite + enstatite and magnesite + enstatite. *Contributions to Mineralogy and Petrology*, *173*(1), 2. https://doi.org/10.1007/s00410-017-1427-0

Trommsdorff, V., & Connolly, J. A. D. (1996). The ultramafic contact aureole about the Bregaglia (Bergell) tonalite: Isograds and a thermal model. *Schweizerische Mineralogische Und Petrographische Mitteilungen*, *76*(3), 537–547.

Trommsdorff, V., & Evans, B. W. (1977). Antigorite-ophicarbonates: Phase relations in a portion of the system CaO-MgO-SiO$_2$-H$_2$O-CO$_2$. *Contributions to Mineralogy and Petrology*, *60*(1), 39–56. https://doi.org/10.1007/BF00372850

Trommsdorff, V., López Sánchez-Vizcaíno, V., Gomez-Pugnaire, M. T., & Müntener, O. (1998). High pressure breakdown of antigorite to spinifex-textured olivine and orthopyroxene, SE Spain. *Contributions to Mineralogy and Petrology*, *132*(2), 139–148. https://doi.org/10.1007/s004100050412

Tumiati, S., Fumagalli, P., Tiraboschi, C., & Poli, S. (2013). An experimental study on COH-bearing peridotite up to 3·2 GPa and implications for crust-mantle recycling. *Journal of Petrology*, *54*(3), 453–479. https://doi.org/10.1093/petrology/egs074

Ulmer, P., & Trommsdorff, V. (1995). Serpentine stability to mantle depths and subduction-related magmatism. *Science*, *268*(5212), 858. https://doi.org/10.1126/science.268.5212.858

van Keken, P. E., Hacker, B. R., Syracuse, E. M., & Abers, G. A. (2011). Depthdependent flux of H O from subducting slabs worldwide. *Journal of Geophysical Research*, *116*(B1). https://doi.org/:10.1029/2010jb007922

Vitale Brovarone, A., Chu, X., Martin, L., Ague, J. J., Monié, P., Groppo, C., … Chaduteau, C. (2018). Intra-slab COH fluid fluxes evidenced by fluid-mediated decarbonation of lawsonite eclogite-facies altered oceanic metabasalts. *Lithos*, *304–307*, 211–229. https://doi.org/10.1016/j.lithos.2018.01.028

Vitale Brovarone, A., Martinez, I., Elmaleh, A., Compagnoni, R., Chaduteau, C., Ferraris, C., & Esteve, I. (2017). Massive production of abiotic methane during subduction evidenced in metamorphosed ophicarbonates from the Italian Alps. *Nature Communications*, *8*, 14134. https://doi.org/10.1038/ncomms14134

Weiss, M. (1997). Clinohumites: A field and experimental study. PhD thesis, Swiss Federal Institute of Technology Zürich (ETH).

Will, T. M., Powell, R., & Holland, T. (1990). A calculated petrogenetic grid for ultramafic rocks in the system CaO-FeO-MgO-Al$_2$O$_3$-SiO$_2$-CO$_2$-H$_2$O at low pressures. *Contributions to Mineralogy and Petrology*, *105*(3), 347–358. https://doi.org/10.1007/BF00306544

**SUPPORTING INFORMATION**

Additional supporting information may be found online in the Supporting Information section at the end of the article.

**Figure S1.** BSE and reflected light images of oxides in Milagrosa and Almirez rocks. (a) Association of Ca-Ti-perovskite (Prv) rimmed by ilmenite (Ilm) with inclusions of uraninite (UO$_2$) and zirconolite (Zrc), pyrite (Py) and pyrrhotite (Po) in Milagrosa TiCl-Cal marble (SN-100; BSE image). (b) Cr-bearing magnetite in Milagrosa Atg–Di–Dol rock (SN-98), with the core rich in chlorite inclusions (likely tracing magnetite after Cr-spinel) and inclusion-free rims (Mag-2). Rims are locally replaced by hematite (reflected light image). (c) BSE image of magnetite in Almirez meta-ophicarbonate (SN-138), showing cores with abundant chlorite inclusions and inclusion-free rims and neoblasts. (d) Reflected light image of the same sample as in c), showing similar magnetite textures and relatively abundant pentlandite (Pn).

**Figure S2.** Histograms of frequency of measured $X_{MgCO_3}$ in calcite and dolomite analysed by electron microprobe from Milagrosa marble lenses (grey histogram) and Almirez meta-ophicarbonate (yellow histogram) and calcite-dolomite miscibility gap after Anovitz and Essene (1987).

**Figure S3.** $T$-$X_{CO_2}$ pseudosections of meta-ophicarbonate compositions with XSerp = 0.8 (a, b) and 0.9 (c, d) at 1.8 and 1.0 GPa respectively, superposed on the CO2 content in the solid (common colourbar in a; the colour scale is the same as in Figure 13b,c). Yellow dashed arrows show rock-buffered fluid evolution paths for serpentine-calcite protoliths, with

the yellow star indicating fluid $X_{CO_2}$ at conditions of antigorite breakdown in the host serpentinite.

**Table S1.** Representative electron microprobe analyses of carbonates.

**Table S2.** Representative electron microprobe analyses of olivine, Ti-clinohumite and TiChn.

**Table S3.** Representative electron microprobe analyses of clinopyroxene, diopside, amphiboles and talc.

**Table S4.** Representative electron microprobe analyses of serpentine and chlorite.

**Table S5.** Representative electron microprobe analyses of oxide minerals.

**Appendix S1** Phases and solution models used for thermodynamic modelling.